Design Method and Dynamic Response of Floating Ocean Thermal Energy Conversion (OTEC) Plant

久松, 稜弥

Design Method and Dynamic Response of Floating Ocean Thermal Energy Conversion (OTEC) Plant

HISAMATSU Ryoya

January 2023

Doctoral Dissertation

Design Method and Dynamic Response of Floating Ocean Thermal Energy Conversion (OTEC) Plant

Submitted to the Department of Maritime Engineering,
Graduate School of Engineering, Kyushu University,
as a partial fulfillment of the requirements for
Degree of Doctor of Engineering

By

HISAMATSU Ryoya

Supervised by

Prof. Dr. Eng. UTSUNOMIYA Tomoaki

Department of Maritime Engineering,
Graduate School of Engineering, Kyushu University

January 2023

ACKNOWLEDGEMENT

First and foremost, I would like to express the deepest appreciation to my supervisor Professor Tomoaki Utsunomiya. He introduced me this research topic and kindly guided me throughout my undergraduate, master and doctor courses. He also gave me many opportunities to grow as a person who tends to be withdrawn. Without his help, I would not have been able to finish my degree.

I am grateful to Dr. Ristiyanto Adiputra who was an assistant professor at Kyushu University. He pioneered this research field before I started my research and introduced me to it. He was also willing to discuss with me and provided me insightful suggestions and warm encouragement as I progressed this work.

This work was partially supported in part by the Collaborative Research Program of Research Institute for Applied Mechanics, Kyushu University. This work was supported by JST SPRING, Grant Number JPMJSP2136.

My gratitude is extended to the following scholarship programs: REDAS in the Shipbuilders' Association of Japan (SAJ), and the program of Support for Pioneering Research Initiated by the Next Generation (SPRING) by Japan Science and Technology Agency (JST). The scholarships enabled me to concentrate on this study.

I appreciate the technical service division of RIAM for their great support in setting up the experimental apparatus. Thank to the members of the OTEC group in Ocean Energy Resources Laboratory, Mr. Yusei Yamaguchi and Mr. Kouki Yamagishi, for their cooperation in the experiment.

I acknowledge the cooperation and encouragement of past and present members of Ocean Energy Resources Laboratory, Kyushu University. All the people I met in the laboratory made my student life pleasurable and productive. Especially, I would like to thank Assistant Professor Takaaki Takeuchi at Osaka University, for his valuable advice when he was a member of the laboratory.

Later, I would like to offer my special thanks to my family. Their warm support and understanding encouraged me to complete my degree.

ABSTRACT

An Ocean Thermal Energy Conversion (OTEC) is the system which utilizes a temperature difference between surface seawater and deep seawater to drive a heat engine. Since sea temperatures do not change significantly in the short term, this energy source is expected to be operate with a high stability and a high capacity factor among natural energy sources. Because of this main characteristic, an OTEC plant could have a large potential to contribute as a base-load power in tropical island countries, such as Indonesia. Furthermore, to utilize the advantage of scale, a 100 MW floating plant has frequently been studied for a commercial-scale deployment. However, the estimated levelized cost of energy of OTEC is still higher than existing base-load powers, and its evaluation also involves many uncertainties.

A commercial scale OTEC plant requires a large amount of seawater to drive the heat engine from only a 20 ℃ of temperature difference. For a 100 MW plantship, a Cold Water Pipe (CWP) with the diameter of 12 m and the length of 800 m will be required to intake deep seawater. Comparing to an offshore Oil & Gas riser, the mechanical characteristics of CWP are that (i) the diameter is significantly large, (ii) it contains a large mass flow rate, (iii) it is always hanged off even during operation, and thus (iv) the lower end is open in underwater. Currently, a design method has been developed for individual projects, and there seems to be no systematic analysis and design methodology that focuses on these mechanical characteristics.

The overall objective of this thesis is to clarify the design methodology of a floating OTEC plant and its mechanical characteristics through a preliminary design of a 100 MW plantship. This thesis is divided into 6 chapters as follows.

Chapter 1, general introduction, firstly introduces the general overview of OTEC. Subsequently, the development history and current status of a floating OTEC with regard to offshore engineering are reviewed to clarify the position and the overall objective of this study.

In chapter 2, the environmental conditions, hull geometry, mooring system and CWP are configured for analysis model. An analysis model of the plantship is designed from KVLCC2M and the CWP is assumed as made of FRP. The environmental conditions for Indonesia seas are assumed for the extreme analysis. A spread mooring system is considered preferable as a position keeping system. Preliminary designs by several combinations of a flexible joint, a clump weight for the CWP, taut mooring system and catenary mooring system are compared on their dynamic behavior by using OrcaFlex. Two kinds of models which are calculated by direct coupled system and only CWP under the forced oscillation obtained by the moored ship without CWP are

compared in order to examine those interactions. As a result, it is found that the interaction is significant and thus should not be ignored around the resonant frequency of the CWP and the slowly-varying drift motion of the plantship.

The aim of chapter 3 is to construct a simplified analysis model/method to easily comprehend the coupled responses characteristics of the floating platform, CWP and mooring system for the preliminary design stage. The equations of equilibrium and motion are derived based on simplifying a floating OTEC plant to a two-dimensional floating body and an elastic pendulum. This model is compared with time domain analysis from chapter 2, in order to verify the applicability for a practical design and limitation of this present model. It is observed that the present model has predicted the coupled response with practically sufficient accuracy for the early design stage. Subsequently, the influence of the design parameters for CWP to the coupled responses is also clarified by a parametric study combining the bending stiffness, the linear density, and the boundary conditions, as a preliminary design methodology using the present model.

As a critical phenomenon for the design, there are concerns about a self-induced vibration due to large momentum of internal flow. However, our knowledge of the dynamics of such pipes is based on limited experimental studies and the dynamics would seem to be not definitely established. This issue is considered to be an important outstanding question in the dynamics of the CWP and pursued it experimentally and theoretically in chapters 4 and 5.

Chapter 4 reports a tank experiment using a polycarbonate pipe with 4 m length. As first configuration, the free vibration with internal flow is measured by a set-up in which possible disturbances is removed. As a result, a flutter is not observed at a maximum flow velocity of 1.66 m/s. In addition, the observed free vibration seems to be essentially nonlinear and three-dimensional. As second configuration, the behavior at a range of high intaking flow velocity generated by a centrifugal vacuum pump is measured. As a result, a typical flutter is not observed at the maximum flow velocity of 4.1 m/s, while only long-period behavior of less than 5% of the diameter is observed at the tip of the pipe. The existing theory and simulation predicted that a self-induced vibration occur at this flow velocity. Therefore, the experiment reveals the necessary to improve the theory.

In chapter 5, a new model of the inlet flow field, which plays an important role on stability, considering the flow separation and jet formed inside of the pipe entrance is presented based on a CFD analysis. This equation is solved by FEM for time integration and eigenvalue analysis, and the results reproduce the experimental observations. The model also suggests that an aspirating pipe submerged in water does not flutter up to the practically reachable flow velocity.

Chapter 6, concluding remarks, states the general conclusions obtained above and future works.

CONTENTS

LIST OF FIGURES

LIST OF TABLES

1 GENERAL INTRODUCTION

1. 1 Introduction of OTEC

The total amount of energy flowing into the earth from solar radiation is estimated to be 1.75×10^{14} kW, about 50% of which reaches the surface of the ground and the ocean. Part of the energy irradiated on the sea surface is stored in the ocean as thermal energy. In the surface layer of the ocean at low latitudes, which receives a particularly large amount of solar irradiance, a seawater temperature reaches over 25°C. While the deep layer is hardly affected by solar radiation and the seawater temperature is maintained at a constant value of about 5°C. Low-latitude Ocean is constantly divided into a surface mixed layer, a thermocline in which temperature changes drastically with the depth, and a deep isothermal layer.

An Ocean Thermal Energy Conversion (OTEC) [1] is the system that utilizes a temperature difference between the surface layer and deep layer of the ocean to drive a heat engine. Since sea temperature does not change significantly in the short term, this energy source is expected to be operate with high stability and a high capacity factor among natural energy sources. Moreover, the global power potential of OTEC is estimated at 7×10^{9} kW (61,000 TWh/year) [2–4], despite a conservative scenario. Fig. 1-1 shows the sites which have high global ocean thermal resources based on the data from the World Ocean Atlas 2005. Generally, a commercial operation would be possible in the areas where above 20℃ of the temperature difference indicated with the colors in Fig. 1-1. In particular in remote islands such as Okinawa and Hawaii and low-latitude island

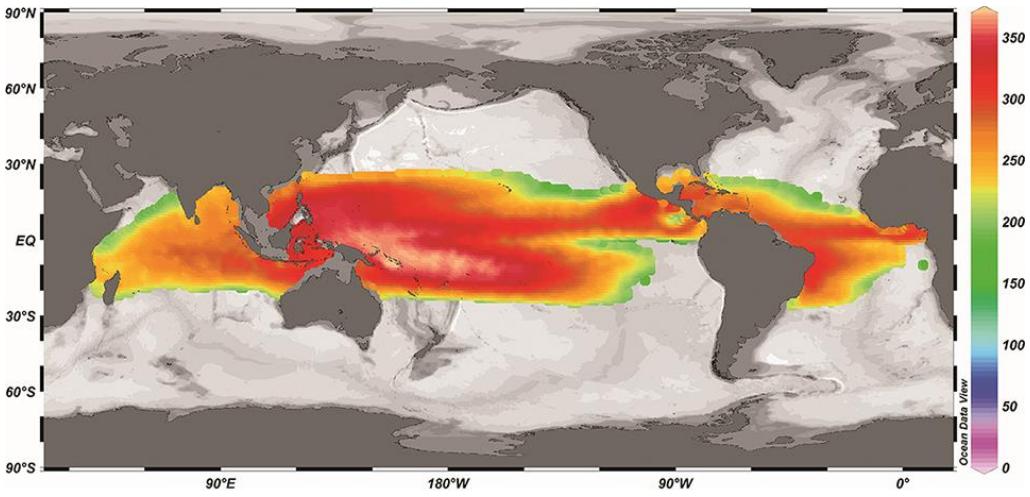

Fig. 1-1 Yearly averaged OTEC power density (kWm^{-2}) [3].

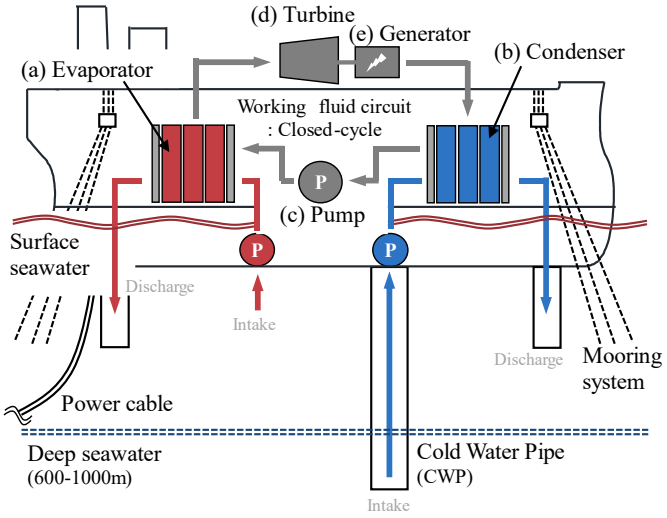

Fig. 1-2 Sketch of a floating OTEC plant.

countries such as Indonesia, an OTEC plant could have a large potential to contribute as a base-load power.

A heat cycle of OTEC can be broadly divided into Open Cycle and Closed Cycle, with the Closed Cycle currently adapted in many concepts. The configuration and mechanism are shown in Fig. 1-2. The plant is configured by working fluid, (a) evaporator, (b) condenser, (c) pumps, (d) turbine and (e) generator. Working fluid is a low boiling point medium, such as ammonia or its mixture with water. The procedure of the heat engine is:

(i) In the evaporator, working fluid in liquid phase is evaporated by exchanging heat with surface seawater.
(ii) Evaporated working fluid drives the turbine, then the kinematic energy is converted into electricity in the generator.
(iii) In the condenser, working fluid is restored to liquid phase by exchanging heat with deep seawater.
(iv) The working fluid pump loops back working fluid to the evaporator.

Because the available temperature difference is relatively small, the thermal efficiency is evaluated 3-4%, and besides the net power considering the pumping is about 2-3% of the thermal efficiency [1]. Therefore, a large amount of seawater-pumping and discharging facilities should be needed in order to obtain commercial feasibility by only the OTEC plant. In particular, a Cold Water Pipe (CWP) is required to be a large diameter and length to intake a large amount of deep seawater from a depth of 600-1,000 m. Hence the CWP has been considered the most challenging component in the deep seawater utilization industry.

An OTEC plant is considered as a land-based plant or an offshore floating plant. The land-

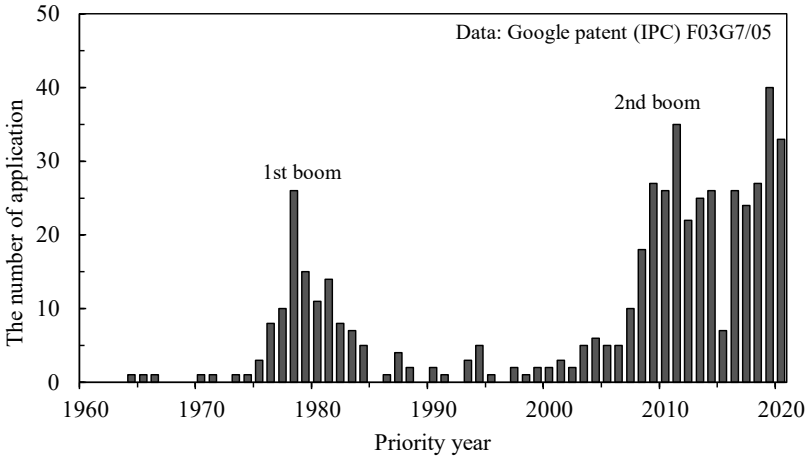

Fig. 1-3 The number of patent application regarding OTEC.

based plant has advantages on maintainability, easier transmission of resulting products to the respective grid, and integration with the utilization of deep seawater. Despite these advantages, the issues are that the laying distance of a CWP could be very long which increases the cost depending on the seafloor topography and the plant capacity. For a floating plant, the CWP is vertically hanged off from the platform, thus minimizing the seawater transport distance. Because of these characteristics, the land-based plant has been planned for a demonstration and a small-scale plant, while a floating plant has been planned for a large-scale commercial deployment.

Fig. 1-3 shows the number of patent applications regarding OTEC since 1960. The first peak in 1975-1985 is known as the first boom, triggered by the oil crisis in 1973. A number of studies on conceptual designs and component technologies made rapid progress, and a demonstration plant was succeeded in net power production. However, an OTEC plant has not yet been commercialized due to technical and economical reasons. The second boom from 2005 is led by a surge of interest in reducing carbon dioxide emissions, and there has been renewed development to solve the economical issue, to scale up to the plant larger than 10 MW, and to integrate other productions.

1. 2 **Historical Background**

The history of OTEC development dates back to the end of the 19th century. From there, OTEC has been developed intermittently, and several projects around the world have made significant progress. This section introduces these important projects and studies and identifies the current status of the technology and remaining issues with regard to a floating OTEC plant and marine engineering.

(1) Early works and demonstrations

D'Arsonval, a French scientist, first put forward a concept of a closed cycle OTEC system in 1881. Subsequently, his student Claude conducted a large-scale demonstration experiment in the first half of the 20th century. In 1930, Claude built a land-based plant using an open cycle in Cuba, and the plant demonstrated 22 kW of gross power production [5]. However, the plant failed to achieve net power production, and it highlighted the difficulty of laying the CWP of the diameter of 1.6 m and the length of 2 km.

In 1933-1935, Claude subsequently constructed the 800 kW floating plant which was converted from a 10,000-ton cargo ship [1]. The CWP with the diameter of 2.5 m and the length of 700 m was vertically connected with a float and a flexible joint. However, the CWP broke off in a storm during the installation, thus the sea experiment was forced to abandon [6]. This was before the beginning of offshore oil and gas industry; therefore, this was due to a lack of knowledge of offshore engineering.

(2) First boom

The oil crisis in 1973 triggered a growing interest in OTEC, along with other natural energy sources. Many projects from the United States, Japan and France made rapid progress on the feasibility study and the component technologies [1,7–9].

There is a considerable amount of report on the preliminary design from the individual groups supported by the U. S. Department of Energy (DOE) or from the "sunshine project" in Japan. The early feasibility studies demonstrated that a 100-400 MW floating plant is necessary to achieve commercial power production at competitive cost. Meanwhile, a required flow rate of deep seawater intake was predicted as about 3.3 m^3/s per 1 MW [10]. Due to the need to reduce the water head loss, a single pipe with a diameter of around 10 m and a maximum internal flow velocity of 2-3 m/s was firstly planed for a commercial scale plant. This has highlighted the need for the development of a large-diameter CWP and the system integration with a floating platform and a position keeping system to optimize the cost.

For example, TRW systems group (1975) [11] and Lockheed corporation (1978) [12] have widely evaluated the quantitative technical feasibility, accessibility, maintenance, risk and cost of a floating platform, such a ship, barge, semisubmersible and spar for a 100 MW plant. As a result, a rectangular and a circular barge were highly evaluated. Note that a deep-water mooring system was not well established at that time; thus, the dynamic behavior of the floating platform and the mooring system seem to be poorly examined.

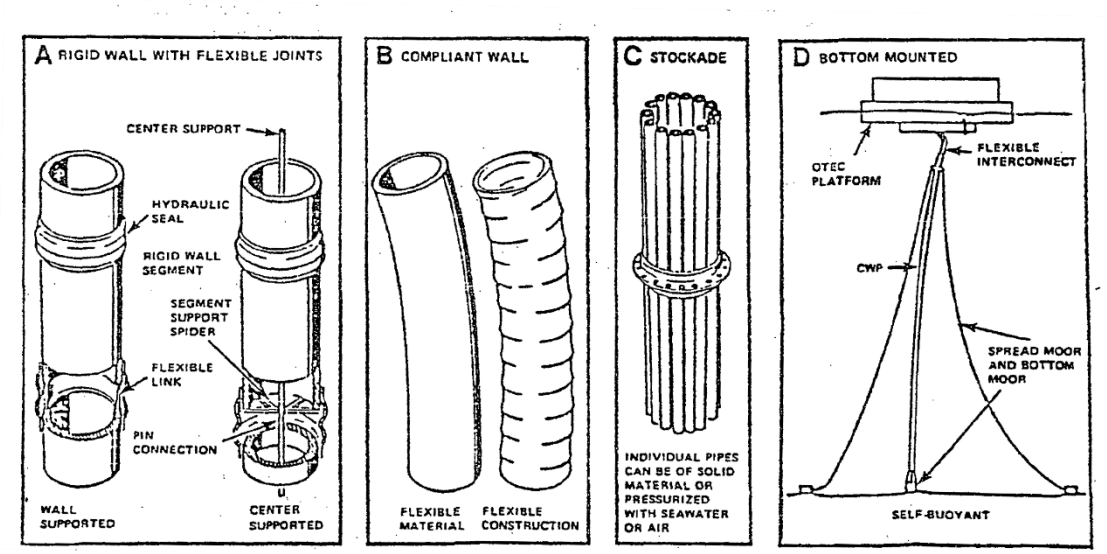

Fig. 1-4 Structure category of the CWP proposed by McGuiness [17].

Meanwhile, Paulling [13] developed a frequency domain analysis method for the coupled platform – CWP system by using the finite element method with beam elements. As the same time, two other computer codes which are frequency domain coupled analysis and time domain decoupled analysis, were developed and three codes were totally compared for a test of their relative accuracy and computational costs [14]. Griffin [15] considered the application of Vortex-Induced Vibration (VIV) for the design of CWP and argued that the existing model could be directly applicable in the Reynolds number range for a 10 m diameter-pipe.

Subsequently, important preliminary works of CWP were carried out including: extensive designs of structure, material, joint system with hull and installation, as well as the assessment of those risks and costs [16–18]. McGuiness [17] has categorized the structure and the material and of the CWP as, the structure: A. rigid, B. compliant, C. stockade and D. bottom-mounted (shown in Fig. 1-4), the material: reinforced concrete, steel, plastic and elastomer. The research group evaluated a total of 67 preliminary designs of the combination of these categories. As the result, a rigid pipe made as Fiber Reinforced Plastic (FRP) sandwich wall was rated as the most promising candidate. In addition, the group also designed three freely rotational connectors between the platform and the CWP (a gimbal, ball-socket and universal joint) [16].

The preliminary works led to subsequent detail design and several at-sea tests [19]. In 1979, the Mini-OTEC with the 50 kW closed cycle plant has demonstrated a net power operation at sea for the first time in history [20]. The platform used a barge which has the length of 32 m, the breadth of 10.3 m, and the draught of 1.3 m. The barge was moored at 2.4 km of offshore from Hawaii and the water depth of 915 m with a single buoy mooring. As a part of the mooring line, the CWP was suspended from the buoy. The CWP was fabricated from High-Density

Polyethylene (HDPE) pipes which had the inner diameter of 0.561 m, and the outer diameter of 0.610 m. The element pipes buttwelded together to the total length of 661 m. Although the reported maximum roll angle of the barge reached 15-20 deg, the plant succeeded the operation for 4 months and provided an important data of a plant-operation at sea.

Subsequently, the OTEC-1 performed an at-sea experiment of the subsystems such as heat exchangers, pumps and CWP in 1980 and 1981 [21–23]. The ship-shaped platform was converted from a tanker constructed in 1943. The dimensions of the tanker were the length of 160 m, the breadth of 21 m, and the draught of 12 m [24]. As a position keeping system, single weak mooring and thruster were designed to allow the platform to drift around 28 km of offshore from Hawaii [25]. The CWP was made by bundled three HDPE pipes, which had the inner diameter of 1.34 m, the outer diameter of 1.22 m, and the length of 671 m. As one of the important outcomes, the experiment demonstrated the installation of the CWP by upending and the connection to the platform. In addition, the rotation of 30 deg at the gimbal between the platform and the CWP was recorded under the about 1.0 m/s of current velocity [26]. This confirmed the structural reliability of the gimbal, but also reveals the need for improving the drag force estimation and a design that suppress the rotation.

Meanwhile, several at-sea experiment to verify the analysis of the platform and CWP was conducted [27,28]. The group of Deep Oil Technology and The Johns Hopkins University Applied Physics Laboratory conducted an experiment using the steel pipe with 150 m long and 1.5 m in outer diameter and the test platform Deep Oil X-1 moored by a three-point catenary mooring [29]. Although this pipe did not strictly meet a scale law with an actual CWP, the test has confirmed that the necessity of a coupled analysis of the CWP and platform. In addition, it has been reported that the pipe broke at the flanged connections and 120 m of pipe were lost due to resonance with waves during the experiment. Furthermore, a FRP pipe which had the length of 122 m and the diameter of 2.4 m was made for a prototype of a 40 MW OTEC CWP [30]. The experiment at offshore of Hawaii was conducted with the pipe which was suspended from a barge with a gimbal joint. A statistical response that was computed with correctly modeling the drag and added mass coefficient were in good agreement with the experimental measurement.

(3) Post first boom

Commercializing an OTEC at competitive cost was considered economically and technically unfeasible, hence most projects were unfortunately abandoned before they provided any knowledge of the commercial operation. In summary, the researchers and engineers were limited to confirm the applicability of existing technologies. Nevertheless, research institutes have been

established such as Hawaii and at Saga University, Japan to continue to study on OTEC and deep seawater utilization.

The National Institute of Ocean Technology (NIOT) in India built a 1 MW floating plant [31]. The platform used a barge which has the length of 68.5 m, the breadth of 16 m, and the draught of 4 m. The mooring system was close to mini-OTEC, in which a HDPE CWP with 1 m in diameter and 1,000 m long was suspended from a buoy as part of the mooring line. Unfortunately, the CWP was broken, and the project had to be abandoned.

Nihous and Vega in 1993 proposed a 100 MW OTEC plantship for hydrogen production and storage [32]. Due to the success of at-sea pilot scale experiment [30], the CWP made as a FRP - syntactic form core with the diameter of 10 m was selected in this design. They stated that a grazing plant with a thruster is the most suitable due to environmental and economical reasons.

In Japan, researchers have focused on an integration an OTEC with a deep-water utilization such as an ocean nutrient enhance. The floating device HOYO performed at-sea experiment of the OTEC system. A steel pipe with 0.45 m in diameter and 236 m long was suspended from a rectangular barge moored by two point mooring [33]. Unfortunately, it was reported that the CWP and its connector with the barge were broken in a typhoon. The Marino-Forum 21 subsequently built the ocean nutrient enhancer TAKUMI (without an OTEC system) [34]. In order to reduce the motion of the platform and CWP, submersible disc was adopted as the floating platform. The platform was moored by a single point mooring. The steel pipe with 1 m in diameter and 175 m long was suspended form the bottom of the platform with a flexible joint and two chains. The system has succeeded in the operation for five years.

(4) Second boom

Climate change issue has led to a renewed interest in OTEC along with other renewable energy sources and CO2 reduction technologies. There are a large number of projects and researches to investigate the economical feasibility from many countries [35]. In addition, there are reported several preliminary designs reflecting a deep-water offshore oil and gas development.

Korea Research Institute of Ships and Ocean (KRISO) carried out a field test of 1 MW OTEC plant with a rectangular barge in 2019 [36]. The plant succeeded the largest power production by OTEC.

Lockheed Martin Corporation that was one of contributors of the first boom has resumed the development of OTEC. The group reported a 100 MW semisubmersible plant [37], its 5 MW and 10 MW pilot plants [38] and 2.5 MW mini-spar pilot plant [39]. In the preliminary design of the

CWP with the diameter of 10 m, they proposed a FRP composite pipe designed to be fabricated on the platform as the most economical and low-risk candidate. The fabrication process was validated with the demonstration of 4 m diameter scale [6].

The design load of the CWP and joint with the platform was computed using a state-of-the-art time-domain coupled behavior simulation of the platform, mooring system, CWP and the gimbal joint [40]. The simulation was compared with a tank experiment [41,42]. As a result, the simulation which regards the system as a fully coupled model was in good agreement with the experiment. Meanwhile, scaling the experimental pipe has been limited in the design; therefore, there is still unclear about an effect of the geometrical similarity and internal flow.

SBM Offshore discussed the applicability of technology of a Floating Production, Storage and Offloading (FPSO) with a preliminary design converted oil tanker, container ship and barge [43]. They have also designed the 4 m long FRP pipe for 10 MW plant; however, they have used a decoupled approach [44]. Furthermore, the group carried out a series of tank experiment to examine an effect of internal flow [45,46].

Overall, these works suggest the efficacy of a knowledge of the deep-water offshore oil and gas development on the floating OTEC plant. The classification of an OTEC plant has been provided by the review by Zhang [47]. In addition, a technical requirement of OTEC plant has been provided by Bureau Veritas (BV) [48] and the International Electrotechnical Commission (IEC) [49].

On the other hand, the CWP that has been successfully operated at sea are limited to 1-2 m in dimeter for demonstration plants and at-sea test. While a large diameter CWP still remains one of the most challenging components in OTEC to be overcome, in contrast to the growth of deep-water mooring, risers and floating structures. Several tank experiments were conducted to verify a coupled analysis program and VIV problem of the CWP [50,51]. Furthermore, Adiputra and Utsunomiya put forward self-induced vibration of the CWP due to steady internal flow as a critical issue to be designed [52,53]. These studies have outlined a need for a systematic understanding of the dynamics and design methods of the CWP and its connector with the platform.

1. 3 **Study Objective**

A commercial scale OTEC plant requires a large amount of seawater to drive the heat engine from only a 20 ℃ of temperature difference. For a 100 MW floating plant, about 10 m diameter CWP will be required to intake deep seawater. The almost all the studies and projects presented in previous section substantiate the importance of understanding of its dynamics and the structural reliability.

Comparing to an offshore oil and gas riser, the novelty of CWP is that: (i) the diameter is significantly large, (ii) it contains a large mass flow rate, (iii) it is always hanged off even during operation, and thus (iv) the lower end is open in underwater. Although prior studies have made a significant contribution to commercialization, the design methodology has been developed for individual projects, and there seems to be no systematic analysis and design methodology that focuses on these mechanical characteristics.

The overall objective of this thesis is to clarify the design methodology of a floating OTEC plant and its mechanical characteristics through a preliminary design of a 100 MW plantship. In particular, this thesis examines two main research questions:

(1) The dynamic interaction between a ship-shaped platform, a deep-water mooring and a CWP is expected to be particularly strong. However, there seems to be unclear on its influence on design and validity of numerical simulation. The coupled response characteristics will be discussed using numerical simulation and simplified modeling approaches.

(2) As a critical phenomenon for the CWP, there are concerns about a self-induced vibration due to large momentum of internal flow. However, our knowledge of the dynamics of such pipes is based on limited experimental studies and the dynamics would seem to be not definitely established. This issue is considered to be an important outstanding question in the dynamics of the CWP and will be pursued it experimentally and theoretically.

1. 4 **Study Case**

As a study case, this study selects the concept of a 100 MW-NET OTEC plantship. The findings from this study case might be applicable to other platform geometries and ocean sites. In this section, the specification of the concept and its current status are introduced prior to this main subject.

As background of this concept, a Levelized Cost Of Energy (LCOE) of a 100MW-scale OTEC has been estimated as 150-280 $/MWh in 2015 [54]. Capital costs of the platform, mooring and CWP account 20 % of which. As mentioned by Langer [35], the estimation seems to have large uncertainty and does not consider the effect of technical learning. These economical works suggest the need for reducing the capital cost of the floating plant and updating the concept that reflects the knowledge of offshore oil and gas development.

Adiputra et al. [55] have proposed a 100 MW-NET OTEC plantship which reflected design philosophy of FPSO. To attempt to reduce the capital cost, the platform is converted from a pre-

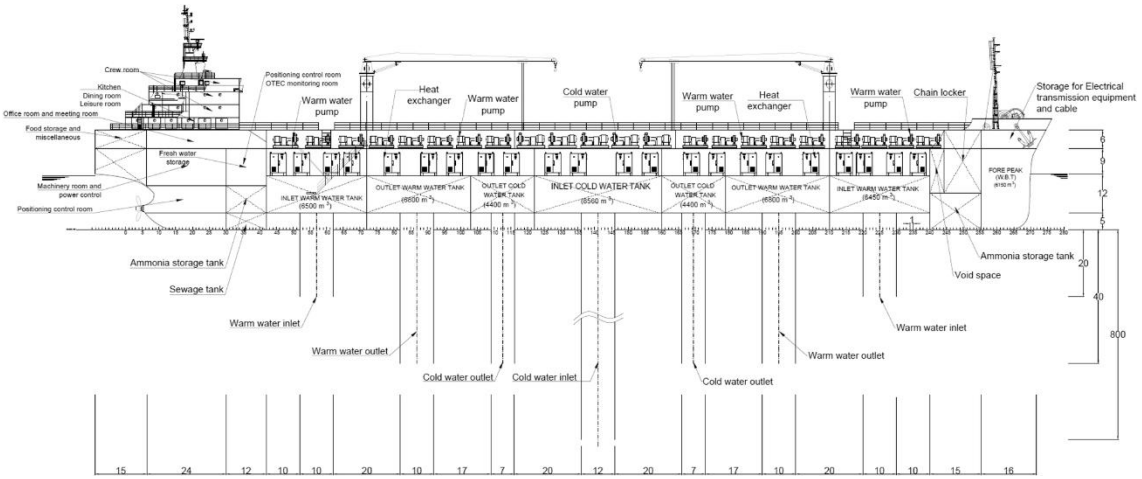

Fig. 1-5 General arrangement of 100 MW-NET OTEC plantship [55].

owned ship. Indonesia is chosen as the target site because of its high geographical and economical potential. Additionally, Indonesia in which there is no tropical cyclone makes it possible to implement a ship-shaped floating structure, which generally has a large response.

Fig. 1-5 shows the proposed general arrangement for a Suez-max oil tanker. Warm seawater and cold seawater are aspirated through each of inlet pipe, and they are temporarily stored in the seawater tank (surge tank). Subsequently, the seawater pumps supply seawater to the heat exchangers. After the production process, the seawater will be discharged to a depth of same temperature through the discharge pipes. As the most important component, the CWP is the length of 800 m and the inner diameter of 12 m to deliver 235 m^3/s of deep seawater.

Yet, the mooring system and risers were not specified in this concept. Hence, clarifying these designs and establishing their design methods would be valuable for improving resolution of an economical and technical feasibility.

1. 5 **Outline**

This thesis is divided into 6 chapters as follows. Fig. 1-6 shows an overview of design procedure of a floating OTEC plant based on BV[48] and IEC [49]. In Fig. 1-6, the positionings of each chapter are marked.

In this chapter, the general overview of OTEC was firstly introduced. Subsequently, the development history and current status of a floating OTEC with regard to offshore engineering were reviewed to clarify the position and the overall objective of this study.

In chapter 2, the environmental conditions, hull geometry, mooring system and CWP are configured for analysis model. Preliminary designs by several combinations of a flexible joint, a

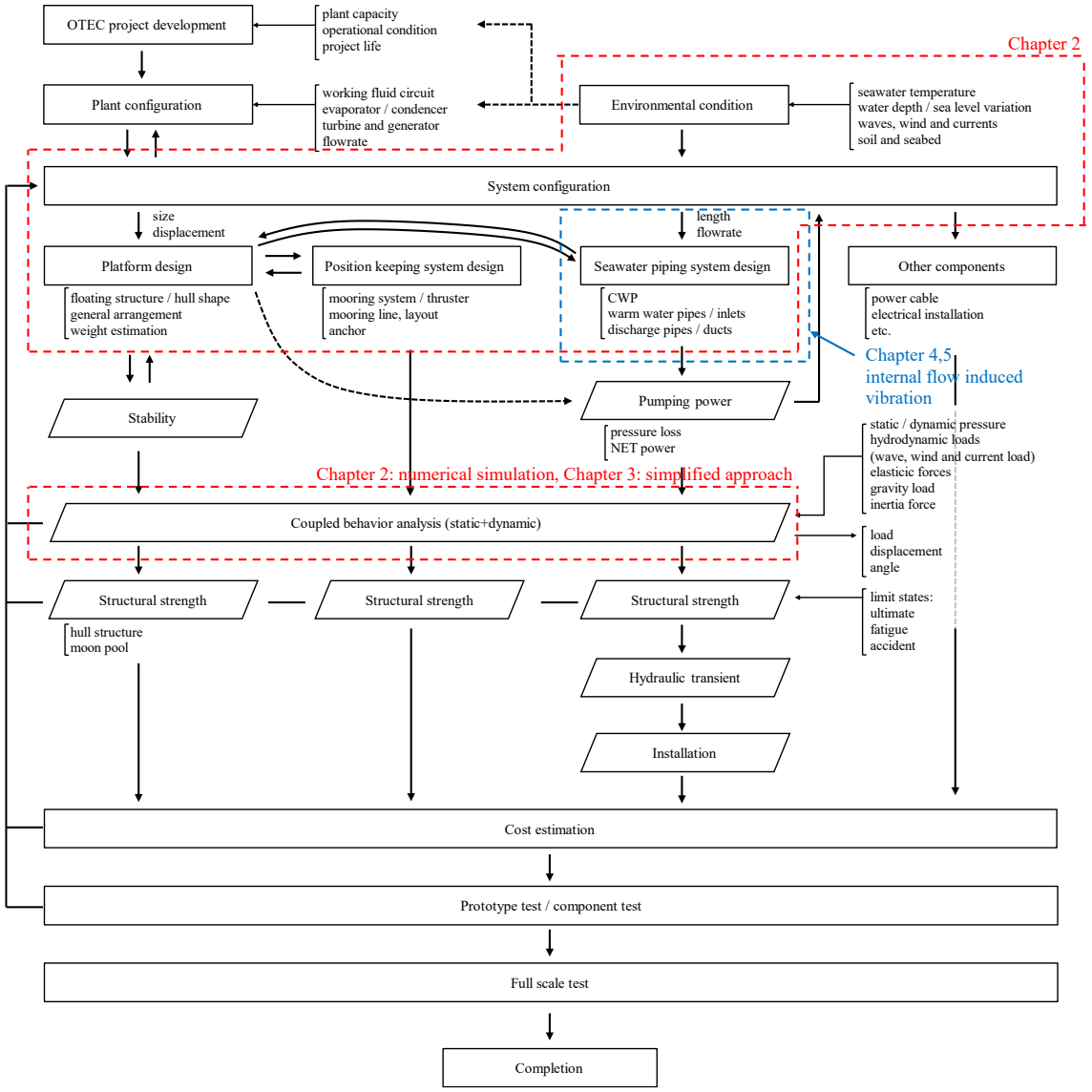

Fig. 1-6 Design procedure of a floating OTEC plant.

clump weight for the CWP, taut mooring system and catenary mooring system will be compared on their dynamic behavior by using OrcaFlex. Two kinds of models which are calculated by direct coupled system and only CWP under the forced oscillation obtained by the moored ship without CWP will be also compared in order to examine those interactions.

The aim of chapter 3 is to construct a simplified analysis model/method to easily comprehend the coupled responses characteristics of the floating platform, CWP and mooring system for the preliminary design stage. Additionally, the influence of the design parameters for CWP to the coupled responses will also be investigated by a parametric study combining the bending stiffness, the linear density, and the boundary conditions, as a preliminary design methodology using present model.

In chapter 4, a tank experiment using a polycarbonate pipe with 4 m length is reported. Subsequently, the observations are compared with existing equation of motion of a fluid-conveying pipe and its stability analysis.

In chapter 5, a new model of the inlet flow field, which plays an important role on stability, will be presented based on a CFD analysis. Then, the result and discussion with regard to the stability and dynamic behavior of CWP will be shown.

Chapter 6, concluding remarks, states the general conclusions obtained above and future works.

2 MOORING / RISER ANALYSIS AND DESIGN

2. 1 Introduction

Climate change and energy issue has led to a surge of interest in OTEC in particular in remote islands such as Okinawa and Hawaii and low-latitude island countries such as Indonesia. Although a floating OTEC plant demonstrated a net power production, the economical and technical feasibility at competitive cost has been a major issue. A large number of feasibility studies have suggested that a 100 MW floating plant is necessary to achieve commercial power production at competitive cost. These studies also suggest the need for reducing the capital cost of the floating plant and updating the concept that reflects the knowledge of offshore oil and gas development.

From the above background, Adiputra et al. [55] have proposed the 100 MW OTEC plantship, which is converted from a pre-owned ship for an effort to reduce the capital cost. The preliminary work indicated that a Suez-max oil tanker is the best candidate. Comparing well established offshore structure such as FPSO, the distinction of the OTEC plantship is the CWP which has the length of 800 m and the inner diameter of 12 m to be attached. Following the previous study, the environmental conditions, hull geometry, mooring system and CWP are configured in the first half of this chapter. Specifying these designs and establishing their design methods would also be valuable for improving resolution of an economical and technical feasibility.

Generally, a commercial scale CWP requires coupled analysis of the platform, mooring and CWP due to the huge mass of the internal fluid and added mass. In particular, a dynamic interaction between a ship-shaped platform and over 10 m diameter CWP is expected to be strong. However, there seems to be unclear on a quantitative magnitude and its influence on the design procedure.

The objectives of this chapter are to specify the hull, mooring system and CWP and to investigate the magnitude of the interaction between platform and CWP through a numerical simulation. Thus, the time-domain coupled analysis is carried out using the commercial software OrcaFlex, which is coupled dynamics code of floating structure and line structures.

2. 2 **Preliminary Design**

2.2.1 **Hull geometry**

The study case is a 100 MW-NET OTEC plantship in this study. The previous study [55] has indicated that a Suez-max class oil tanker is one of suitable candidates. Since the concept is given as conversion from a pre-owned ship on the premise, here an openly available hull geometry is assumed as the plantship.

The series ship of KRISO Very Large Crude-oil Carrier (KVLCC) has been provided to be used as benchmark of Computational Fluid Dynamics (CFD) and a tank experiment. In this study, the KVLCC2M [56] is assumed as the hull geometry and its main dimension is modified to satisfy a typical Suez-max class oil tanker. The bilge keel with the length of 82.5 m ($0.3L_{pp}$) and 1.0 m wide is additionally installed in order to reduce roll amplitude.

Dynamics of floating body will be influenced not only the hull geometry but also the location of center of gravity and the weight distribution. To provide sufficient material for the preliminary design stage, the schematic layout of OTEC components and tank plant shown in Fig. 2-1 are assumed here. Additionally, Table 2-1 shows the main dimensions, the center of gravity and gyrational radius estimated with Fig. 2-1 in the case of the full load condition of the platform. The estimation could not distinctly consider the weight distribution of ship structure and piping system onboard. However, it may be sufficient to design mooring and risers in preliminary stage.

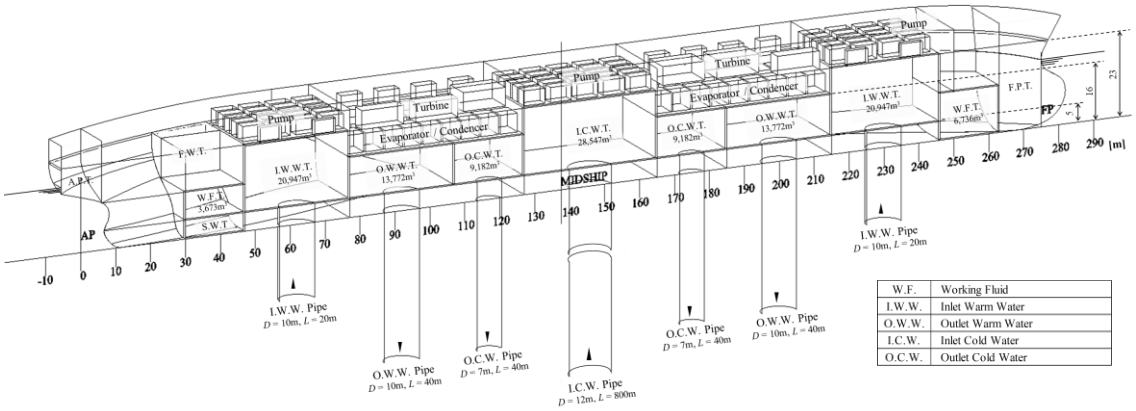

Fig. 2-1 Preliminary layout of the OTEC plantship.

Table 2-1 Main dimensions of the OTEC Plantship.

Length(o.a.)	L_{oa}	286	m
Length(p.p.)	L_{pp}	275	m
Breadth	B	50	m
Depth	D	29	m
Draught	d	17.9	m
Block coefficient	C_B	0.8099	
Displacement	W	204,035	ton
Center of buoyancy from Midship	l_{cb}	3.4%L_{pp}	
Center of buoyancy above B.L.	$\overline{KB}$	9.36	m
Center of gravity above B.L.	$\overline{KG}$	13.9	m
Non-dimensional radius of gyration	K_{xx}/B	0.280	
	K_{yy}/L_{pp}	0.229	
	K_{zz}/L_{pp}	0.231	

2.2.2 **Mooring system and risers**

A floating OTEC plant ship is broadly divided into a grazing type and a mooring type [49]. In the grazing type, the plant is drifted with keeping an allowable range by a thruster or jet of discharge water. Although this type has been considered superior in environment, it is not found in modern conceptualization. Thus, this study focused on the mooring type to consider the applicability of knowledge of offshore oil and gas technology.

The mooring system is divided into a single point mooring and a spread mooring system [57]. The single point mooring may be suitable for a demonstration plant and a detachable plant; however, it would not be sufficient for a commercial scale plant. Furthermore, a turret mooring which is often adopted for a FPSO in a severe ocean would be not suitable to this concept here. This is because that: the large diameter-CWP cannot be concentrated with other risers and mooring lines, while the case that CWP is installed at bottom of hull would interfere the mooring lines, and it is overdesign for a calm ocean such as Indonesia. The spread mooring system is one of economical candidates for a calm and directional sea state.

For these reasons above, this study focusses on a spread mooring system. The spread mooring system is additionally divided into two mooring systems: a taut mooring system and a catenary mooring system. In this study, both alternatives are designed, and their response characteristics are compared focusing on the response of a CWP. The seawater intake and discharging risers are individually connected to the hull structure through the moonpool. These are always hanged off even during operation, and the lower end is open and free in underwater.

The plantship is moored head to the strongest wave incident direction on a site of 1,000 m of water. The mooring layout is shown in Fig. 2-2. As shown in Fig. 2-2, each mooring line is

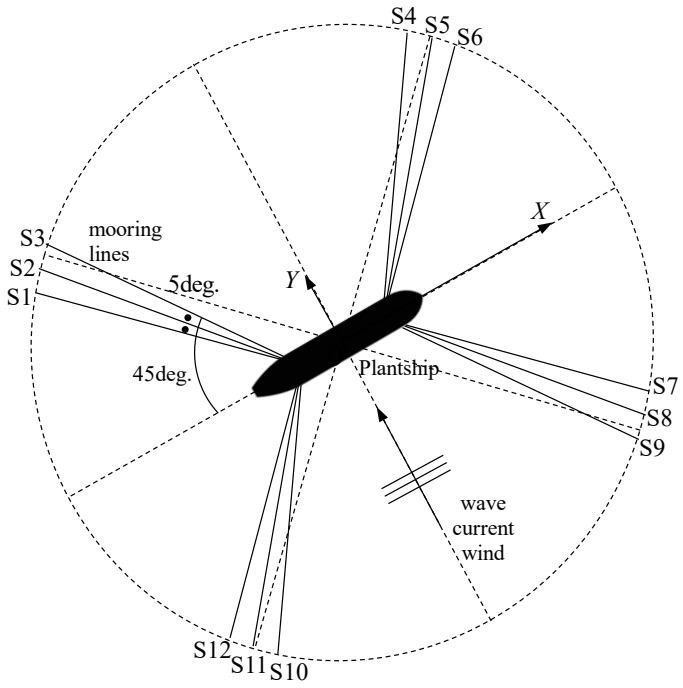

Fig. 2-2 Layout of the spread mooring system.

deployed from the starboard/port of the bow/stern to 45 deg direction. To increase redundancy after a single mooring line breakage condition, two mooring lines are additionally deployed from each direction with angular difference of 5 deg.

The catenary mooring system is mainly configured with the R4 grade studless chains of 111 mm in the nominal diameter and drag anchors. The mechanical properties from Ref. [58] are shown in Table 2-2. The total arc length of the single line is 2,800 m in which the arc length between the fairlead and the touch down point is 1,400 m.

The taut mooring system is mainly configured with polyester ropes of 212 mm diameter and suction anchors. The mechanical properties from Ref. [59] are shown in Table 2-2. The length of the single line is 1.7 times of the water depth. The design requirement and validation of these mooring systems are given later in section 2.4 and section 2.5.1, respectively.

The CWP and the joint structure are especially important components to be overcome. However, this study firstly concentrates on the design method and the dynamic characteristics prior to the detailed design. Several preliminary works have identified a FRP pipe as the most feasible candidate. This study thus assumes the syntactic foam core sandwich FRP wall from Ref. [32] as a tentative material and structure. Table 2-3 is the mechanical properties of the pipe which is assumed as one-dimensional beam.

Table 2-2 Mechanical properties of mooring lines.

		studless chain	polyester rope
Nominal diameter		111 mm	212 mm
Length		2,800 m	1,750 m
Drag coefficient	axial	1.15	0
	normal	2.4	1.6
Added mass coefficient	axial	0.5	0
	normal	1.0	1.0
Grade / Type		Grade R4	OceanMax
Axial stiffness		1,052 MN	294 MN
MBL		11,854 kN	12,263 kN
Weight in sea water		245 kg/m	7.52 kg/m

Table 2-3 Main dimensions of the CWP.

Length	l	800	m
Inner diameter	D_{in}	12.00	m
Outer diameter	D_{out}	12.32	m
Thickness	t	16.0	cm
Material		Syntactic core - FRP	
Density	ρ	1.2	ton/m^3
Young's modulus	E	13,776	MPa
Yield stress	σ_Y	550	MPa

The joint structure between the CWP and hull has also been proposed: a gimbal joint, ball-socket joint, universal joint, and flexible joint with suspended chains [16,34]. Within the purpose of the global behavior analysis, their mechanism can be regarded as a rotational spring or a pinned joint. In addition, a sinker may be required to be installed at the lower end to prevent excessive rotation of the joint due to currents acting on the CWP. This study considers these as the design parameters.

2.2.3 **Environmental conditions**

There are several design limit states of the structure of hull, mooring system and CWP: Ultimate Limit State (ULS), Fatigue Limit State (FLS), Accident Limit State (ALS) and Serviceability Limit State (SLS). In addition, the operating conditions would be applied in combination with a specific environmental condition. For the OTEC plant, there are parked condition, production condition, and transit, installation and maintenance conditions [48]. In order to first conduct a preliminary design, this study evaluates the ULS, which may cause under a combination of the parked condition and an extreme environmental condition.

Table 2-4 Environmental conditions.

Water depth		1,000	m
Waves / 100yr.	H_s	$7.3 \times D(\beta)$	m
	T_p	11.1	s
	Spectrum	JONSWAP (γ = 2.79)	
Current / 10yr.	V_{c0}	0.85	m/s
	Profile	1/7 Power law	
Wind / 100yr.	$V_{w,\ 1\ hour}$	28.6	m/s
	Spectrum	NPD Spectrum	

The design life of the plantship is assumed 20 years and the plantship moored a fixed location on 1,000 m of water in Indonesia. An environmental data at the specific location is required; however, any specific material or survey could not be found. Thus, this study uses the convenience data from Ref. [58] of waves, wind, and current in the South China Sea (non-typhoon), which is nearby the site and has a calm environment. The statistics are shown in Table 2-4.

Ocean waves for 100 years return period is represented as the significant wave height of 7.3 m and the peak period of 11.1 seconds. The wave spectrum is assumed as the JONSWAP spectrum of $\gamma = 2.79$. The directional character of the wave is additionally assumed with a coefficient below,

$$D(\beta) = \frac{1+\cos\beta}{2}, \tag{2.1}$$

where, β is a clockwise incident angle from the head seas.

Wind for 100 years return period is characterized by a 1 hour mean wind speed and the time-varying components are assumed as the NPD spectrum. Current for 10 years return period is represented as a surface velocity of V_{c0} and a vertical distribution is assumed as the 1/7 power law.

2. 3 Numerical Simulation

2.3.1 Coordinate system

The time-domain coupled analysis of the hull-mooring-CWP system is carried out using the OrcaFlex 11.0b under the extreme environment for 3 hours duration. Fig. 2-3 shows overview of the analysis model, components and coordinate systems.

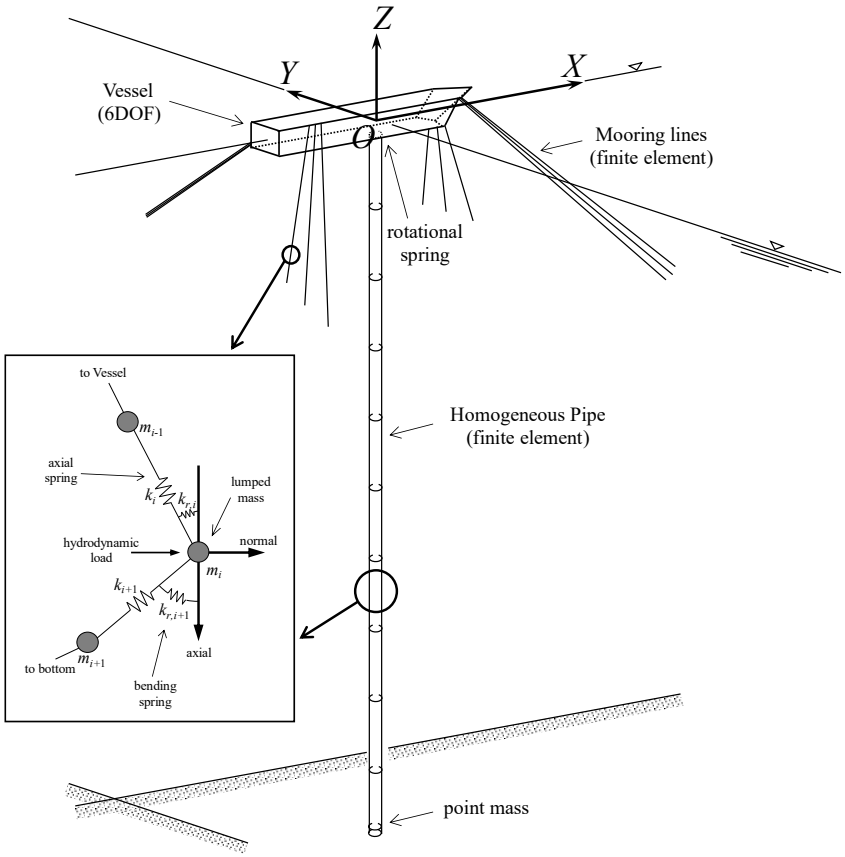

Fig. 2-3 Overview of the analysis model in OrcaFlex.

As shown in Fig. Fig. 2-3, the global coordinate system is defined as a right-handed system on the sea surface and the *Z*-axis is positive upwards. The hull fixed coordinate is placed on the center of gravity, the forward is parallel to the global *X*-axis and the global *Y*-axis is toward the port side of the hull in the initial state.

2.3.2 **Environmental loads acting on the hull**

This section describes the theoretical treats of the environmental forces acting on the hull due to waves, current and wind. At first, the hull is considered as a three-dimensional rigid body.

First order wave forces are calculated with the potential flow theory, in which the fluid is perfect fluid, and the waves and the hull behavior are considered as infinitesimal amplitude. A wave diffraction/radiation analysis is carried out using a High Order Boundary Element Method (HOBEM) with 8 nodes quadrilateral panels [60]. The mesh is shown in Fig. 2-4, in which there are 3,528 panels on the wetted hull surface and 1,789 panels on the water plane. The mesh on the water plane contributes to remove irregular frequencies by the rigid-lid. The RAOs of the center of gravity of the hull in head sea and beam sea are shown in Fig. 2-5.

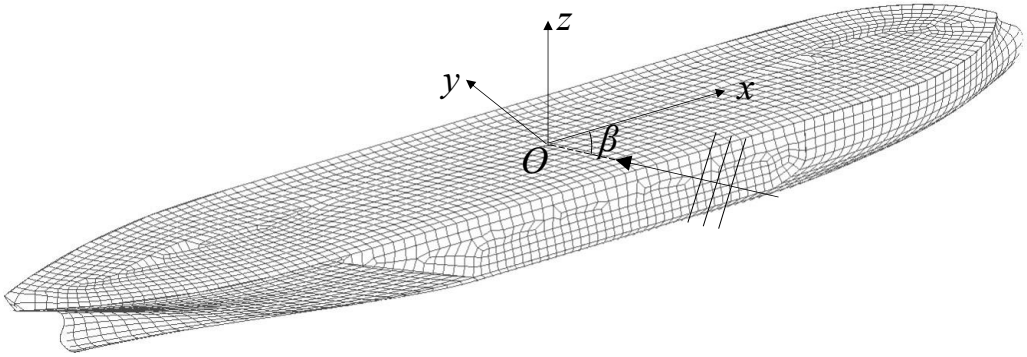

Fig. 2-4 Meshed hull surface and the coordinate system for HOBEM.

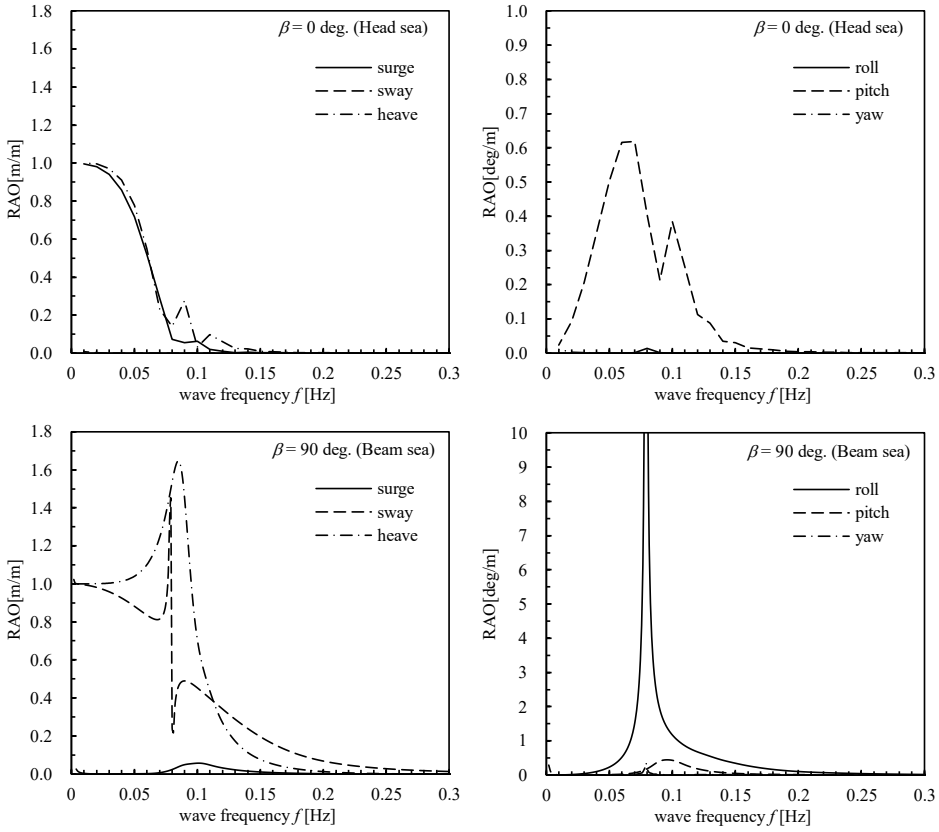

Fig. 2-5 RAO without mooring lines and CWP.

Second order wave force acting on the hull will be the most important in the mooring system. The mean drift force is simultaneously calculated by a far-field method which used the first order velocity potential [61]. In addition, the slowly varying force in irregular waves is calculated by Newman's approximation using the mean drift forces [62]. The significant natural frequencies of the moored floater are only surge, sway and yaw; thus, the method is sufficient to estimate the offset and the mooring tension.

The damping due to viscous flow and flow separation around the hull and the bilge keel plays

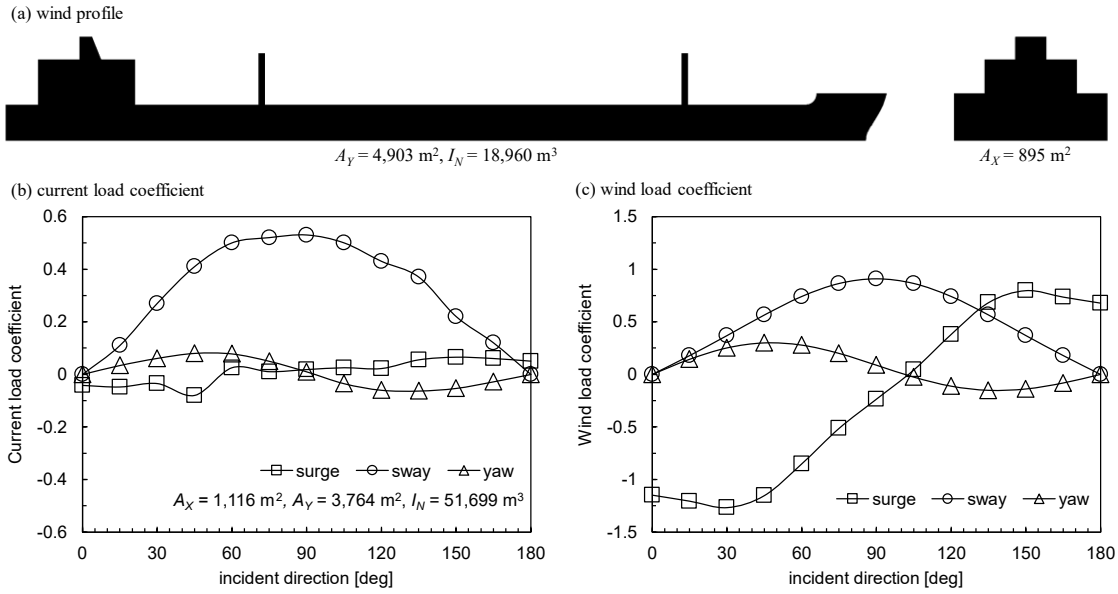

Fig. 2-6 Current and wind load coefficient and wind profile.

important role on the roll. Consequently, the roll peak as shown Fig. 2-5 would be significantly reduced by this effect. This effect is estimated based on Ikeda's method [63]. As a result, the *N*-coefficient with the amplitude of 10 deg is $N_{10\deg} = 0.0295$. For the simulation, the effect is modeled as a linear and quadratic damping moment.

The current and wind force are represented as a drag force acting to the surge, sway and yaw. Thereby drag coefficients depending on an incident angle β are estimated as shown in Fig. 2-6. Current force coefficients are estimated by the empirical coefficients according to an the experiment of a model tanker from Ref. [64]. Wind force coefficients are estimated by adopting a multiple regression model proposed by Fujiwara et al. [65].

First and second order wave force tables by intervals of 22.5 deg of incident directions are inputted to OrcaFlex. Also, current and wind coefficient tables are inputted by intervals of 15 deg for each incident direction. In the time-domain analysis, the forces seem to be interpolated to correspond to the instantaneous attack angle determined from the heading and incident angles.

2.3.3 **Modeling of mooring lines and risers**

The mooring lines and risers are treated as a lumped mass model in OrcaFlex. Namely, the mooring lines are modeled as a mass - axial spring model, and the bending rigidity and shear force of the risers are represented with a rotational spring. The model is superior to the computational cost and would seem to be sufficient to estimate the dynamic behavior.

The hydrodynamic forces induced by waves, current and itself motion are estimated by

Morison's formula. Meanwhile, a hydrodynamic interaction between the hull, mooring lines and risers such as disturbance and wake could not be considered in this study. This may be sufficient for a preliminary design stage, while it should be treated with caution in future detailed design. The added mass coefficient and the drag coefficient of the mooring lines as shown in Table 2-2 are based on Ref. [58]. Hydrodynamic coefficients for the CWP are tentatively estimated: the drag coefficient $C_d = 0.8$ and the added mass coefficient $C_a = 1.0$, based on DNVGL-RP-C205 [66]. Note that the accuracy of this estimation needs further validation and an investigation of the flow structure for the Keulegan-Carpenter number $K_c < 2$ and the Reynolds number $Re > 10^7$.

The effect of internal fluid of the CWP is only considered for the inertia force for lateral displacement. Since the top of CWP is free surface, the axial inertia would be negligible here. As assuming the parked condition, an internal velocity is not considered in this chapter. This effect will be discussed in chapter 4 and subsequent chapters in this thesis.

The CWP is considered as homogeneous along the length and has boundary conditions at the top and the bottom. The top is connected to the hull with a rotational spring of an arbitrary stiffness k_r. At the bottom, a clump weight which neglects the volume and has only a mass m_c is additionally attached.

The dynamic interaction of the hull with other intake and discharge pipes is smaller than that with the CWP. Hence, this study concentrates on the dynamics of the CWP, and other pipes are first neglected.

2.3.4 **Analysis method**

In order to quantitively confirm the interaction between the moored ship and the CWP, two coupled behavior analysis methods are defined, and later, the results are totally compared. Both of analyses are carried out with the implicit integration of the equation of motion with 0.1 second time steps.

(1) Direct coupling

With this method, the individual responses of all components are simultaneously calculated by considering the interaction between the hull, mooring lines and CWP. This method can consider all nonlinearities; therefore, it is generally the most accurate procedure.

In this procedure, the static analysis of all components is first computed. Subsequently, to eliminate a transient response, build-up for 1,800 seconds is performed, then, the dynamic analysis for 10,800 seconds (3 hours) is carried out under a steady state.

(2) One-way coupling

With this method, the coupled analysis of the hull and the mooring is performed first. At this stage, the steady forces acting on the CWP (the weight and current force) are only involved, while the dynamic interaction between them is not considered. Subsequently, the obtained displacement of the hull is applied as a forced displacement to the top of the CWP, in order to analyze the responses under the forced motion, waves and current. The individual procedure of analysis is same.

2. 4 **Design and Analysis Cases**

This section describes the design requirement of the mooring lines to discuss the technical feasibility of these. Moreover, to comprehend the coupled behavior for a further development of CWP, several analytical cases are set up with assuming design parameters of the coupled system.

The design requirement of mooring system is defined in ISO 19901-7 [67], in which the safety factor 1.67 for the intact condition is imposed by using a dynamic analysis under extreme environmental condition. As one of severe conditions, the combination of waves, current and wind is assumed coming from same direction. Then, the simulations are performed at the interval of 15 deg for the incident angle β = 0-90 deg. To obtain the statistical maximum response, six random number seeds for waves and wind are prepared, and the maximum value is evaluated by averaging the result of each seed. Note that the verification process applies the direct coupling denoted above.

Table 2-5 List of the design cases.

Cases	Mooring system	Clump weight	Rotational spring	Analysis method
design 1t	taut	×	○	direct
design 2t	taut	×	○	one-way
design 3t	taut	○	×	direct
design 4t	taut	○	○	direct
design 1c	catenary	×	○	direct
design 2c	catenary	×	○	one-way
design 3c	catenary	○	×	direct
design 4c	catenary	○	○	direct

clump weight m_c = 1,000 ton and rotational stiffness k_r = 40,000 kNm/deg

For the design of CWP, the inner diameter and the length would be preferentially decided based on the planned capacity of power generation. If the material and structure of the CWP are additionally fixed, the dynamic behavior would only depend on the mooring characteristic and the boundary conditions of the CWP. The flexible joints and sinker are needed to reduce the static displacement due to a current. In particular, a relative rotational angle between the hull and CWP is considered important as suggested from the prior at-sea experiments [23].

From the foregoing, this chapter configures the design cases which combine the mooring system, rotational spring k_r, and clump weight m_c as the design parameters. Table 2-5 shows the list of analysis/design cases.

2. 5 **Result and Discussion**

2.5.1 **Verification of the mooring designs**

As an example, this subsection presents results of verification of mooring design using designs 3t and 3c in Table 2-5. Fig. 2-7 shows the safety factor of the mooring tensions of S1-S12 as numbered in Fig. 2-2. The maximum offset of the hull and the maximum tip displacement, internal forces and bending stress of the CWP are shown in Table 2-6 and Table 2-7 for β = 0, 45, 90 deg. The maximum responses of all individual components arise in the beam seas (β = 90 deg). Since the platform is a ship-shaped body, it is very sensitive to short waves in beam seas, while its response in head seas is relatively small. Furthermore, the CWP is significantly affected by the motion of the platform; therefore, the maximum response also arises in beam seas.

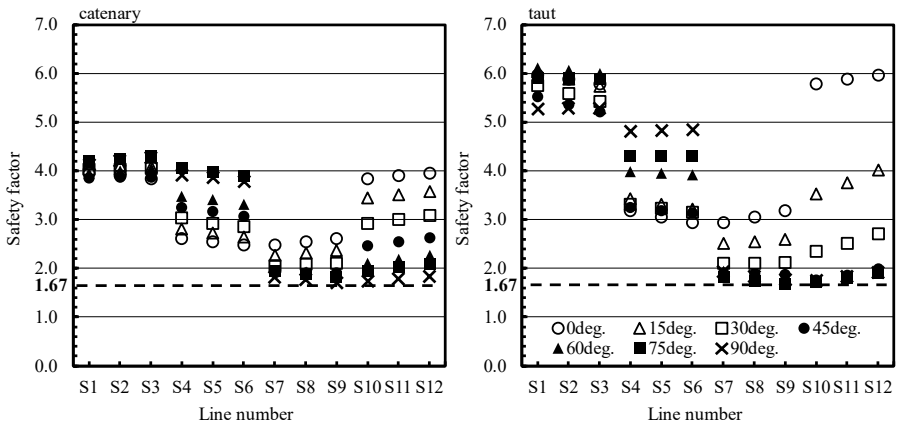

Fig. 2-7 Safety factor of the mooring lines.

Table 2-6 Maximum offset of center of gravity of the planthip.

item	catenary			taut		
direction[deg]	0	45	90	0	45	90
X / depth [%]	13.4	8.4	0.3	2.0	1.7	0.3
Y / depth [%]	0.0	15.4	20.8	0.0	3.2	4.0
Z [m]	2.0	2.0	3.8	2.0	2.1	3.9
roll [deg]	0.0	3.4	6.9	0.0	4.7	10.5
pitch [deg]	1.6	2.0	0.9	1.6	2.4	1.0
yaw [deg]	0.0	32.6	4.5	0.0	14.8	2.8

Table 2-7 Maximum responses of the CWP.

item	catenary			taut		
direction [deg]	0	45	90	0	45	90
X / depth [%]	17.1	10.5	0.5	7.1	5.2	0.0
Y / depth [%]	0.0	20.5	27.7	0.0	8.3	11.3
tension, *T* [MN]	24.2	24.4	26.9	24.3	25.1	27.4
shear force, *S* [MN]	7.0	8.6	10.4	6.7	9.6	10.4
bending moment, *M* [MNm]	473	561	705	468	677	791
axial stress, σ [MPa]	28.3	32.8	40.8	28.2	39.3	45.5

As a result, all mooring lines satisfy the deign requirement of 1.67 as shown in Fig. 2-7. The analysis confirms the validity of both specific catenary mooring system and the taut mooring system for the plantship. The environmental conditions and assumptions were not definitely high resolution, nevertheless this result would suggest that the OTEC plantship with a spread mooring system could be technically feasible at calm and directional environment.

2.5.2 **Static deflection**

In this subsection, the general characteristics of CWP subjected to a current and their influence on the mooring system are discussed. Fig. 2-8 shows the static deflection of the CWP due to the current. Since the FRP-CWP is lightweight and has a large projected area, the rigid body rotation due to current is predominant as shown in Fig. 2-8 (iii). As seen in Fig. 2-8 (i), the static deflection is controllable with the rotational spring k_r, and clump weight m_c. Namely, the rigid rotation is trade-off relationship with an increase of elastic deformation and internal forces by installing them.

While the current force acting on the CWP could be significant in designing the mooring tension. Of the steady forces acting on the hull, the reaction from the CWP accounts for 30% of the total. The force increases the offset of the hull from 94.1 m to 136.4 m for the catenary mooring system, and from 9.0 m to 14.0 m for the taut mooring system. This increase would need to be considered to reproduce the nonlinearity of restoring of catenary lines with the catenary mooring system. Also, for the taut mooring, large offsets might cause snap loading. In fact, the static tension increased 1.3-1.6 times with installing the CWP in this design cases.

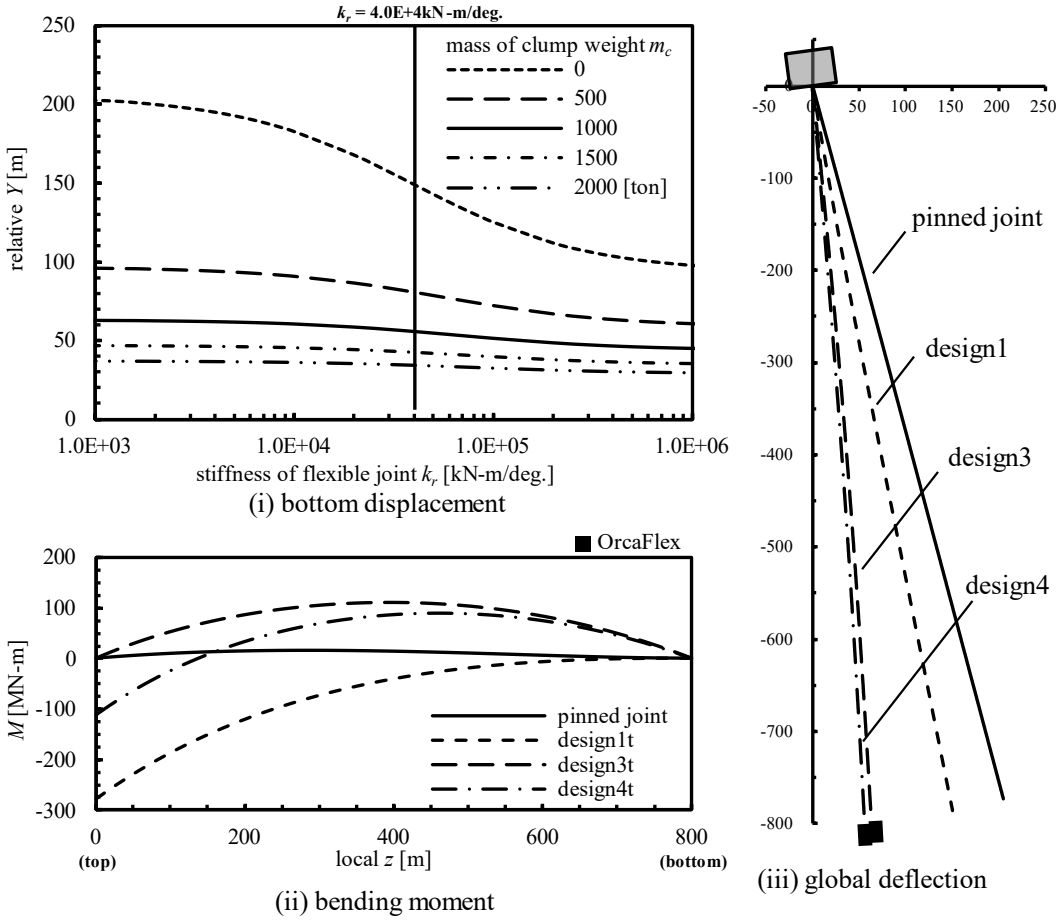

Fig. 2-8 Static deflection of the CWP.

2.5.3 **Dynamic responses**

The result of the maximum responses of the ship is shown in Fig. 2-9. Comparing designs 1 and 2 which are with/without the CWP, the design2 overestimates the maximum value for sway and underestimates the maximum value for roll. As a result, mooring tension is overestimated by 6% for design 2c compared to 1c and by 24% for design 2t compared to 1t.

Comparing designs 1, 3 and 4, there seems to be a slight difference due to the rotational spring

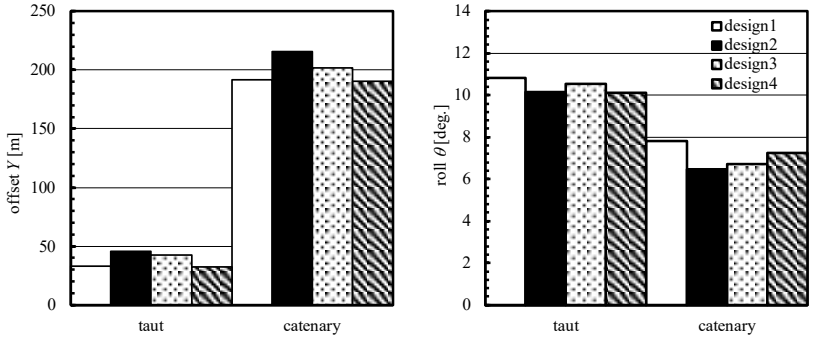

Fig. 2-9 Maximum sway and roll angle of the ship.

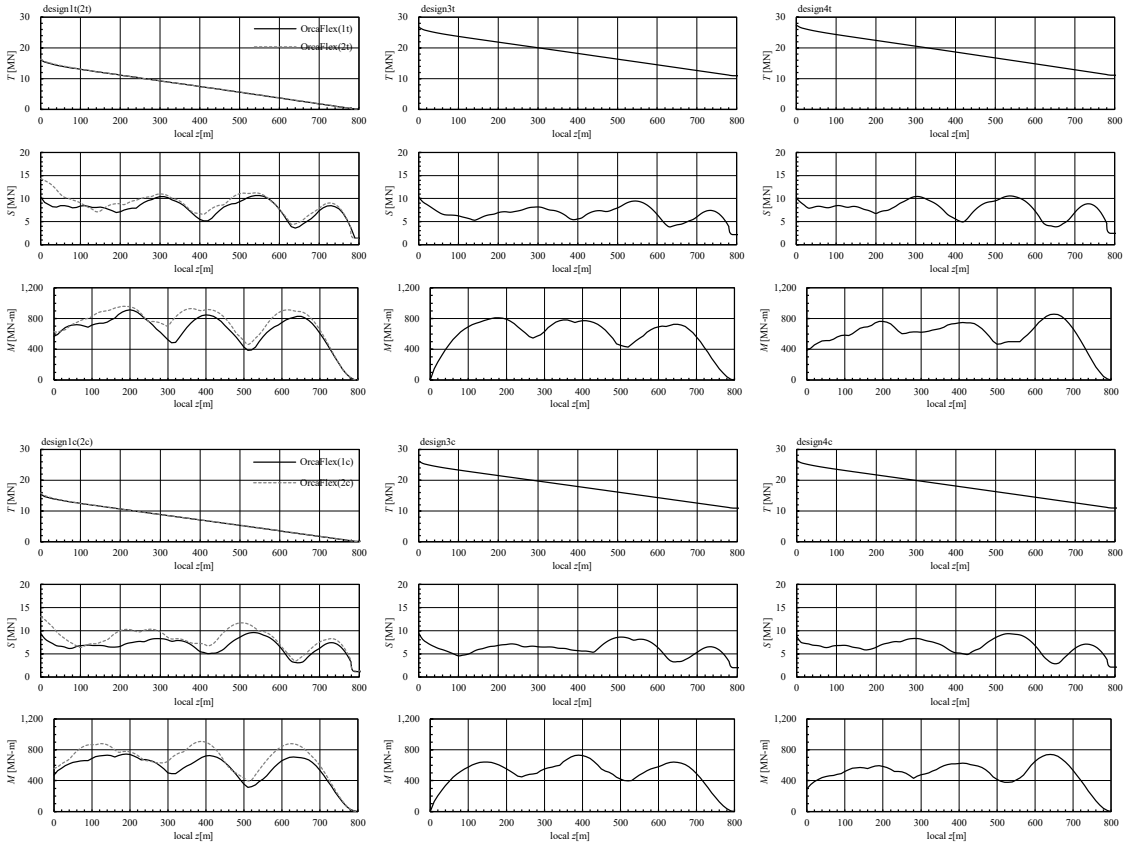

Fig. 2-10 Maximum internal forces.

and clump weight. However, the difference is identified with the static displacement as Fig. 2-8, the impact of dynamic response seems not to be dominant. Fig. 2-9 moreover shows a significant difference by the mooring system. The hydrodynamic forces due to a motion of the catenary chain decrease the roll of the ship.

Fig. 2-10 presents the maximum internal forces, the axial force *T*, shear force *S*, and bending moment *M*, for all design cases in Table 2-5. Interestingly, the dynamic tension due to heave accelerations is observed about twice of the static tension due to the weight. The joint structure between the ship and CWP is generally designed with its weight; however, it highlights needs to consider the dynamic tension. Furthermore, the shear force at the top connection is in order of 10 MN which would also be significant for the design.

The bending moment diagram in Fig. 2-10 also demonstrates that the third mode of the bending motion is predominant response on the CWP. As comparison with the static bending moment in Fig. 2-8 (ii), the dynamic responses at a wave frequency range would seem to be a dominant component for the design. These suggested that a resonance avoidance design should be needed against waves and roll of the ship. The maximum responses can be generally found at 150 m above the bottom end. Meanwhile, when the CWP is connected with a strong flexible joint, the maximum response is found at close to the top.

Comparing designs 1 and 2 in Fig. 2-10, the one-way coupling is suggested to estimate a conservative design load, and the distribution of the maximum response is also different between the two designs. However, caution must be applied to whether these findings can apply to other environmental condition and design cases.

Overall, the amplitude of elastic responses of the CWP in design waves are 0.5 times of the diameter in the maximum. Whereas the relative rotation angle between the ship and CWP has an increase of 5-8 deg from the steady rotation. As mentioned by prior at-sea experiments [20,23], it should be considered to reduce the rotation if the joint mechanism has a rotational capacity.

2. 6 **Conclusion**

This chapter has specified the design cases of the hull, mooring system, CWP and environmental conditions to confirm the technical feasibility and to examine these interactions. A spread mooring system has been considered preferable as a position keeping system. Preliminary designs by several combinations of a flexible joint, a clump weight for the CWP, taut mooring system and catenary mooring system have been compared on their dynamic behavior by using OrcaFlex.

As a result, the analysis has confirmed the validity of both the specific catenary mooring system and taut mooring system for the ship-shaped platform. The environmental conditions and assumptions were not definitely high resolution, nevertheless this result would suggest that the OTEC plantship with a spread mooring system could be technically feasible at calm and directional environment.

As stated in the introduction, specifying these designs and establishing their design methods would also be valuable for improving resolution of an economical and technical feasibility. This work might be helpful to a further feasibility study including more detailed design of a plantship and mooring system and estimation of these cost by an experienced company.

With regard to findings of the coupled analysis approach, it has been found that the interaction is generally significant, and a direct coupling analysis would be more reasonable for the design. On the other hand, the one-way coupling has been suggested to estimate a conservative design load. Since the FRP-CWP is lightweight and has a large projected area, the rigid body rotation due to current is predominant. The static deflection could be controlled by installing the flexible joint at the top and the clump weight at the bottom. While the modes of the dynamic response due to the ship motion has been predominant for the design loads.

Caution must be applied to whether these findings can apply to other design cases. Further work needs to be carried out to determine the design parameters over a wider range. In addition, the validity of the analysis model should be verified through a tank experiment.

3 COUPLED MOTION CHARACTERISTICS OF CWP AND MOORED SHIP

3. 1 Introduction

A floating OTEC plant requires a large-diameter CWP to be attached to a floating structure. For the design of the mooring system and the CWP, a coupled analysis of a floating body, mooring system and CWP may be employed due to the huge mass of the internal fluid in the CWP. Previous chapter has highlighted that the interaction is generally significant, and a direct coupling analysis would be more reasonable for the design. However, the mechanism of the coupling remains unclear, and a systematic understanding of the response characteristics, such as the natural frequency and frequency response of the platform and CWP, would be necessary.

In the mooring and riser design for FPS/FPSO, it is well known that the interaction cannot be neglected in deep water, and a coupled analysis is therefore required [68,69]. Cruces Girón et al. [70] have reviewed and classified design methodologies of mooring systems and risers, and as an efficient method, they have proposed an integrated design which selects the levels of interaction corresponding to the design stages. Although the CWP is different from the risers for FPS/FPSO where it is larger in diameter than the risers and always hanged-off state, the OTEC system will require the coupled analysis as well. Several numerical works have mentioned that stresses computed by a coupled model are different from the decoupled model [13,40].

For the structural design of CWP, a fully coupled analysis of a floating body, mooring system and CWP has been commonly employed since the beginning of OTEC development. Paulling [13] developed a frequency domain analysis method for the coupled system by using the finite element method with beam elements. The hydrodynamic force acting on CWP was predicted with the equivalent linearization form of the quadratic drag force. At the same time, two other computer codes which are frequency domain coupled analysis and time domain decoupled analysis, were developed and the three codes were totally compared for a test of their relative accuracy and computational costs [14]. Moreover, those theoretical evaluations were validated with experiments on small and medium scales, and it was observed that the code developed by Paulling [13] was in good agreement with the experiments [27,29,30]. Shi et al. [40] reported the coupled analysis for a 100 MW semisubmersible plant by two different state-of-the-art time domain simulation codes. One of those codes was also validated by comparing with a tank test at a scale of 1:50 [41]. In the previous chapter, this study has also carried out the coupled analysis for the preliminary design of mooring system and CWP for a 100 MW ship-shaped plant by using

commercial software OrcaFlex. However, the analysis has not yet been validated with a scale experiment due to the limitation in the depth of the wave tanks.

These previous studies have focused on establishing the design method and discussing feasibility. Although the studies have made a significant contribution to commercialization, the design methodology has been developed for individual projects and has hardly been systematized [47]. The numerical analysis has been validated only by comparing multiple codes and experiments in deep water tank, which is costly and time consuming to develop. As far as we know, there exist few studies focusing on basic characteristics for rational design, such as the coupled response and the sensitivity of design parameters. In addition, although a state-of-the-art time domain coupled analysis is accurate and practical at the middle to final design stages, it requires high computational resources and is not suitable for the early design stage dealing with a large number of design trials.

The aim of this chapter is to construct a simplified analysis model/method to easily comprehend the coupled responses of the floating platform, CWP and mooring system for the preliminary design stage. We formulate the coupled system of an OTEC floating plant based on the basic principles of mechanics in the first of this paper. Such formulae are based on a classical method; however, they mathematically yield tractable and essential characteristics. The model/method will hence facilitate the preliminary design of an OTEC floating plant and explanation of the results of numerical simulations and model experiments.

Subsequently, this chapter verifies the applicability for a practical design and limitation of the present model. The preliminary design of a 100 MW ship-shaped plant is configured as a study case to compare proposed model with time domain analysis by using OrcaFlex. This chapter additionally discusses a sensitivity of design parameters of CWP including linear density, bending rigidity, top joint system and clump weight at the bottom, as a preliminary design methodology using present model.

3. 2 **Formulation**

An OTEC floating plant is configured with a floating structure, mooring system and riser system. In a typical modern design of floating plant, the floating body is directly moored with multiple lines and CWP is hanged off from the floating body. The floating structure has been proposed as semisubmersible, spar and ship. The higher rated structure for CWP has been rigid wall [17] and can be handled as a continuous beam. The joint system between floating body and CWP is considered as a fixed joint, a gimbal (pinned) joint or a flexible joint. If the wet weight is not large, a clump weight which is additionally attached at the bottom of CWP is effective to

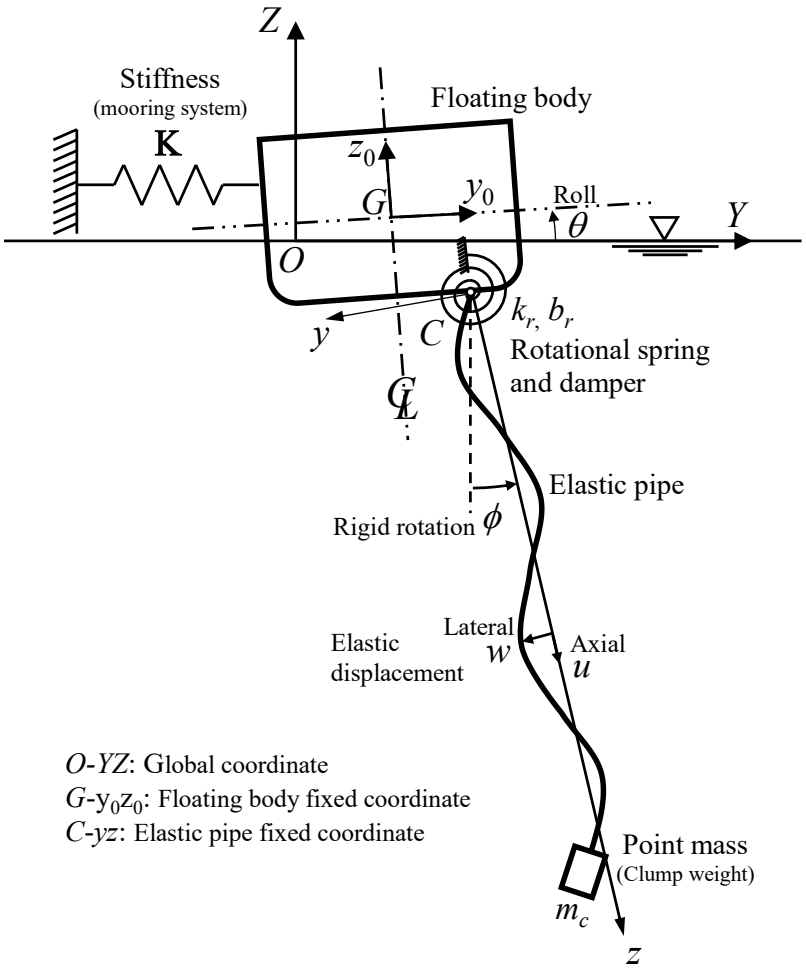

Fig. 3-1 Definition of symbols and the coordinate systems.

reduce the lateral displacement due to current. If the wet weight is large in contrast, a buoyant structure may be concentratedly attached between the floating structure and the CWP in order to counter the dead weight of CWP.

In this chapter, the characteristic of an OTEC floating plant with all components as a coupled system is discussed. Additionally, in order to comprehend the response more essentially, the coupled behavior is simplified into a plane motion. As shown later, the two-dimensional assumption is sufficiently accurate to identify a significant response such as a ship in beam seas.

Fig. 3-1 shows an overview of the coupled system with several coordinate systems, and the symbols are explained in Table Table 3-1. The physical model is configured as a moored floating body and an elastic pipe which is attached at an arbitrary position with rotational spring k_r and damper b_r. The point mass m_c is additionally attached at the bottom of the pipe as a clump weight. The global coordinate system *O-YZ* is defined on the mean sea surface. The body-fixed local coordinate system for the floating body is defined with its origin at the center of gravity G-$x_0y_0z_0$.

Mooring lines are attached at an arbitrary position and the elastic pipe is attached at $\begin{bmatrix} y_0 & z_0 \end{bmatrix}^{\mathrm{T}}$ on the same section of the floating body. The position is denoted as *C* and the local coordinate system for the elastic pipe is *C-yz*. Note that the axes *y* and *z* are basically inverse to *Y* and *Z* directions, respectively.

Table 3-1 Parameters for the coupled system.

Parts	Symbols	Meanings
floating body	η, ζ, θ	sway, heave and roll
	$\overline{OG}$	distance of center of gravity from sea surface Note: center of gravity is basically under the surface
	$\mathbf{M}_0$	mass matrix
	$\mathbf{M}_a$	added mass matrix
	$\mathbf{B}_1$	linear damping matrix
	$\mathbf{B}_2$	nonlinear damping vector
	$\mathbf{C}_0$	hydrostatic stiffness matrix
	$\mathbf{F}_0$	hydrodynamic force vector
elastic pipe	ϕ	angle of rigid rotational
	u	axial displacement
	w	lateral displacement
	l	length
	E	Young's modulus
	ρ	material density
	$D_{\mathrm{in}} / D_{\mathrm{out}}$	inner/outer diameter
	A	sectional area
	$A_{\mathrm{in}} / A_{\mathrm{out}}$	inner/outer area
	I	moment of inertia of area
	C_a	added mass coefficient
	C_d	drag coefficient
	m_c	mass of clump weight
mooring system	$\mathbf{R}$	restoring force vector
	$\mathbf{K}$	linearized stiffness matrix
constraint	k_r	rotational stiffness
	b_r	rotational damping
environment	ρ_f	fluid density
	g	gravity acceleration

The coupled system is formulated by the following procedure. First, the moored floating body - elastic pipe is divided into two free bodies. The subsequent three subsections explain the formulation for each body. Second, constraints are made at the joint position between two bodies. At last, the constraints are eliminated for the number of unknowns between two bodies, thus a coupled equation is obtained.

The equation of motion is separated into three stages based on framework of coupled frequency domain analysis with equivalent linearization in Ref. [69] which has been used for risers and mooring design. Static analysis is solved for the equilibrium state considering nonlinearity of mooring force, drag force and finite deformation of the elastic pipe. In the dynamic analysis, the equation of motion is linearized around the static equilibrium position and then solved in frequency-domain: Wave Frequency (WF) domain of 3-30 seconds and for Low Frequency (LF) domain over 50 seconds.

3.2.1 **Floating body**

The floating body is assumed rigid, in which the degrees of freedom are three: $\mathbf{x} = \begin{bmatrix} \eta & \zeta & \theta \end{bmatrix}^{\mathrm{T}}$, that is, we consider only sway, heave and roll motions in the *YZ* plane (or we fix surge, pitch and yaw motions). The equation of motion is represented as,

$$\left(\mathbf{M}_0 + \mathbf{M}_a\right)\ddot{\mathbf{x}} + \mathbf{B}_1\dot{\mathbf{x}} + \mathbf{B}_2\left(\dot{\mathbf{x}}\right) + \mathbf{C}_0\mathbf{x} + \mathbf{R}\left(\mathbf{x}\right) = \mathbf{F}_0 + \boldsymbol{\lambda}. \tag{3.1}$$

Here, $\boldsymbol{\lambda}$ is constraint force vector with top of the elastic pipe, and $\mathbf{F}_0$ is load acting on the body. The current and wind forces are modeled as a drag force. Interaction effect between body and waves is modeled by radiation/diffraction forces, mean drift force and slow-varying drift force. The wave diffraction effect from the elastic pipe can be neglected for >7 seconds of wave period since the applicable elastic pipe is assumed below 15 m of diameter as 100 MW OTEC CWP. Besides, the mooring lines and the elastic pipe could be affected by the radiation/diffraction waves from the floating body. However, these effects are not considered in this simplified formulation, since the wave forces are considered to be small in comparison to the structural interactions. In addition, nonlinear damping due to viscosity is modelled as a quadratic damping: $\mathbf{B}_2\left(\dot{\mathbf{x}}\right) = \begin{bmatrix} B_{2,1}\dot{\eta}\left|\dot{\eta}\right| & B_{2,2}\dot{\zeta}\left|\dot{\zeta}\right| & B_{2,3}\dot{\theta}\left|\dot{\theta}\right| \end{bmatrix}^{\mathrm{T}}$.

3.2.2 **Mooring system**

The more accurate analysis for the middle to final design stages should consider the dynamic tension, hydrodynamic forces and geometric nonlinearity of mooring lines. It is well known that their contribution would be significant on LF motions and mean displacement of a floating body especially for a deep water mooring [68]. However, a simplified analysis considering only stiffness and damping of the mooring system can be employed in an initial design stage (*e.g.*, [70]). In this formulation, we thus consider the stiffness of the mooring system based on their methodology, and the damping due to the mooring system is assumed as a linear damping ratio for the moored floating body.

A restoring force on a moored floating body is exerted by two characteristics of a mooring line: axial elasticity and deadweight of the mooring line. The restoring force can be determined from the shape of the line between the floating body and the anchor. The stiffness matrix **K** in Table 3-1 can be obtained by a differential coefficient of the restoring force vector **R** at the steady position $\mathbf{x}_{st}$:

$$\mathbf{K} = \left.\frac{\partial \mathbf{R}}{\partial \mathbf{x}}\right|_{\mathbf{x}=\mathbf{x}_{st}} . \tag{3.2}$$

3.2.3 **Elastic pipe**

The equation of motion or equilibrium is derived from the principle of energy. The elastic pipe is assumed as a Bernoulli-Euler beam; besides, the pipe has the rigid motion: the translational motion at the top as $\mathbf{r}_c = \begin{bmatrix} y_c & z_c \end{bmatrix}^{\mathrm{T}}$ and the rotational motion of angle ϕ. In order to consider the initial tension, the axial strain due to bending as the geometric nonlinear effect is also involved. The axial tension resists lateral load and traditionally considered in riser analysis [71]. In summary, the strain and the global position of a point on the neutral axis are described as

$$\varepsilon(y,z,t) = u' + 0.5w'^2 - yw'', \tag{3.3}$$

$$\mathbf{r}(z,t) = \mathbf{r}_c - \begin{bmatrix} \cos\phi & -\sin\phi \\ \sin\phi & \cos\phi \end{bmatrix} \begin{bmatrix} w \\ z+u \end{bmatrix}. \tag{3.4}$$

By using Eqs. (3.3) and (3.4), the kinetic energy K and the potential energy U are given as,

$$K = \int_0^l \frac{1}{2}\rho A\left|\dot{\mathbf{r}}(z)\right|^2 dz + \frac{1}{2}m_c\left|\dot{\mathbf{r}}(l)\right|^2, \tag{3.5}$$

$$U = \int_0^l \int_A \frac{1}{2}E\varepsilon^2 dAdz\,. \tag{3.6}$$

In addition, we have the virtual work of the external forces,

$$\delta W = \int_0^l \mathbf{F}^{\mathrm{T}}\delta\mathbf{r}dz + M\delta(\phi - w')\,. \tag{3.7}$$

Here, the external force **F** and the moment M include hydrodynamic force, gravity, buoyancy, inertia of internal fluid and constraint force with the floating body. The hydrodynamic force acting on normal direction of the pipe is calculated by the modified Morison's formula. Inertia force due to internal fluid is additionally acting on normal direction. Since both top and bottom ends are open, the axial inertia force of the internal fluid is not considered here. The normal force can thus be denoted as,

$$F_n = \frac{1}{2}\rho_f C_d D_{out}(V_n - U_n)|V_n - U_n| - \rho_f C_a A_{\mathrm{out}}\dot{U}_n - \rho A_{\mathrm{in}}\dot{U}_n + \rho(C_a + 1)A_{\mathrm{out}}\dot{V}_n\,, \tag{3.8}$$

where, F_n is the normal hydrodynamic force acting on section of pipe, V_n is the normal fluid velocity of waves and current and U_n is the normal velocity of the pipe itself.

These equations and hydrodynamic forces have a high nonlinearity. In particular if the diameter is large and the wet weight is small, the angle ϕ is to be regarded as finite rotation. Thus, the inclined pipe should be considered in the equation of motion.

Since loads and boundary conditions are complex, we cannot derive an exact solution. Instead of this, the axial and the lateral displacement are represented by the generalized coordinates **a**, **b** and the mode shape functions based on the Galerkin's method:

$$w(z,t) = \mathbf{a}^{\mathrm{T}}(t)\boldsymbol{\psi}(z),\ u(z,t) = \mathbf{b}^{\mathrm{T}}(t)\boldsymbol{\tau}(z)\,. \tag{3.9}$$

Here, power series functions can be used for the mode functions $\boldsymbol{\psi}(z)$, $\boldsymbol{\tau}(z)$ in static analysis. In dynamic analysis, an exact solution of rotational spring – mass beam and fixed – mass column is assumed as mode shape functions (see Appendix A.1). Although Finite Element Method (FEM) [13] can be an alternative candidate of the engineering discretization of CWP, the Galerkin's method has an advantage of more directly describing the interaction between the elastic modes of CWP and the rigid motions of the floating body.

Therefore, the equation of motion or equilibrium is obtained by Euler-Lagrange equation with the kinetic energy K, potential energy U and virtual work δW as,

$$\left[-\frac{\partial U}{\partial \mathbf{p}}\right]^{\mathrm{T}} \delta\mathbf{p} + \delta W = 0 \quad \text{for statics,} \tag{3.10}$$

$$\left[\frac{\partial (K-U)}{\partial \mathbf{p}} - \frac{d}{dt}\frac{\partial (K-U)}{\partial \dot{\mathbf{p}}}\right]^{\mathrm{T}} \delta\mathbf{p} + \delta W = 0 \quad \text{for dynamics,} \tag{3.11}$$

where, $\mathbf{p} = \begin{bmatrix} \mathbf{r}_c^{\mathrm{T}} & \phi & \mathbf{a}^{\mathrm{T}} & \mathbf{b}^{\mathrm{T}} \end{bmatrix}^{\mathrm{T}}$ is the generalized coordinates.

3.2.4 **Constraints**

The joint system between the floating body and the elastic pipe is simplified into a pinned joint, a rotational spring and a damper. The model can reproduce a gimbal, a universal or a flexible joint system that are employed in several preliminary designs. Therefore, two constraints are applied to the floating body and the top of the pipe.

(1) The elastic pipe is connected at an arbitrary position on the floating body,

$$\mathbf{r}_c = \begin{bmatrix} \eta \\ \zeta - \overline{\mathrm{OG}} \end{bmatrix} + \begin{bmatrix} \cos\theta & -\sin\theta \\ \sin\theta & \cos\theta \end{bmatrix} \begin{bmatrix} y_0 \\ z_0 \end{bmatrix}. \tag{3.12}$$

(2) Two bodies are connected with a rotational spring and a damper,

$$M_0 = k_r\left(\phi - \theta - w'\right) + b_r\left(\dot{\phi} - \dot{\theta} - \dot{w}'\right). \tag{3.13}$$

3.2.5 **Equation of equilibrium**

Along with the diameter of the CWP becoming larger, the horizontal displacement of the floating body is significant due to a current acting on the pipe. To consider the nonlinearity of the mooring system and the rotation of the pipe, the steady state should be first calculated. The equation of equilibrium is obtained as,

$$\mathbf{S}(\mathbf{p}) = \left[\mathbf{S}_{\mathbf{x}}^{\mathrm{T}} \quad S_\phi \quad \mathbf{S}_w^{\mathrm{T}} \quad \mathbf{S}_u^{\mathrm{T}}\right]^{\mathrm{T}} = \mathbf{0}, \tag{3.14}$$

where,

$$\begin{cases} \mathbf{S}_{\mathbf{x}} = \mathbf{C}_0\mathbf{x} + \mathbf{R} - \mathbf{F}_d - \mathbf{F}_{\mathrm{drift}} - \boldsymbol{\lambda} \\ S_\phi = \int_0^l f\left(z + \mathbf{b}^{\mathrm{T}}\boldsymbol{\tau}\right)dz - \gamma g\int_0^l\left[\left(z + \mathbf{b}^{\mathrm{T}}\boldsymbol{\tau}\right)\sin\phi - \mathbf{a}^{\mathrm{T}}\boldsymbol{\psi}\cos\phi\right]dz \\ \quad -m_c g\left[\left\{l + \mathbf{b}^{\mathrm{T}}\boldsymbol{\tau}(l)\right\}\sin\phi - \mathbf{a}^{\mathrm{T}}\boldsymbol{\psi}(l)\cos\phi\right] - k_r\left[\phi - \theta - \mathbf{a}^{\mathrm{T}}\boldsymbol{\psi}(0)\right] \\ \mathbf{S}_w = \int_0^l\left(-EI\boldsymbol{\psi}\boldsymbol{\psi}''''^{\mathrm{T}} + T'\boldsymbol{\psi}\boldsymbol{\psi}'^{\mathrm{T}} + T\boldsymbol{\psi}\boldsymbol{\psi}''^{\mathrm{T}}\right)\mathbf{a}dz + \int_0^l\left(\gamma g\sin\phi - f\right)\boldsymbol{\psi}dz \\ \quad +\left[\left(EI\boldsymbol{\psi}\boldsymbol{\psi}'''^{\mathrm{T}} - EI\boldsymbol{\psi}'\boldsymbol{\psi}''^{\mathrm{T}} - T\boldsymbol{\psi}\boldsymbol{\psi}'^{\mathrm{T}}\right)\mathbf{a}\right]_0^l + m_c g\sin\phi\boldsymbol{\psi}(l) + k_r\left[\phi\boldsymbol{\psi}'^{\mathrm{T}} - \theta\boldsymbol{\psi}'^{\mathrm{T}} - \boldsymbol{\psi}'\boldsymbol{\psi}'^{\mathrm{T}}\mathbf{a}\right](0) \\ \mathbf{S}_u = \int_0^l T'\boldsymbol{\tau}dz + \left[-T\boldsymbol{\tau}\right]_0^l + \int_0^l \gamma g\cos\phi\boldsymbol{\tau}dz + m_c g\cos\phi\boldsymbol{\tau}(l) \end{cases} \tag{3.15}$$

Here, $\mathbf{p} = \left[\mathbf{x}^{\mathrm{T}} \quad \phi \quad \mathbf{a}^{\mathrm{T}} \quad \mathbf{b}^{\mathrm{T}}\right]^{\mathrm{T}}$ is the generalized coordinate, and the vector that satisfies Eq. (3.14) is the steady state. The vector $\mathbf{S}$ and scalar S on the left side mean the sum of forces in each component of $\mathbf{p}$. $\mathbf{F}_d$ is the drag force due to a wind and current acting on the floating body, $\mathbf{F}_{\mathrm{drift}}$ is the mean drift force due to waves, T is the tension, γ is the wet weight of the pipe and $f(z)$ is the current force acting on the pipe. The constraint force $\boldsymbol{\lambda}$ and those forces are represented by

$$\begin{aligned} \boldsymbol{\lambda} = &\int_0^l f(z)dz\left[\cos\phi \quad \sin\phi \quad y_0\sin(\phi-\theta) - z_0\cos(\phi-\theta)\right]^{\mathrm{T}} \\ &-(\gamma g l + m_c g)\left[0 \quad 1 \quad y_0\cos\theta - z_0\sin\theta\right]^{\mathrm{T}} + k_r\left[0 \quad 0 \quad \phi - \theta - \mathbf{a}^{\mathrm{T}}\boldsymbol{\psi}(0)\right]^{\mathrm{T}} \end{aligned}, \tag{3.16}$$

$$T = EA\left(u' + \frac{1}{2} w'^2 \right), \tag{3.17}$$

$$f\left(z\right) = \frac{1}{2} \rho_f C_d D_{\text{out}} \left(V_c \cos\phi \right) \left| V_c \cos\phi \right|. \tag{3.18}$$

3.2.6 **Equation of motion**

After solving the equilibrium equation above, the equation of motion is linearized for frequency domain analysis. Then, we will obtain a Response Amplitude Operator (RAO) not only for the floating body (sway, heave and roll) but also for the rotation ϕ and the modal amplitudes **a** and **b** of the elastic pipe at WF. The LF response can be predicted by the same procedure. The linearization is carried out by the assumptions below.

(1) Replacing the trigonometric function about the steady rotation angle ϕ to first order Tayler expansion approximation.

$$\sin\phi = s + c\phi, \;\; \cos\phi = c - s\phi, \tag{3.19}$$

where, $s = \sin\phi_{st}$ and $c = \cos\phi_{st}$. In addition, the mooring force is linearized by Eq. (3.2) at the steady position $\mathbf{x}_{\text{st}}$.

(2) The quadratic damping in Eqs. (3.1) and (3.8) is approximated by the equivalent linearization method for both waves and current [69].

The roll damping is,

$$B_{2,3}\dot{\theta}\left|\dot{\theta}\right| = \left(B_{2,3}\sqrt{\frac{8}{\pi}}\sigma_{\dot{\theta}} \right)\dot{\theta}. \tag{3.20}$$

The drag force acting on the pipe is,

$$\left(V_n - U_n\right)\left|V_n - U_n\right| = \left(V_c + V_w - U_n\right)\left|V_c + V_w - U_n\right| \equiv b_1\left(V_w - U_n\right) + b_0, \tag{3.21}$$

where,

$$b_1 = \sqrt{\frac{8}{\pi}}\sigma_u \exp\left[-\frac{1}{2}\left(\frac{V_c}{\sigma_u}\right)^2\right] + 2V_c \operatorname{erf}\left(\frac{1}{\sqrt{2}}\frac{V_c}{\sigma_u}\right), \tag{3.22}$$

$$b_0 = \sqrt{\frac{2}{\pi}}\sigma_u V_c \exp\left[-\frac{1}{2}\left(\frac{V_c}{\sigma_u}\right)^2\right] + \left(\sigma_u{}^2 + V_c{}^2\right)\operatorname{erf}\left(\frac{1}{\sqrt{2}}\frac{V_c}{\sigma_u}\right), \tag{3.23}$$

here, erf(x) is the error function, $\operatorname{erf}(x) = \frac{2}{\sqrt{\pi}}\int_0^x e^{-y^2} dy$.

Where, V_c is the velocity of a current, V_w is unsteady flow due to waves, U_n is the normal velocity of the motion of pipe itself, b_1 and b_0 are the intercept and the slope of the linearized drag force, and σ_θ and σ_u are the standard deviations of the amplitude of roll angular velocity and relative velocity in irregular waves, respectively. The standard deviations can be estimated by a statistical procedure using RAOs and the wave spectrum.

(3) The high order terms are assumed infinitesimal, and the constant terms are neglected.

As the result of formulation and linearization, the equation of motion can be denoted as a general shape as,

$$\mathbf{M}\ddot{\mathbf{p}} + \mathbf{B}\dot{\mathbf{p}} + \mathbf{C}\mathbf{p} = \mathbf{F} . \tag{3.24}$$

Where, **M** is the inertia matrix, **B** is the damping matrix, **C** is the stiffness matrix, **F** is the load vector and **p** are the generalized coordinate. Those matrixes and vectors are configured by a matrix of floating body and the coefficient matrixes **h** which represent the elastic pipe and constraint (see Appendix A.2),

$$\begin{aligned}
\mathbf{M} &= \mathbf{M}_0 + \mathbf{M}_a + \rho A\int_0^l \mathbf{h}_m(z)dz + m_a\int_0^l \mathbf{h}\mathbf{h}^{\mathrm{T}}(z)dz + m_c\mathbf{h}_m(l) \\
\mathbf{B} &= \mathbf{B}_0 + \int_0^l b\mathbf{h}\mathbf{h}^{\mathrm{T}}(z)dz + b_r\mathbf{h}_r(0) \\
\mathbf{C} &= \mathbf{C}_0 + \mathbf{K} + \int_0^l \mathbf{h}_{k1}(z)dz + \left[\mathbf{h}_{k2}(z)\right]_0^l + \gamma g\int_0^l \mathbf{h}_g(z)dz + m_c g\mathbf{h}_g(l) + k_r\mathbf{h}_r(0) \\
\mathbf{F} &= \mathbf{F}_w + \int_0^l q\mathbf{h}(z)dz
\end{aligned} \tag{3.25}$$

where, m_a is sectional added mass, b is damping coefficient, γ is wet weight of the pipe and q is wave force acting on the pipe as shown below. In addition, $\mathbf{F}_w$ is wave exciting force or slowly-varying drift force acting on the floating body and $\mathbf{B}_0$ is sum of linear and linearized quadratic damping matrix.

$$\begin{cases} m_a = \rho_f C_a A_{\text{out}} + \rho_f A_{\text{in}} \\ \gamma = \left(\rho - \rho_f\right)\left(A_{\text{out}} - A_{\text{in}}\right) \\ b(z) = \dfrac{1}{2}\rho_f C_d D_{\text{out}} b_1 \\ q(z) = b\left(cu_w + sv_w\right) + \rho_f \left(C_a + 1\right) A_{\text{out}} \left(c\dot{u}_w + s\dot{v}_w\right) \end{cases} \tag{3.26}$$

Here, u_w and v_w are the horizontal and vertical velocities of wave particles, respectively, which can be calculated by the velocity potential of a regular wave.

3. 3 **Validation Case**

The analysis case for validation is almost same as the one described in the previous chapter. This section reiterates the outline and describes the changes.

The hull geometry is assumed as the KVLCC2M. A diffraction / radiation analysis is carried out by the HOBEM to compute the first order wave force and the mean drift force. The slowly-varying drift force is calculated by using Newman's approximation with the mean drift force. The roll damping due to eddy and bilge keel is predicted by Ikeda's method as quadratic damping force. And the critical damping ratio for LF sway of the moored ship without CWP is assumed as $B_{11}/2\sqrt{M_{11}C_{11}} = 0.1$.

The analysis is performed for an extreme environment. The ship is moored heading to the most significant incident wave direction; thus, the wave height in beam seas is assumed as half of the head seas. Moreover, the plantship is moored in 1,000 m of water by using twelve mooring lines. This chapter uses the design of the taut mooring system using polyester rope.

The CWP requires 800 m length and 12 m inner diameter in order to intake 235 m^3/s seawater. The material and the structure are 190 mm thickness of the solid wall pipe made as FRP. The mechanical properties of FRP are Young's modulus of 13,776 MPa and density of 1.52 t/m^3 from Ref. [32]. The joint between the CWP and the ship has rotational stiffness of 40 MNm/deg. The

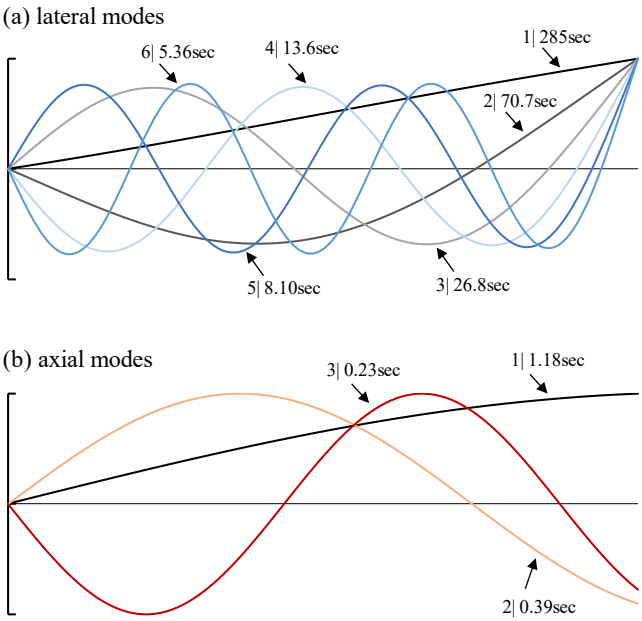

Fig. 3-2 Mode shape and natural period of the CWP.

joint is on the bottom of the ship below the center of gravity. A 1,000 ton clump weight (0.5% of CWP virtual mass) is additionally attached at the bottom of the CWP. The hydrodynamic coefficients for a slender member are tentatively estimated: the drag coefficient $C_d = 0.8$ and the added mass coefficient $C_a = 1.0$. Fig. 3-2 shows the mode shapes and the natural periods of the top supported pipe from mode 1 to mode 5.

3. 4 **Results and Comparisons**

This section presents the results of application of the present formulae to compute the coupled responses for ULS of the study case configured in the previous section. Besides, the applicability for a practical design and limitation of the present model are discussed by comparison with a numerical simulation code.

The results using the present formula with OrcaFlex which is commonly used for a design of offshore structures are compared. OrcaFlex can analyze a coupled system with floating body, mooring lines and riser in the time domain as shown in the previous chapter. To compare the frequency-domain analysis, the response spectra are recovered from the time histories after completing the dynamic analysis.

The procedure of estimating the response spectra and maximum values based on statistical procedure by using the present formula is shown in Fig. 3-3. Here, the degrees of freedom in

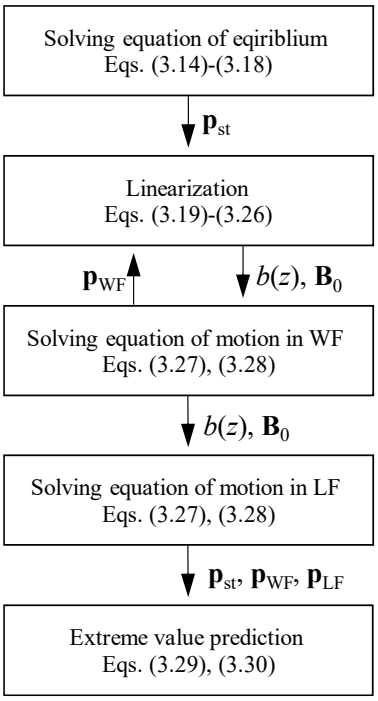

Fig. 3-3 Procedure if the extreme responses using the present coupled model.

Eq. (3.9) are assumed as 7 and 3 for the lateral and the axial modes, respectively. Firstly, we solve equilibrium Eq. (3.14).

Secondly, the WF Response Amplitude Operator (RAO) $\mathbf{p}_{WF}$ and the LF response amplitude function $\mathbf{p}_{LF}$ are calculated by solving Eq. (3.24). In this procedure, the linearized damping coefficient can also be employed to LF domain since the displacement velocity of the LF components is sufficiently small. The response spectra $\mathbf{S}_{WF}$ and $\mathbf{S}_{LF}$ are calculated by,

$$\mathbf{p}_{WF} = \left(\mathbf{C} - \omega^2\mathbf{M} + j\omega\mathbf{B}\right)^{-1}\mathbf{F},\ \mathbf{p}_{LF} = \left(\mathbf{C} - \omega^2\mathbf{M} + j\omega\mathbf{B}\right)^{-1}\mathbf{I}, \tag{3.27}$$

$$\mathbf{S}_{WF} = \left|\mathbf{p}_{WF}\right|^2 S_{xx},\ \mathbf{S}_{LF} = \mathbf{p}_{LF}{}^{*}\mathbf{S}_d\mathbf{p}_{LF}{}^{T}. \tag{3.28}$$

Here, ω is the forced angular frequency, j is the imaginary unit, $\mathbf{I}$ is the unit matrix, S_{xx} is wave spectrum and $\mathbf{S}_d$ is slowly-varying drift force spectra predicted by Newman's approximation and mean drift forces acting to sway. The asterisk * means complex conjugate.

Thirdly, the probability distribution function is assumed as Rayleigh distribution, thus maximum values in three hours and significant values in each domain are calculated by

$$\sigma^2 = \int Sdf,\ X_{\text{sig}} = 2\sigma,\ X_{\max} = \sigma\sqrt{2\ln\left(\frac{10{,}800}{T_z}\right)}, \tag{3.29}$$

where, S is a response spectrum, σ is a standard deviation, X_{sig} is a significant value, $X_{\max}$ is a maximum value, and T_z is a zero-up crossing period which is obtained by the zero and second order moment of the response spectrum.

Finally, the total maximum value is predicted by

$$X_{\max} = X_{\text{st}} + \max\left[X_{\text{WF,max}} + X_{\text{LF,sig}}, X_{\text{WF,sig}} + X_{\text{LF,max}}\right]. \tag{3.30}$$

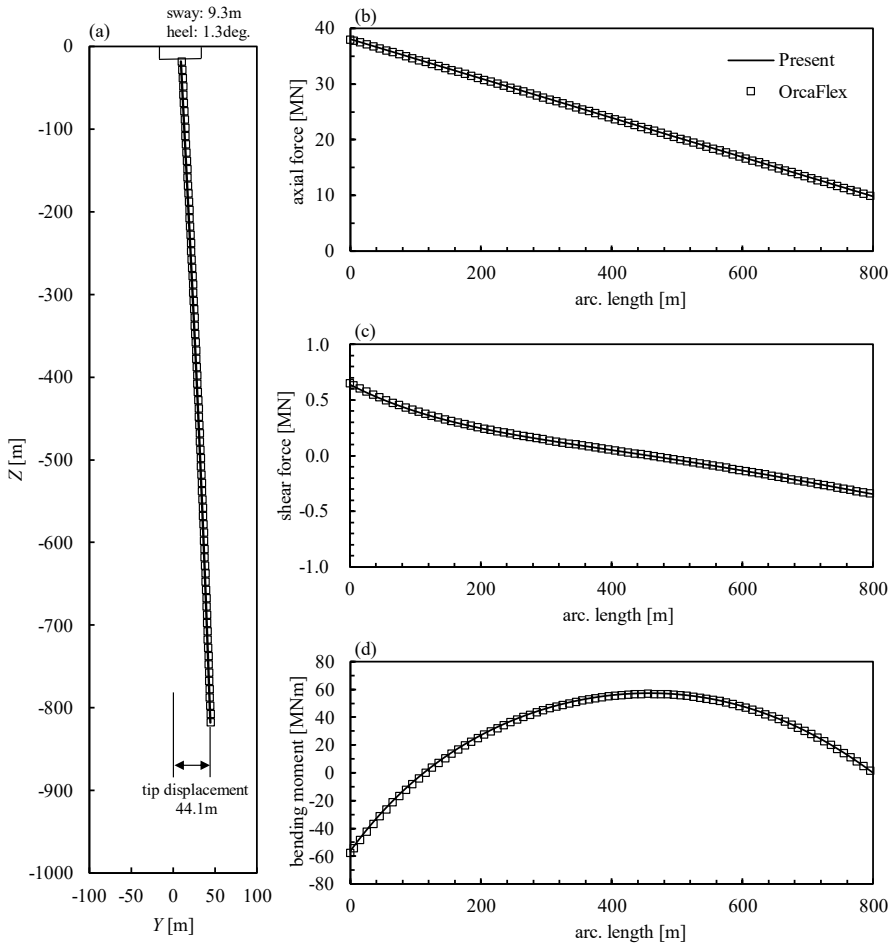

Fig. 3-4 Static deflection of the CWP: (a) global displacement, (b) axial force, (c) shear force and (d) bending moment.

3.4.1 **Results of static analysis**

Selected results of static analysis for both cases are shown in Fig. 3-4. As seen in Fig. 3-4, the internal forces and deflection of the present formulae agree very well with OrcaFlex static analysis. On the other hand, the present formulae do not necessarily correspond to the position of the ship due to neglecting the hydrodynamic forces on the mooring lines, as has already been presented by Ormberg and Larsen [68]. However, the present formulae allow the complete calculation of the elastic deformation of the CWP and the influence of the effect of the attachment to the ship.

Since the projected area of the CWP is larger than that of the hull, current force acting on the CWP is significant for mooring lines. The reaction from the CWP is 36% of the total load in sway direction acting on the hull. By attaching the CWP, therefore, the static tension of the mooring lines becomes 111% on port side and 78% on starboard side of the system without CWP. This point may be important to the configuration of mooring system.

3.4.2 **Results of dynamic analysis**

The results of the ship WF-RAO at the center of gravity are shown in Fig. 3-5. In this figure, the result with and without the CWP are compared as solid and dashed lines, respectively. The result without CWP is obtained by solving Eq. (3.1) excepting the constraint forces. The peak period without the CWP is 11.5 seconds for heave and 12.0 seconds for roll, which are shown as the peaks of dashed lines. As comparison of the lines, it is observed that there is high interaction between sway and roll. Furthermore, results of the modal WF-RAO and actual deflection of the CWP are presented in Fig. 3-7 and Fig. 3-6. The modal amplitude a_i and b_i (the suffix i is the mode number which equals to the number of nodes) in Fig. 3-7 and Fig. 3-6 correspond to the amplitude per unit amplitude regular waves of the assumed lateral and axial mode shapes as shown in Fig. 3-2.

Prior to compare with OrcaFlex, the interaction between the ship and the CWP is discussed. As

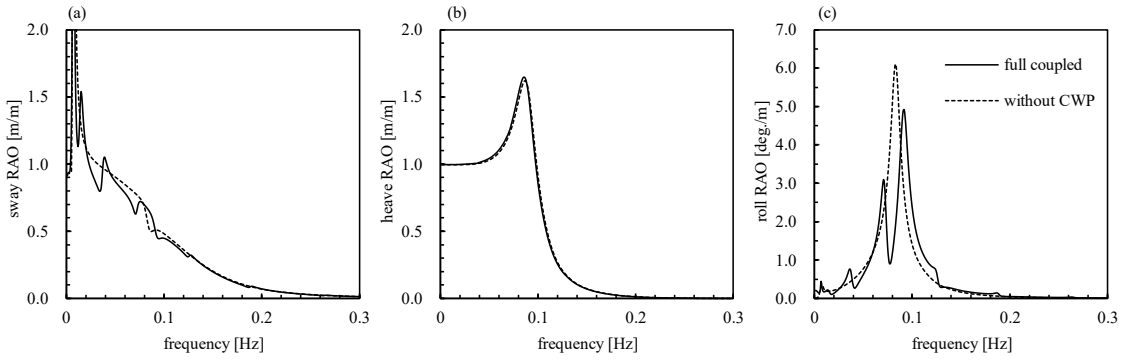

Fig. 3-5 RAO of the ship: (a) sway, (b) heave and (c) roll.

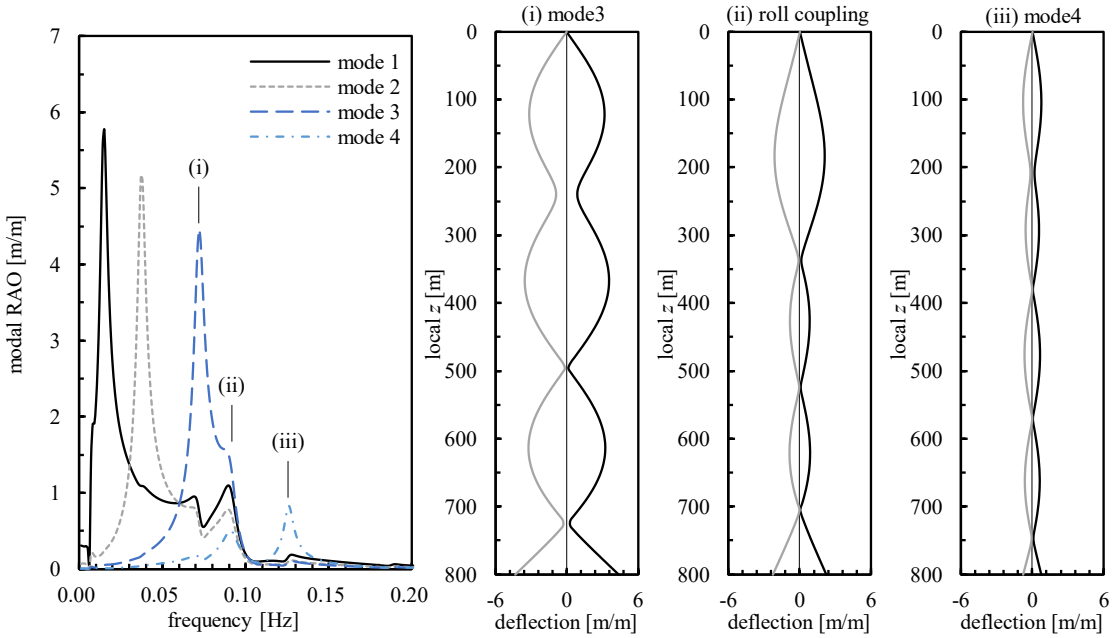

Fig. 3-7 Modal RAO and their shapes of lateral deflection.

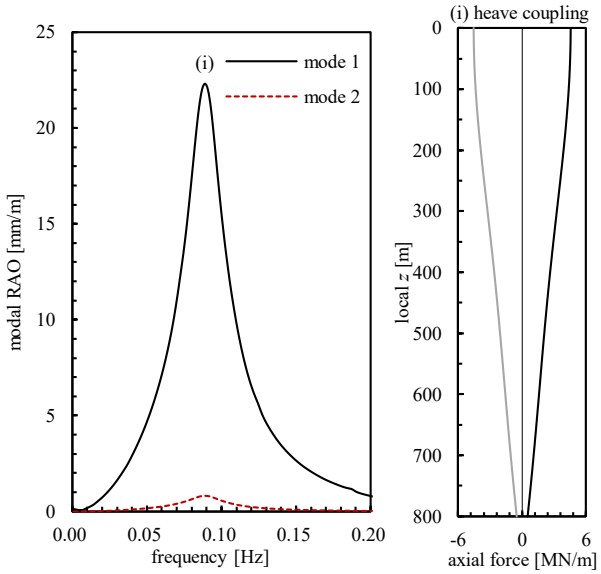

Fig. 3-6 Modal RAO and its shape of axial elongation.

comparison of Fig. 3-5 and Fig. 3-7, it is found that sway and lower order modes of the lateral vibration, and roll and third mode are strongly coupled, respectively. The lower order modes are excited by wave particle motion and sway of the ship which is almost the same amplitude as the wave amplitude. Among the coupling effects, the third mode particularly distorts the response curve of roll. At the peak frequency of roll without CWP, the CWP reduces the amplitude to 31%. The peak frequency shifts to high due to the rotational spring at the joint between the ship and the CWP. On the other hand, as comparison of Fig. 3-5 and Fig. 3-6, it is found that the relationship

between heave and axial vibration of the CWP is considered one-way from the ship. Since natural periods of the axial modes are much shorter than the wave periods, the dynamic tension is excited only around the peak period of heave.

Eq. (3.25) shows that the interaction between the ship and the CWP is a dynamic coupling. Although the dry mass ratio of the CWP to the ship is 4%, the modal mass including the internal fluid and added mass is 16-24% for the sway. The off-diagonal components representing the interaction of the mass matrix are also remarkable. For the sway/roll, the off-diagonal component of the first mode is 8-12% of the inertia term of the ship and it decreases as the number of mode increases. Therefore, the strong coupling described in Fig. 3-5 and Fig. 3-7 is justified by the relatively large mass ratio.

The Power Spectrum Densities (PSD) of the ship responses obtained by both the present procedure and OrcaFlex are presented in Fig. 3-8. As same as the RAOs in Fig. 3-5, the dashed lines mean the responses without CWP. Both analyses are basically in good agreement and these results are clearly different from the sway and roll without CWP. Focusing on the low frequency drift motion in sway, it is found that the peak due to mooring system is reduced by attaching the CWP. Although the CWP increases the coupled virtual mass to 150% of the ship, the drag force

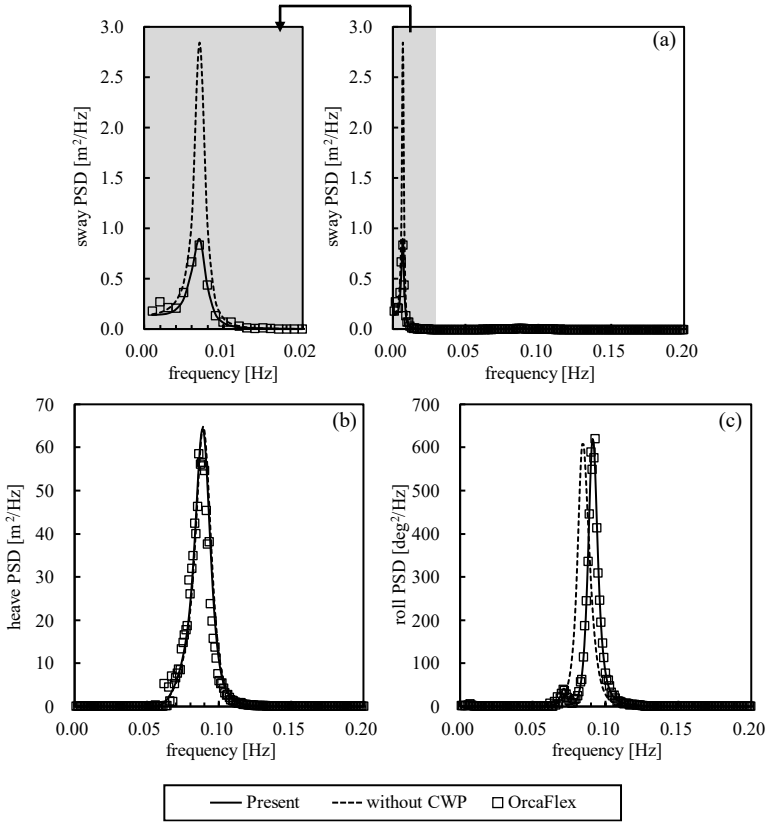

Fig. 3-8 PSD of the ship responses: (a) sway, (b) heave, and (c) roll.

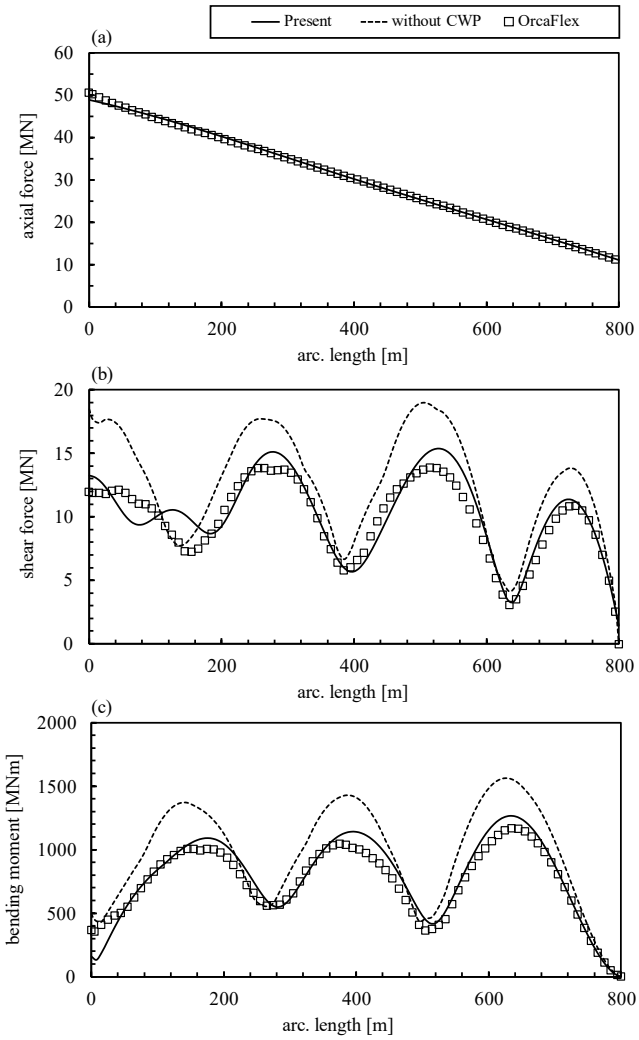

Fig. 3-9 Envelop of the maximum responses of the CWP for 3 hours: (a) axial force, (b) shear force and (c) bending moment.

acting on the CWP is sufficiently large to increase the damping ratio.

Fig. 3-9 presents the envelops obtained by the predicted maximum loads with Eq. (3.30) and maximum loads through the time domain analysis. Note that dashed lines show the result of decoupled analysis with OrcaFlex: simulating the individual behavior of CWP under the forced oscillation using the previously analyzed time histories of the ship without CWP. Almost the same results of axial force are obtained by both present method and OrcaFlex as shown in Fig. 3-9 (a). Comparing this graph with Fig. 3-4 (b), it is observed that the dynamic part of tension is in the range of 28% of the static tension. In Fig. 3-9, the shear force and the bending moment are also in good agreement for most length. Moreover, comparing dashed lines and solid lines, the decoupled analysis evaluates 140% of the coupled analysis as we can see from the difference in the response characteristics. As focusing on the bending moment in Fig. 3-9 (c), the percentages

of individual results: the static, WF and LF stages in Eq. (3.30) are 4.6, 88.5 and 6.9%, respectively. In the LF, the low modes are excited with large amplitude; however, the response is smaller than the WF due to the long period and smaller curvature.

As the results of this section, the present procedure has predicted the coupled responses of floating body and the CWP with practically sufficient accuracy for early design stage. In addition, the formulae can yield a sufficient information on the identification of coupled responses. In this analysis case, there are confirmed strong dynamic coupling due to the large mass ratio in the WF, and the large hydrodynamic force acting on the CWP in the LF and statics as interaction between the ship and the CWP. Both effects are considered a level that could not be ignored in the design. On the other hand, different results are obtained at the neighborhood of the ship in Fig. 3-9. Subsequent detailed design stage will require a time domain analysis which can consider the nonlinearity of the elastic pipe, the 3D motions and detailed effect of mooring system.

In addition, the computational cost of the coupled analysis in this section required such that: the elapsed time of the present procedure implemented in Python was 5.8 seconds and that by OrcaFlex was 1,270 seconds, on a latest laptop PC with Intel Core i7 CPU. This means that the present model can deal with a larger number of design cases in the preliminary design stage. As an alternative to specify the design cases, the present model can clarify the influence of changing global design parameters in the design space.

3. 5 **Characteristic of Coupled Responses**

In this section, the influence of the variation of design parameters on the coupled responses is presented as a preliminary design method or parametric study using present model. The study case is the same as in the previous sections; however, we focus on the CWP and the joint system as design parameters. Here, the inner diameter D_{in} = 12.0 m and the length L = 800 m should be preferentially decided based on the planned capacity of power generation. Therefore, we exclusively address the other parameters: the linear density, bending rigidity, joint system and clump weight.

3.5.1 **Parametric study of static displacement**

This section firstly discusses the influence of the variation of parameters to the static displacement of CWP due to current. In this section, the fixed parameters are $EI = 1.9\times10^9$ kNm^2 and D_{out} = 12.38 m. Fig. 3-11 shows the relationship of the specific gravity ρ / ρ_f versus the top angle ϕ with the variation of the ratio of clump weight to total wet weight $\mu_g = m_c g$ / $\gamma g l$. A

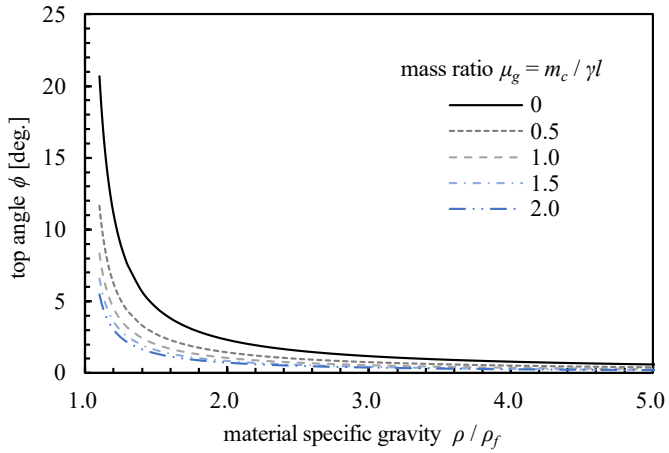

Fig. 3-11 Static top angle versus a specific gravity with variable of the ratio of clump weight to wet weight.

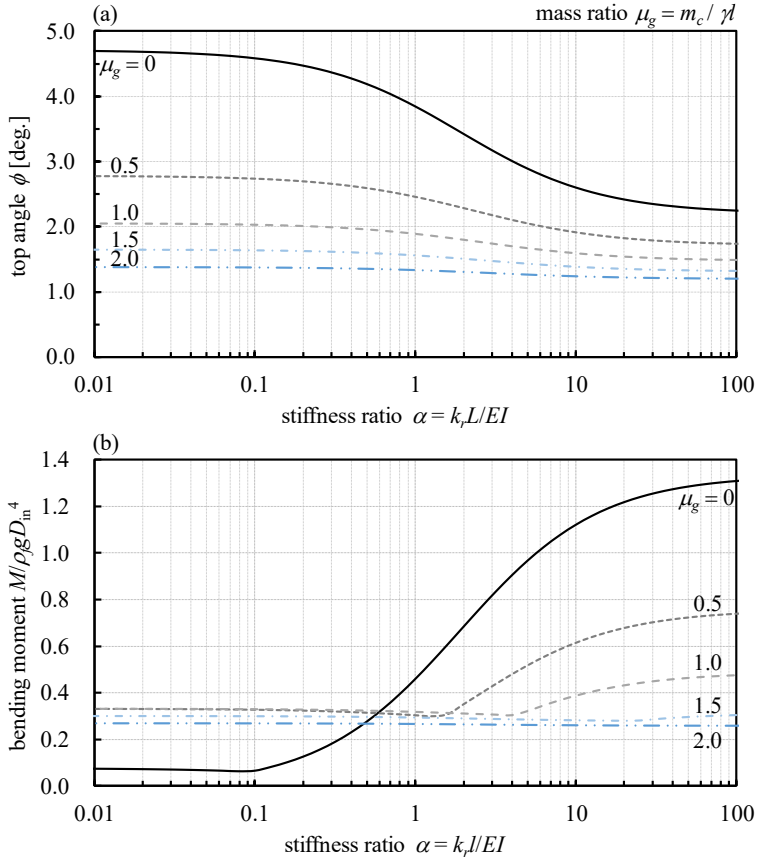

Fig. 3-10 Static states with variable of the top stiffness and the mass of clump weight: (a)static top angle and (b)maximum static bending moment.

lightweight pipe might be preferred for suspending CWP from the floating structure; however, the static displacement due to current increases along with reducing the weight.

The static displacement due to current can be reduced with a top rotational spring and a clump

weight at the bottom. Fig. 3-10 shows the influence of a top rotational stiffness $\alpha = k_r l / EI$ and the clump weight μ_g at ρ/ρ_f = 1.5. In Fig. 3-10 (a), it is observed that the displacement can be reduced by both of the boundary conditions, but the sensitivity of clump weight is higher than the flexible joint. Additionally, the clump weight can reduce the bending moment for $\alpha > 0.5$ as shown in Fig. 3-10 (b).

3.5.2 **Parametric study of dynamic responses**

In Fig. 3-5 and Fig. 3-7 for example, the roll peak is located between the third and the fourth mode of the CWP. The wave peak period T_p is at 11.1 seconds and at the neighborhood of the roll peak. We focus on such a relationship between the roll peak and the location of CWP modes in the frequency axis and the resulting response variation, in order to discuss the general response characteristics. Therefore, a parametric analysis about the bending rigidity and the linear density is performed by using the present model for the WF domain. The bending rigidity EI is normalized as $EI / \rho_f g D_{in}^5$. The range of $EI / \rho_f g D_{in}^5$ is 100-10,000 and the specific gravity ρ / ρ_f is in the range of 1.5-7.0. Note that the parameters related to the hydrodynamic force are fixed so as to focus only on the variation in bending rigidity; D_{out} = 12.38 m, C_d = 0.8 and C_a = 1.0. Moreover, current and wind are also neglected in the static and the dynamic analysis as well.

(1) Effects of bending rigidity and specific gravity

The maximum value of standard deviation for bending moment over the length with changing

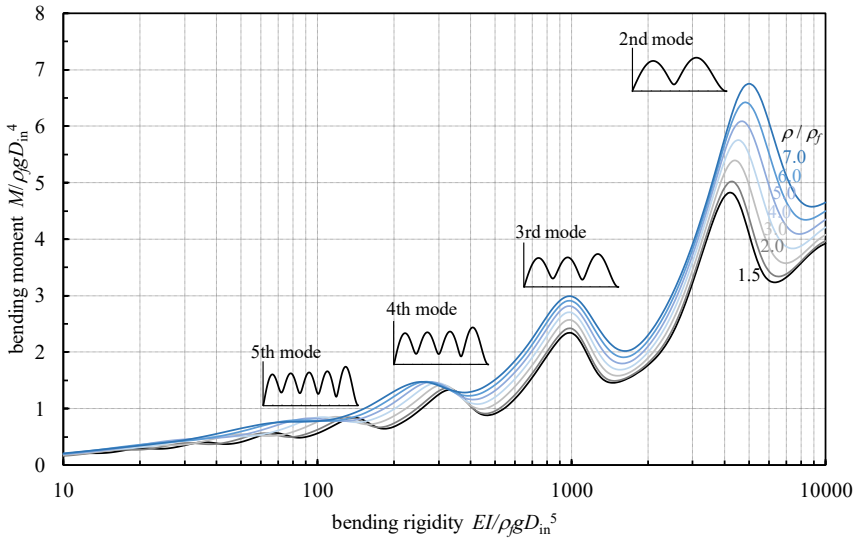

Fig. 3-12 Maximum standard deviation of dynamic bending moment along the length with variable of bending rigidity and specific gravity.

the bending rigidity and the specific gravity is presented in Fig. 3-12. As the bending rigidity increases, the excited mode shifts to lower mode and the curvature decreases. Nevertheless, since only bending rigidity increases while the amplitude does not change significantly, the bending moment ultimately increases.

In addition, the highest natural period (the lowest mode) of CWP in the range of parametric study cannot be shorter than the wave period range; thus, the peaks due to resonance can be found in Fig. 3-12. The wave response characteristics at the local maximum and the minimum points in

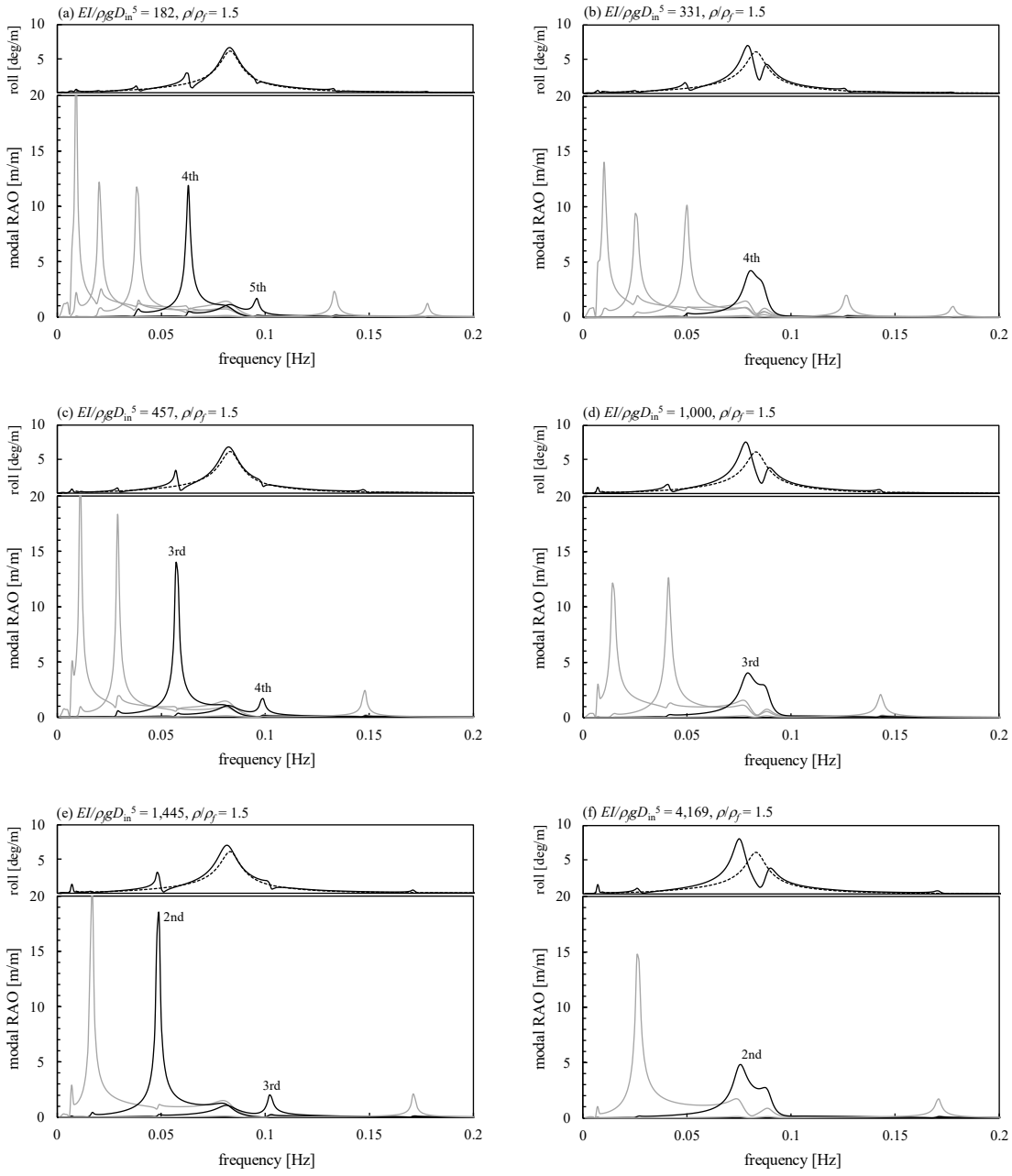

Fig. 3-13 RAO of roll and lateral modes with variable of bending rigidity.

the curve of Fig. 3-12 are extracted and shown in Fig. 3-13. Fig. 3-13 (a), (c) and (e) show the local minimum point, and the roll peak of ship is between the modes of CWP. Fig. 3-13 (b), (d) and (f) show the local maximum point, and the roll peak coincides with either mode of CWP. In the latter case, the shape of roll RAO is significantly distorted, and the amplitude at the peak frequency without CWP is reduced due to the opposite phase between the CWP and roll. It is noted that the amplitude around the peak frequency without CWP can be larger in contrast.

From Fig. 3-12, although the mass of wall of pipe is small compared with the added mass and mass of internal fluid, it is observed that heavier mass clearly decreases the damping ratio in particular at high bending rigidity.

(2) Effects of boundary condition

Subsequently, the effect of the boundary condition of the CWP is focused on. The ratio $\beta = m_c / (\rho Al + m_a l)$ governs the dynamic behavior instead of μ_g for the static displacement. Since $\mu_g / (\rho A + m_a)$ must be limited to small in a practical design, we only discuss the top stiffness here. Fig. 3-14 shows the roll RAO at $EI / \rho_f g D_{in}^5$ and $\rho / \rho_f = 1.5$. The top stiffness not only changes the modal characteristic but also adds the static coupling between ship and CWP. From Fig. 3-14, the rotational stiffness shifts the peak frequency to high and decreases the amplitude as decreasing the ratio of wave exciting force to total of roll stiffness. Fig. 3-15 also shows the standard deviation of bending moment at top and global maximum. At $\alpha < 0.1$, the global maximum occurs at the anti-node point of standing wave of bending. Here, it is observed that the response characteristic hardly changes. As the peak period of roll over $\alpha = 0.1$ approaches the peak period of waves, the response increases and the maximum value transfers to the top at $\alpha > 20$. The top

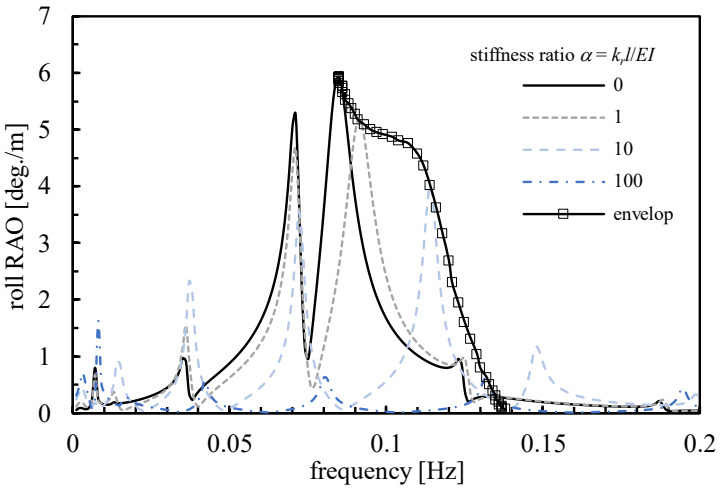

Fig. 3-14 RAO of roll with variable of top stiffness.

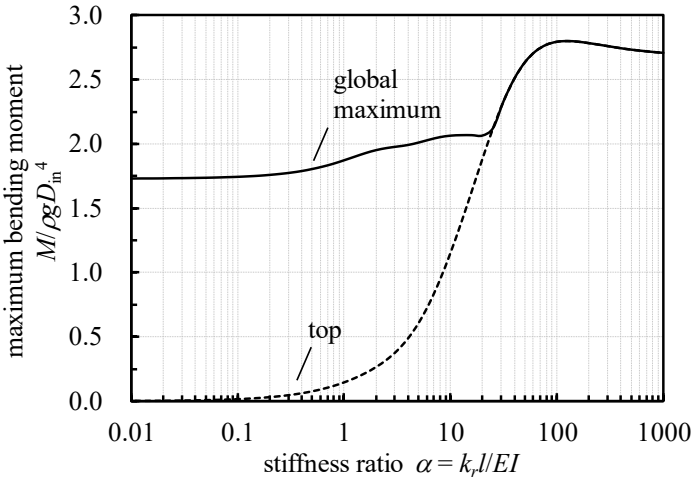

Fig. 3-15 Maximum standard deviation of dynamic bending moment along the length with variable of top stiffness.

bending moment increases until $\alpha = 100$, over that, the bending moment decreases as the response of ship is only sway. However, although the roll cannot be avoided, smaller rotational stiffness or pinned joint is superior in CWP responses as the result.

To conclude this section, a compliant structure with low bending rigidity and small mass is desirable to reduce the bending moment. For the condition that the roll natural period is slightly larger than the wave peak period, a pinned joint is more appropriate than a stiffened joint that shortens the natural period. Additionally, the case that the peak of roll is in between the natural periods of CWP can be expected to reduce the response.

3. 6 **Conclusion**

For the design of floating OTEC plant, a coupled analysis of a floating body, a mooring system and a CWP should be employed due to the huge mass of internal fluid of CWP. This study has constructed a simplified model to easily comprehend the coupled responses, which will be useful in the early stage of design. The model configured a floating body, mooring lines, an elastic beam attached by a rotational spring and a damper and a clump weight at the bottom. The equation of planer motion and equilibrium are derived based on the basic principles of mechanics, and the beam is discretized by Galerkin's method in order to more directly comprehend the relationship between the elastic mode of CWP and the rigid mode of floating body. These formulae are mathematically tractable and could be easily implemented in interfaces with rich mathematical libraries such as Python or Matlab.

The present model has been compared with time domain analysis by using OrcaFlex. In order

for comparison, a 100 MW-NET ship-shaped plant, spread mooring system with 12 taut legs, and GFRP CWP with a length of 800 m and an inner diameter of 12 m is configured as analysis cases. The present equations are solved in frequency domain with equivalent linearization of the drag force and the response spectra, and the extreme values are compared. It is observed that the present model has predicted the coupled response with practically sufficient accuracy for the early design stage. I would like to highlight that the model/method has the advantage of providing the coupled response at the early stage of design, and it can deal with more design cases and sensitivity of design parameters at this time. Meanwhile, in the later design stages, the hydrodynamic forces and nonlinearity of the mooring system, nonlinearity of the CWP and 3D motions need to be addressed.

As a preliminary design method applying present model, the influence of the variation of design parameters to the coupled response characteristic has been discussed through the parametric analysis of bending rigidity, linear density, top rotational stiffness and mass of clump weight. There exists strong interaction between ship and lateral vibration in the case when the roll peak coincides with either mode of CWP. On the other hand, it is difficult to make the natural period of lateral vibration of CWP shorter than the wave period to avoid resonance. A compliant structure with low bending rigidity and small mass will be desirable to reduce the bending moment.

In conclusion of this chapter, the present model could facilitate the preliminary design of an OTEC floating plant and comprehension of the results of numerical simulations and model experiments. To further studies, we intend to focus on the effect of internal fluid and to discuss the variation of coupled characteristic and self-induced vibration problem of CWP.

4 EXPERIMENTAL INVESTIGATION OF A PIPE ASPIRATING FLUID

4. 1 Introduction

An OTEC plant requires intaking a large volume of surface and deep seawater to generate electricity from the temperature gradient of an order of 20℃. A floating plant requires a CWP which has a 12 m diameter and 2-3 m/s velocity to transport 230 m^3/s of deep seawater. The CWP will be hanged off from the platform and the bottom end is free at 800 m depth to intake seawater. Although this pipe is straight and the flow is considered steady, there are concerns about a self-induced vibration due to internal flow [52,53].

Early work by Païdoussis and Luu [72] has theoretically predicted that a self-induced vibration occurs at only 1 m/s for a 1,000 m steel pipe. In addition, according to the results of an application to 100 MW-NET OTEC CWP, it was pointed out that the self-induced vibration may be caused at the velocity of 2-4 m/s [52,53]. The vibration may interfere with the development of OTEC as well as other ocean systems such as Floating LNG Production (FLNG) and ocean mining, and it has led us to investigate this phenomenon. Despite this interest, the issue has not been much discussed, thus it remains unclear even now.

Such a problem of fluid-structure interactions of elastic pipes and internal axial flow has been mainly studied by Païdoussis et al. and systematized in their review papers and literary works [73–75]. In particular, it is widely known that a vertical cantilevered pipe which discharges fluid causes unstable phenomena such as "flutter" and "divergence" over a threshold velocity [73]. On the other hand, the intaking pipe which might be used as an ocean mining and OTEC CWP is a part of the research on "pipes aspirating fluid", and studies have been conducted focusing on their stability (see Section 4.3 in Ref. [75]). The behavior of an aspirating pipe is quite distinct from that of the well-established discharging pipe, and thus it should be considered separately.

The first systematic analysis of aspirating pipe has been undertaken by Païdoussis and Luu [72]. In this theory, when a flow velocity of discharging pipe is replaced by its negative, flutter was found to occur at a very small absolute velocity. Subsequently, Pramila in 1992 [76], Cui and Tani in 1996 [77] and Païdoussis in 1999 [78] have experimentally and/or theoretically contradicted the previous theory, and have individually proposed the revised model considering the inlet flow field. The latest version of the analytical model was constructed by Païdoussis et al. [79] and Giacobbi et al. [80]. Several studies, Axisa [81], Butt et al. [82] and Ma et al. [83], have reported

analyses and experiments using this model. These works considering inlet flow concluded that the flutter could occur at a much larger flow velocity than in the first model.

Since the theory predicts that flutter still exists, an experiment subsequently attempted to prove it. Kuiper and Metrikine [84] and Giacobbi et al. [80] have conducted experiments with different fluids and scales, and have successfully observed the same vibrations that appear to be a flutter. Butt et al. [82] have additionally investigated the modal characteristics of such vibrations by experiment. Moreover, Giacobbi et al. [80] and Adiputra and Utsunomiya [52] have also succeeded to observe the vibration due to internal flow through numerical simulations using Fluid-Structure Interaction (FSI) techniques.

However, there is still ambiguity with regard to justifying the critical velocity and flutter from experimental and numerical results. According to experiment and numerical results [80] vibrations were observed at all flow velocities, in contrast with the theory which predicts it started after a critical velocity. Researchers have provisionally determined flutter from the change in the rate of increase of amplitude with flow velocity [52,80]. Furthermore, the unsteady behavior was observed in which the two phases switched in the experiment, whereas it could not be reproduced by a numerical analysis [80,84].

As far as we know, there has not been definitely comprehended whether these observed phenomena are due to experimental and numerical uncertainties or are reproducible phenomena that can be explained theoretically. This makes us wonder if other experimental and detection methods are possible. In addition, our knowledge of the dynamics of aspirating pipes is based on limited experimental studies. Therefore, the main objective of this chapter and next chapter are to provide experimental data and insight by taking a new look at the dynamics of a submerged pipe aspirating water.

4. 2 **Experiment**

Previous experiments have mainly focused on whether and how aspirating pipes flutter. Kuiper and Metrikine [84], Giacobbi et al. [80] and Butt et al. [82] have observed vibrations that appear to be flutter in previous experiments as far as we know. However, the observed vibrations are of small amplitude, unsteady, and do not exhibit a clear critical flow velocity. In other experiments, flutter has not been observed, or the experiment has been interrupted by the shell-mode collapse of the pipes. Although this approach can provide strong evidence of flutter, its disadvantage is the difficulty of investigating it quantitatively.

As an alternative experimental approach to the observation of flutter and determining a critical flow velocity, Debut et al. [85] have focused on the changes of the modal properties with the

internal flow velocity of an articulated rigid pipe aspirating/discharging water. This approach has provided more quantitative data on the dynamics of the aspirating pipe and the influence of the inlet flow.

This study firstly attempted to observe flutter in a preliminary experiment. Although a very small amplitude long-period vibration at a small flow velocity is measured, it was hardly distinguishable whether it is experimental noise due to the pump and a disturbance of the tank or the effect of internal flow. Therefore, the approach of the first experiment is revised to generate a free vibration and to analyze the effect of the internal flow from the free vibration with the set-up in which possible disturbances is removed. This approach is close to Debut's method which could provide abundant information, even if flutter is not obtained. On that first experiment with a higher accuracy, the behavior at a range of high intaking flow velocity generated by a centrifugal vacuum pump is measured as the second experiment.

With these considerations, both experimental apparatuses were constructed in the deep water tank in RIAM Kyushu University, Japan, which is 65 m long, 5 m wide and 7 m deep. This tank is the largest compared to all previous experiments and has the advantage of eliminating capacity issues and fluid disturbances in the tank. Furthermore, the novelty of this experimental apparatus is to adopt fully submerged condition and has a completely different intake/drainage system from the previous experiments.

Table 4-1 Main properties of the model pipe.

Properties	Values
Length, L	4.000 m
Inner diameter, D_i	0.020 m
Outer diameter, D_o	0.022 m
Thickness, t	0.001 m
Fluid density, ρ	1,000 kg/m^3
Material density	1,204 kg/m^3
Young's modulus, E	2.730×10^9 N/m^2
Poisson ratio, v	0.37

Polycarbonate is used as the material of the model pipe in both experiments. The main properties of the pipe are shown in Table 4-1. The material is modeled as an elastic body, and the material properties in Table 4-1 were obtained directly from specimens taken after the experiment by material testing. The damping properties, hydrodynamic coefficients and boundary conditions of the installed pipe were identified from free vibration tests without internal flow. These results and their validity are detailly discussed in section 4.4.1 below.

As a small scaling model pipe corresponding to the actual CWP is a very flexible tube, there are concerns that the collapse of the section of the pipe due to transmural pressure difference would occur at a small velocity. Since this experiment concentrates on comprehending the dynamic characteristics and verifying the theories, the scale factor between the model pipe and actual CWP is deferred for now.

4.2.1 **First experimental set-up**

In the previous experimental apparatuses, fluid seems to be constantly circulated and supplied to the tank during the measurement due to its capacity. This might cause a disturbance in the measurements; however, there seems to be no mention or discussion of any such effects. The pump may also contain a pulsation and unsteady component which may obscure the vibration of the pipe, as suggested by Kuiper and Metrikine [84].

For the experimental apparatus, this study thus takes great care to avoid mechanical excitation by the pump and disturbance of the fluid. A pump generates a difference in water level between the surge tank and the surrounding water tank, and consequently, this generates a flow in the model pipe. The free surface in the surge tank absorbs the velocity perturbations from the pump, and they are not transmitted to the model pipe. Additionally, the drained fluid from the surge tank is discharged outside the deep water tank to avoid disturbance. Since the capacity of the deep water tank is sufficiently larger than the experimental intake flow rate, it is not necessary to take water level variations into account.

Fig. 4-1 shows the experimental configuration at a cross section of the tank. The surge tank is a circular cylinder with an inner diameter of 0.2 m and a height of 4.0 m, and its top end is open as shown in Fig. 4-1 (b). As shown in Fig. 4-1 (a), the model pipe is fully submerged and transports water to the surge tank. Thus, the top of the model pipe is fixed to the bottom of the surge tank using a threaded joint, and the bottom end is a free inlet. An underwater pump with a DC motor is installed at the bottom of the surge tank, as shown in Fig. 4-1 (a). The output of the pump is controlled changing by the input voltage, and the flow rate is monitored with an impeller type flowmeter close to the discharge end. In this system, the maximum flow velocity is limited by the draft of the surge tank; thus, the maximum internal flow velocity is 1.66 m/s at 60 V input.

The flow rate actually measured is confirmed to be stable. On the other hand, we were unable to quantitatively investigate several possible sources for errors in the experiment. First is the mechanical excitation and local velocity distribution due to the pump just above the entrance from the model pipe to the surge tank. The second is the initial curvature and eccentricity of the model pipe. These experimental uncertainties may cause slight forced vibration.

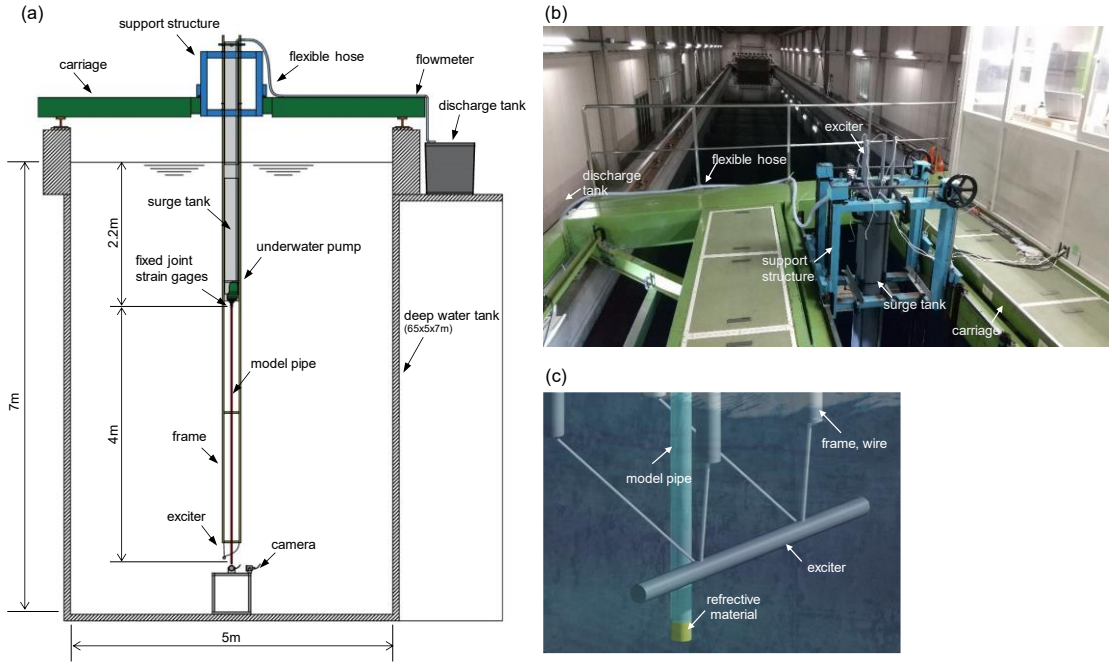

Fig. 4-1 Experimental apparatus: (a) the experimental configuration of a cross-section of the deep water tank, (b) the picture of the view from the carriage, and (c) the bottom of the model pipe.

In order to generate free damped vibration, an exciter instrument is installed around the surge tank to provide an initial displacement to the model pipe. A steel pipe is suspended from the bottom of the frame as shown in Fig. 4-1 (c), and a wire is tied to the steel pipe throughout the frame. By pulling up the wire, the steel pipe horizontally contacts 100 mm above the tip of the model pipe, generating the initial static displacement of the pipe.

In the first step of the experiment, the model pipe is subjected to an initial displacement and internal flow. From this steady state, the transient behavior after releasing the wire was measured in three dimensions with two measurement instruments at the top and bottom of the model pipe. Firstly, dynamic axial strains are measured using four strain gages orthogonally attached near the top end with a sampling frequency of 20 Hz and a resolution of 1.0 μ. Furthermore, a reflective material is attached to the bottom end, and the tip behavior is captured using two digital cameras fixed in specific spatial points. The IPC608UW (obtained from Linovision) which has a maximum resolution of 3850×2160 pixels and a sampling frequency of 20 Hz was used in the experiment.

The analysis of the three dimensional behavior from the camera images was carried out by OpenCV, an open-source image processing library. The camera calibration to eliminate the lens distortion and obtain the focal length is carried out by using Zhang's method [86] implemented in OpenCV. The outline of the reflective material is extracted by image thresholding, and the center of the region surrounded by the outline is recorded as a camera plane coordinate system.

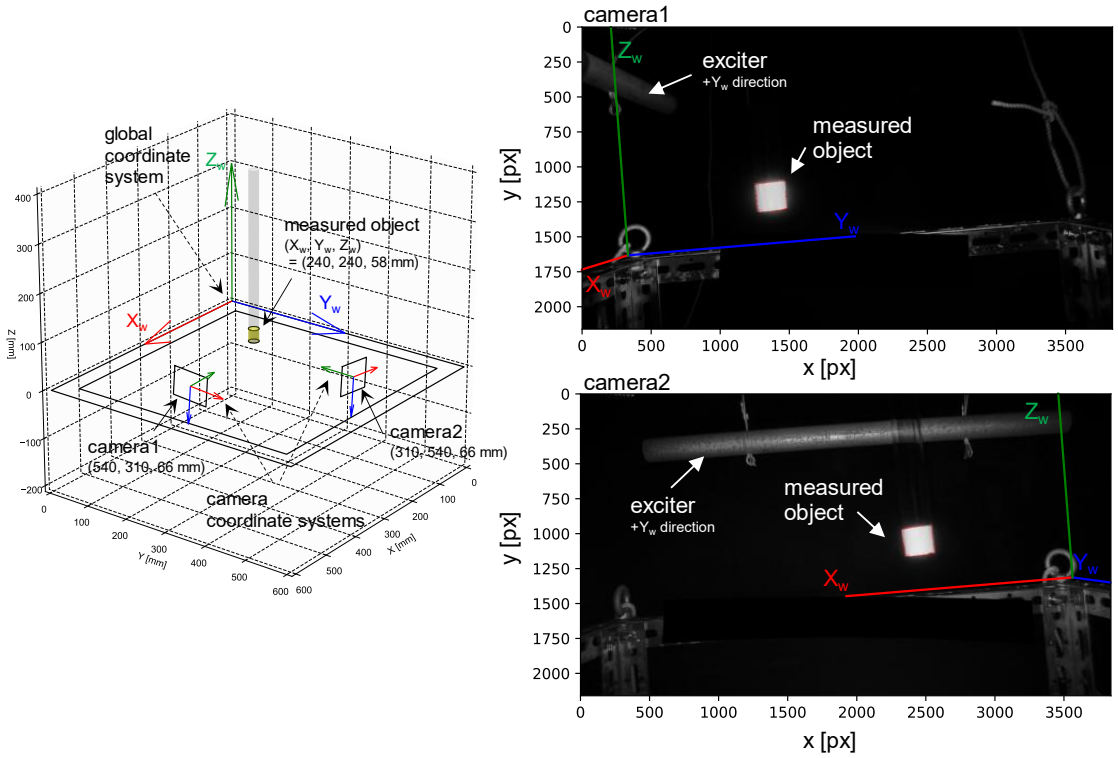

Fig. 4-2 Three-dimensional motion measurement: coordinate systems, the positions of cameras and measured object, and captured views.

Then, the tip behavior in three-dimensional global coordinates is restored by using the least squares method with the two cameras from different viewpoints. Fig. 4-2 shows the images and the positions of cameras, in which the white region is the reflective material. At a distance between the camera and the measurement target of around 200 mm, the resolution of this measurement is 1/40 mm.

4.2.2 **Second experimental set-up**

With the first experiment, the maximum flow velocity is limited by the draft of the surge tank; thus, the maximum internal flow velocity is 1.66 m/s. The aim of this second experiment is to confirm whether self-induced vibration occurs at higher velocity range.

The experimental apparatus is shown in Fig. 4-3. The model pipe is directly connected with a centrifugal vacuum pump through the PVC pipe with 20 mm in inner diameter and 26 mm in outer diameter with three elbows as shown in Fig. 4-3 (b). The centrifugal pump which has the capacity of 95 L/min and 11.5 m in lifting head is installed above the tank. The negative pressure of the impeller inside the pump generates an intake flow that can suck up to 1.3 m of water. The drained fluid from the pump is discharged outside the deep water tank to avoid disturbance. The

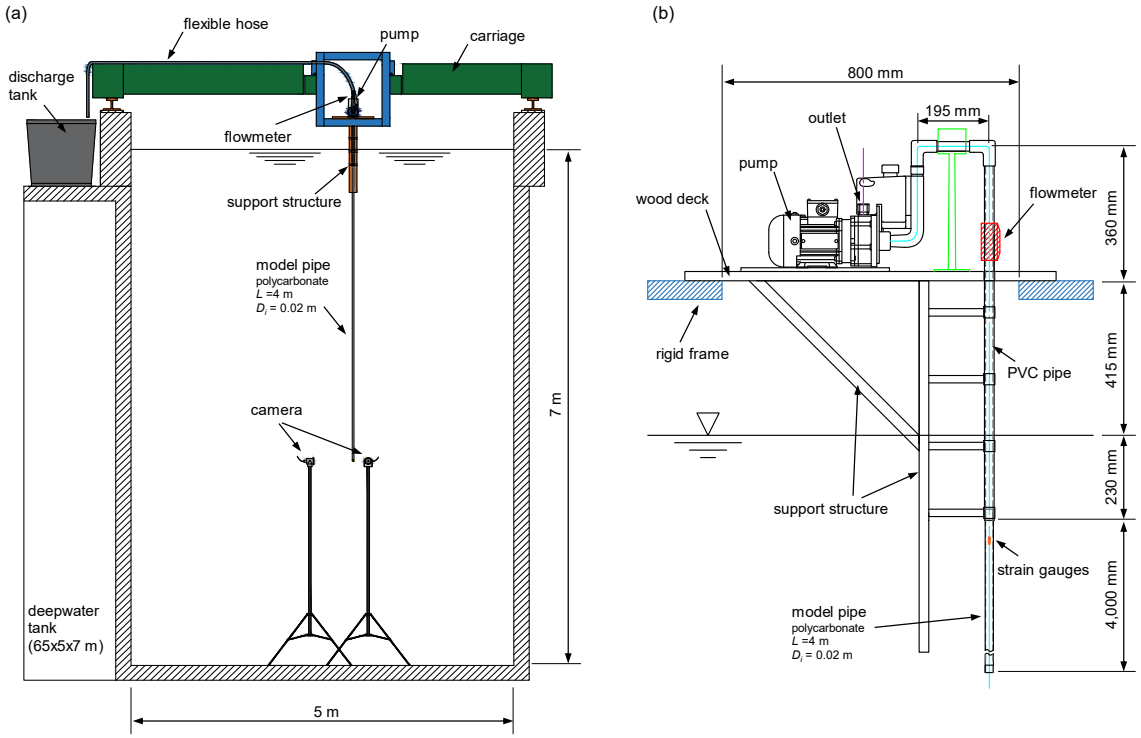

Fig. 4-3 Second experimental apparatus: (a) the experimental configuration of a cross-section of the deep water tank, and (b) the diagram of the intake piping system.

maximum flow velocity of the model pipe is 4.0 m/s during the experiment, it would not be necessary to take a disturbance into account.

As same as the first experimental configuration, there are three measurement instruments: the cameras close to the bottom, the strain gauges at the top of model pipe and the flowmeter at the downstream of the model pipe. A three-dimensional tip behavior in the sampling frequency of 20 Hz is restored by using two cameras. Simultaneously, the dynamic axial strains are measured using four strain gauges orthogonally attached near the top end with the sampling frequency of 1,000 Hz and the resolution of 0.001 μ. Furthermore, the flow rate is obtained from an ultrasonic flowmeter with the sampling frequency of 1,000 Hz and the resolution of 0.1 L/min.

During the experiment, a behavior of the model pipe during a series of start-up, steady state and stop of the pump is measured. The transient time of the start-up and stop is 5 seconds. The output of the pump is controlled by changing the input frequency at the voltage of 60 V.

4. 3 **Experimental Observations**

(1) The first experiment

The free damped signals for intake flow velocity of 0, 0.66, 1.10 and 1.66 m/s are shown in

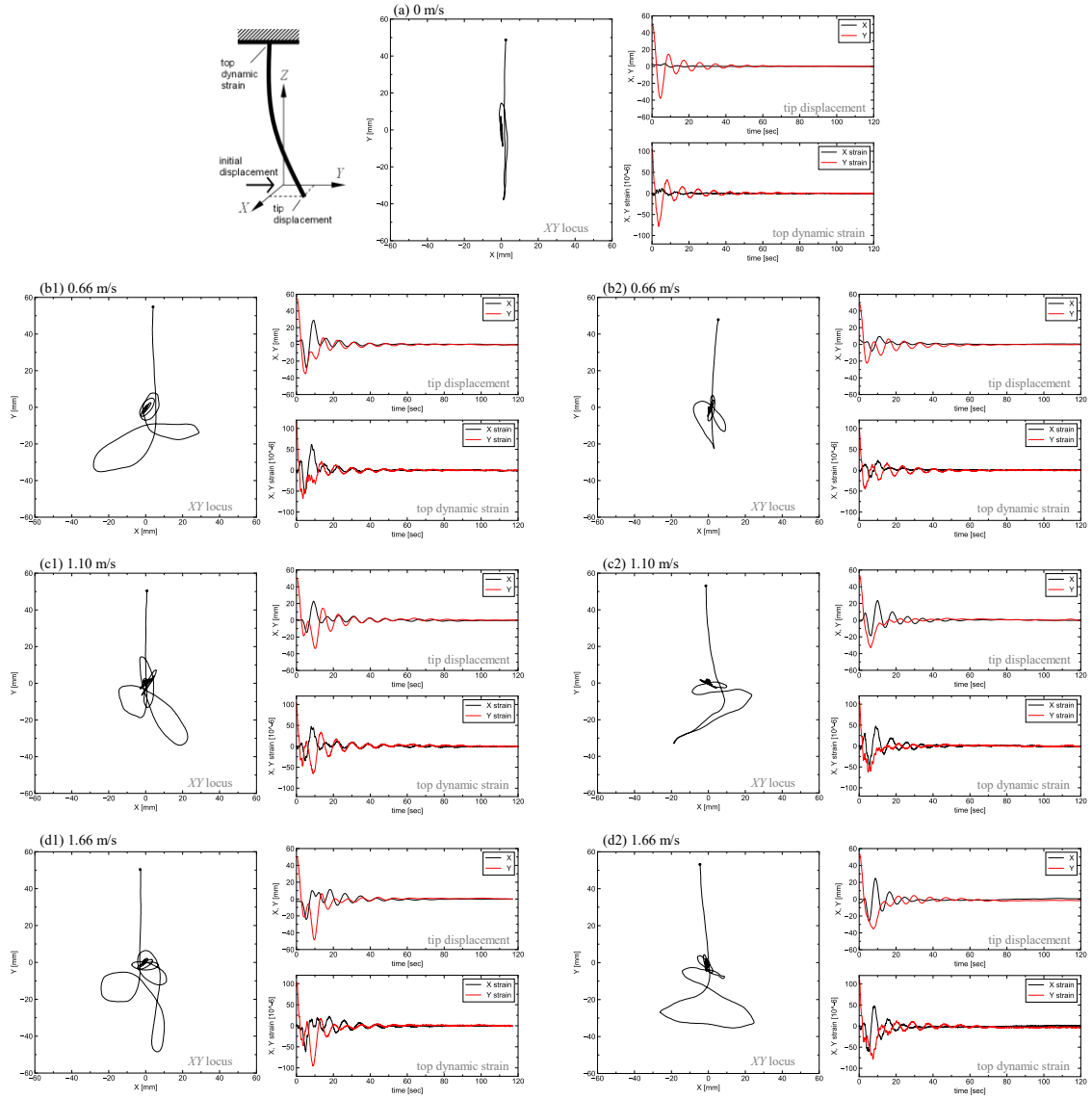

Fig. 4-4 Measured tip behavior and top strain; left graphs are planar locus of bottom part, upper right graphs are displacement time series of bottom part and lower right graphs are strain time-series of top part of the model pipe for initial displacement = 50 mm.

Fig. 4-4 for the initial displacement of $2.5D_i$ (D_i is the inner diameter of the model pipe) in the positive direction of the *Y*-axis.

As shown in Fig. 4-4 (a), the vibration without internal flow is a typical free damped vibration in the *YZ* plane, and there is no excitation force in the perpendicular direction. The higher modes above 1.0 seconds of natural periods are instantly damped, and only the first mode remains as the free damped signal.

In Fig. 4-4 (b-d), the signals with the internal flow are essentially three dimensional, thus an excitation force is acting in the perpendicular direction to the initial displacement. In Fig. 4-4,

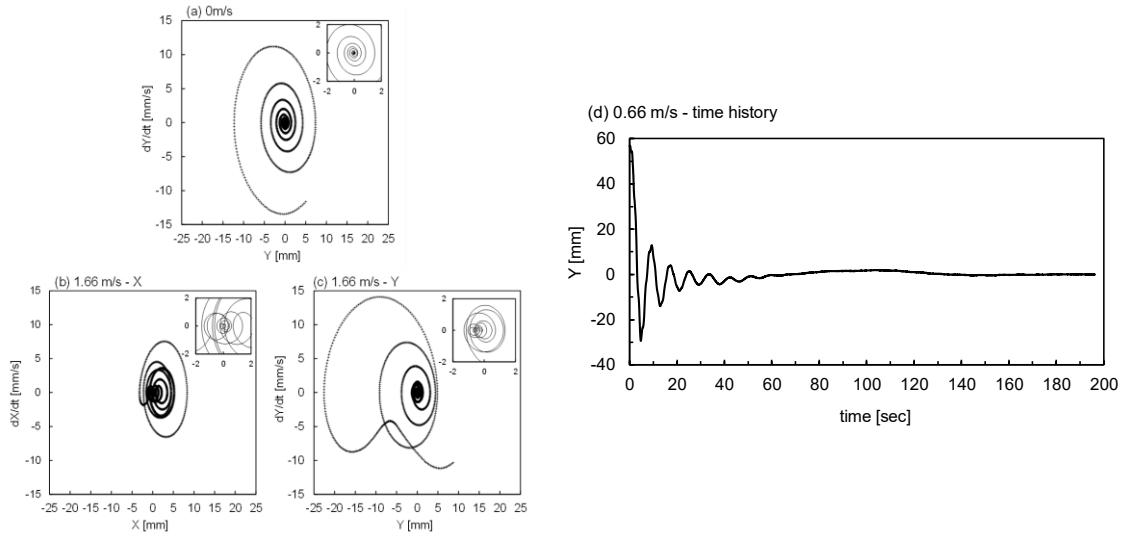

Fig. 4-5 Experimental observations: (a)-(c) phase plane plots at 0 m/s and 1.66 m/s for initial displacement = 10 mm, and (d) typical long period vibration from measured tip displacement of 0.66 m/s.

signals with internal flow go straight up to about Y = -20 mm, then they turn in the negative direction of the X-axis, and free damped vibration occurs with amplitude not much different from the Y-axis. In addition, the characteristic of the vibrations is essentially nonlinear. In particular, comparing Fig. 4-4 (x1) and (x2), the motions show different aspects despite the same flow velocity and the same initial displacement. Thus, this suggests the chaotic character.

Fig. 4-5 (a) shows the results of phase plane analysis of the signals. The behavior on the phase plane without internal flow is a vortex that converges to a stable node. In the behavior with the internal flow, although it eventually converges to the origin, the center point of the vortex appears to be moving. Besides, there are a few cases of long period vibration above 100 seconds as shown in Fig. 4-5 (d). It is suggested that the internal flow may exert a “slowly-varying force".

Unfortunately, we are unable to provide a quantitative investigation, because the behavior is more complex than we initially anticipated. However, previous experiments [80,84] have also suggested a nonlinear three-dimensional behavior, which may relate to the observations in our experiment. An investigation of the theory of nonlinear spatial motion would lead to establishing this phenomenon.

On the other hand, evaluating stability with linear theory is a powerful methodology to evaluate the dynamics of aspirating pipe. All the motion with internal flow converges to a stable node, and flutter was not observed at a maximum flowrate of 1.66 m/s. These results may be highly reliable due to adopting the surge tank and devising the measurement system utilized.

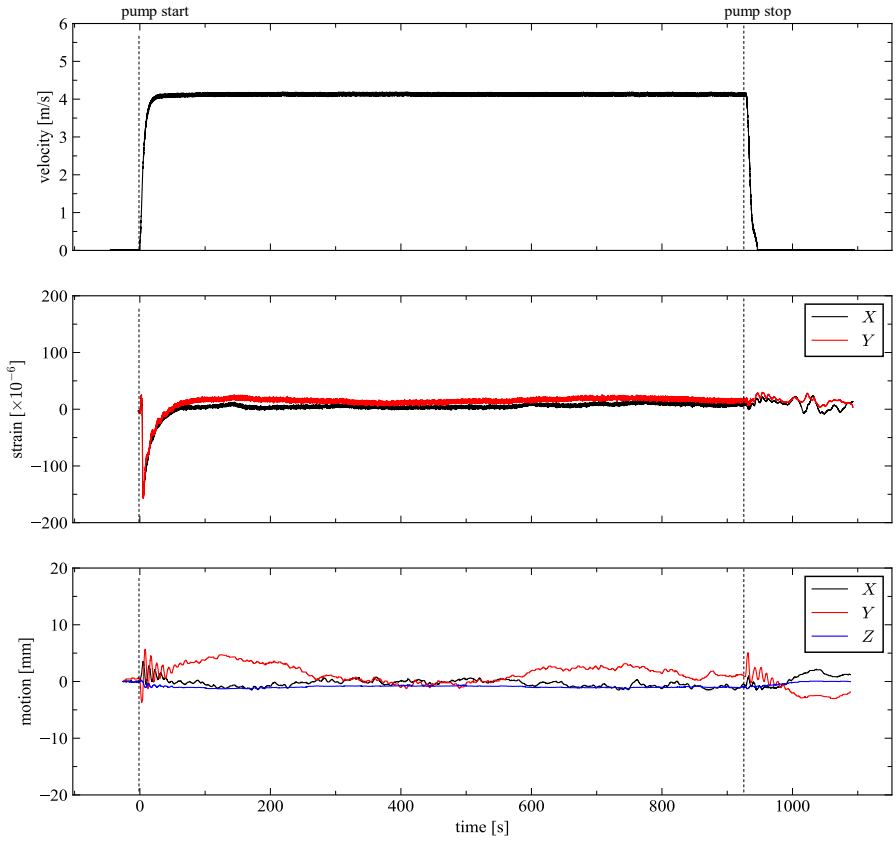

Fig. 4-6 Time series of the second experiment at the flow velocity of 4.1 m/s.

(2) The second experiment

Fig. 4-6 shows an example of the time series of experimental measurement at the flow velocity of 4.1 m/s. First, the internal flow generated by the pump has a velocity variation of the standard deviation of 0.02 m/s. The velocity variation occurs at high frequency range above 20 Hz; thus, it would be hard to affect on the lower-order modes of the model pipe. After the pump starts and stops, transient vibration due to the sudden change in the internal flow momentum is observed. The period after 150 seconds when the vibrations have settled down is considered the steady state and is the subject of this section.

As shown in Fig. 4-6, although the top strain shows slight variation and high frequency vibration that could be mechanical noise caused by the pump, the measured vibration at least the first and second modes is likely to steady. On the other hand, there measures a long-period vibration (the period of about 550 seconds) as shown in Fig. 4-6, which reminds Fig. 4-5 (d). Importantly, this experiment has not reproduced the unsteady behavior in which the amplitude is over the pipe diameter observed in previous experiments [80,84].

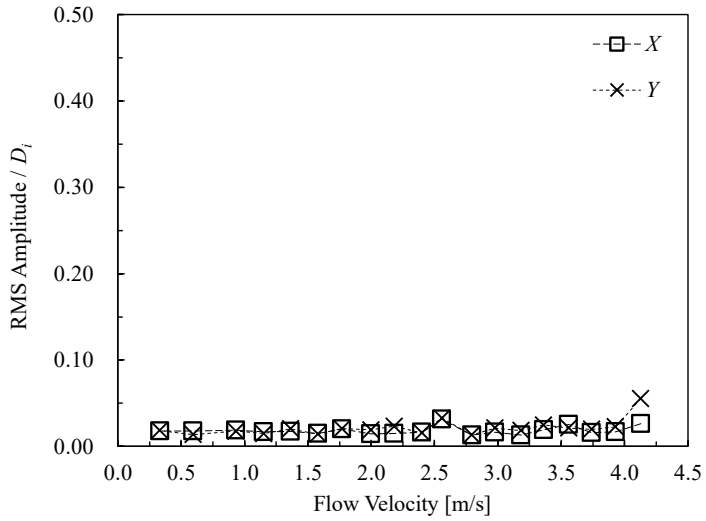

Fig. 4-7 Variation of RMS displacements with internal flow velocity.

Fig. 4-7 shows the summary of the second experiment with the Root Mean Square (RMS) value of tip displacement during the steady state. Although vibrations of 0.02 times of the pipe diameter at all flow velocities through velocity, no significant variation of the amplitude is observed. If the pipe flutters, the amplitude should increase with increasing the flow velocity [80,82]; therefore, this experiment suggests that the model pipe did not flutter during this experiment.

4. 4 Comparison with Existing Model

4.4.1 Existing model

In this section, an existing model is attempted to compare the experimental observations. This subsection initially summarizes the existing linear theory for an aspirating pipe and introduce the method of solving it. Fig. 4-8 shows the mechanical model of a cantilevered pipe conveying fluid. When the flow direction is upward in Fig. 4-8, the system is defined as an aspirating pipe. According to infinitesimal beam theory, the governing equation is described as Eq. (4.1). The equation is essentially the same as in Païdoussis and Luu [72] and Adiputra and Utsunomiya [52,53], with some modifications for considering the fully submerged condition (see Appendix B).

$$\left(m + C_a\rho S_o + \rho S_i\right)\frac{\partial^2 w}{\partial t^2} + c_1\frac{\partial w}{\partial t} + c_2\frac{\partial w}{\partial t}\left|\frac{\partial w}{\partial t}\right| - \frac{\partial}{\partial z}\left(T_e\frac{\partial w}{\partial z}\right) + EI\frac{\partial^4 w}{\partial z^4}$$
$$-2\rho S_i u\frac{\partial^2 w}{\partial z\partial t} + \rho S_i u^2\frac{\partial^2 w}{\partial z^2} = 0 \tag{4.1}$$

$$\text{where,}\quad T_e = T_w + p_o S_o - p_i S_i\,. \tag{4.2}$$

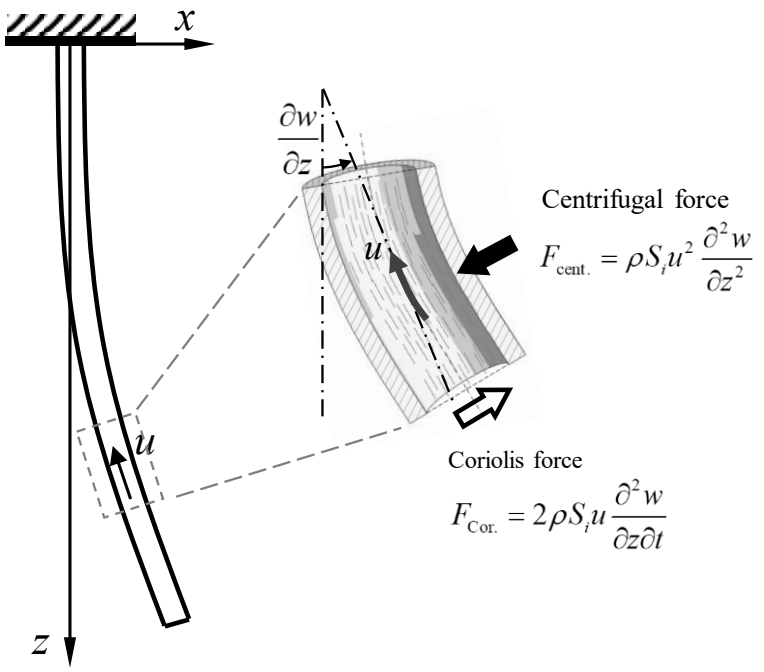

Fig. 4-8 Definition of the cantilevered aspirating pipe and forces acting on an infinitesimal length.

Here, z is the coordinate along the pipe axis, L is length of the pipe (defined here and used below), t is time, w is lateral displacement, m is linear density of the solid part, ρ is fluid density, S is the sectional area, C_a is the added mass coefficient, EI is the bending rigidity and u is the upward flow velocity. Additionally, T_e is the effective tension, widely used in the analysis of submerged pipes and marine risers and its interpretation is given by Sparks [87], T_w is the wall tension and p is pressure, in which the suffix i and o are associated with the inner "contained" fluid column and the outer "displaced" fluid column, respectively. This concept treats the pipe as a composite system, not only solid (pipe wall) part, but also involving inner/outer fluids.

The first line of Eq. (4.1) is as for a typical vertical beam. To enable us to model the experimental system, we consider the damping force due to outer fluid as linear and quadratic terms with coefficients c_1 and c_2, respectively. The second line of Eq. (4.1) is associated with the effect of internal flow. The first term of the second line represents the Coriolis force that decreases the damping, and the second term is the centrifugal force that increases the stiffness. The quadratic damping is not involved in the stability analysis since the effects of internal flow are linear. However, it is a significant term for comparison with the free vibration of submerged pipe in which a drag force is dominant.

The Partial Differential Equation (PDE) Eq. (4.1) is numerically solved by the Finite Element

Method (FEM) in the time integration scheme and the eigenvalue analysis. The details of this approach can be found in Adiputra and Utsunomiya [88]. In the time integration, the nonlinear differential equation, Eq. (4.3), is solved by the Newmark-beta method. In the eigenvalue analysis, eigenvalues of the differential equation are calculated by solving Eq. (4.4). Note that the quadratic damping term is neglected in the eigenvalue analysis.

Differential equation,

$$\mathbf{M}\ddot{\mathbf{W}} + \left[\mathbf{C}_1 - \mathbf{A}(u)\right]\dot{\mathbf{W}} + \mathbf{C}_2\left(\dot{\mathbf{W}}\right) + \left[\mathbf{K} + \mathbf{B}(u)\right]\mathbf{W} = \mathbf{0}. \tag{4.3}$$

Eigenvalue equation,

$$\det\left\{-\omega^2\mathbf{M} + i\omega\left[\mathbf{C}_1 - \mathbf{A}(u)\right] + \left[\mathbf{K} + \mathbf{B}(u)\right]\right\} = 0. \tag{4.4}$$

Here, $\mathbf{W} = [\, w_0\ \theta_0\ w_1\ \theta_1\ \ldots\ w_n\ \theta_n\,]^{\mathrm{T}}$ is the nodal displacement, $\mathbf{M}$ is the mass matrix, $\mathbf{C}_1$ is the linear damping coefficient matrix, $\mathbf{C}_2$ is the quadratic damping force vector, $\mathbf{K}$ is the stiffness matrix, $\mathbf{A}$ and $\mathbf{B}$ are Coriolis and centrifugal force coefficient matrixes depending on flow velocity u, and ω is complex eigenvalue.

In order to assimilate the experimental model pipe and theoretical models, we performed the following processes.

1) Boundary conditions and natural frequency

Since a perfect fixed condition is hard to reproduce in the experiment, a stiff rotating spring is introduced instead at the top fixed end. The bottom end is firstly assumed to satisfy a free condition as

$$\begin{cases} w = 0, & EI\dfrac{\partial^2 w}{\partial z^2} = k_r\dfrac{\partial w}{\partial z} \quad (z = 0), \\ EI\dfrac{\partial^3 w}{\partial z^3} = 0, & EI\dfrac{\partial^2 w}{\partial z^2} = 0 \quad (z = L), \end{cases} \tag{4.5}$$

and the added mass coefficient is assumed as $C_a = 1.0$. Moreover, we first consider an internal frictional pressure loss as a pressure difference between inner and outer fluid [53]. Thus, the effective tension in Eq. (4.2) equals the wall tension obtained by the wet weight $T_w = (mg + \rho S_i g - \rho S_o g)(L - z)$ of the pipe, since the internal frictional pressure loss and wall shear force cancel out. In this case, the stiffness of the rotational spring k_r can be identified from the measured natural

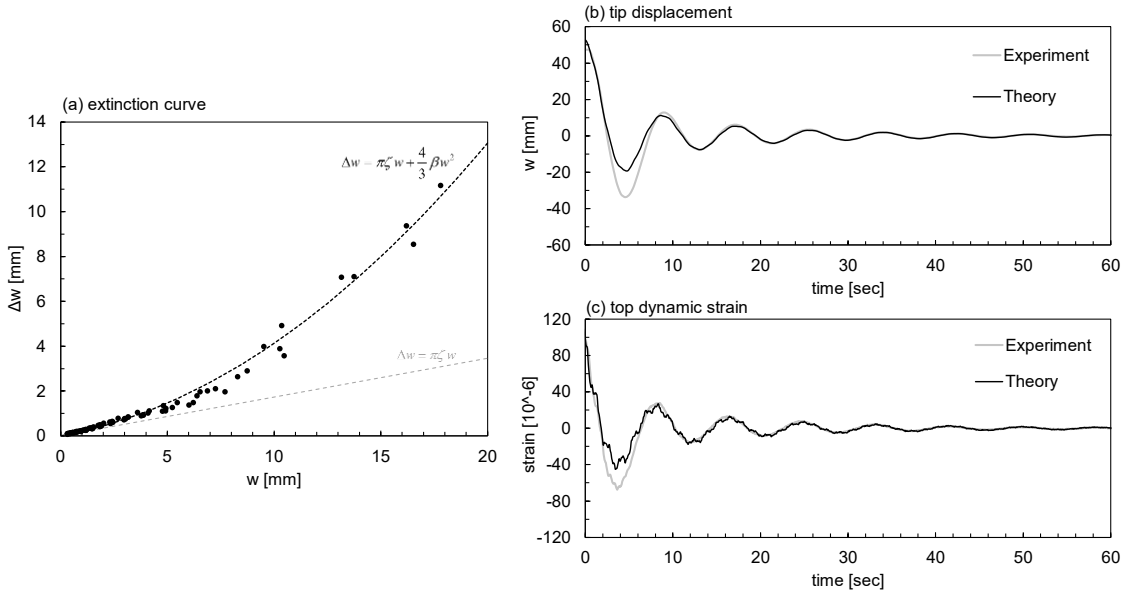

Fig. 4-9 Damping characteristics: (a) extinction curve fitted from the measured plots without the internal flow, (b) tip displacement and (c) top strain compared between an experiment and the theory.

frequency without internal flow.

2) Damping coefficients

The damping coefficients in Eq. (4.1) can be identified from the results of measured free vibration without internal flow. Fig. 4-9 (a) shows the extinction curve of the peaks extracted from the measured free vibration in the first experiment. The horizontal axis is the average amplitude of adjacent peaks, and the vertical axis is the difference between them. The dashed line in Fig. 4-9 (a) shows the quadratic fit curve of the experimental data, and the coefficients represent the linear and quadratic damping ratio of the system as

$$\Delta \mathrm{w} = \pi\zeta w + \frac{4}{3}\beta w^2 , \tag{4.6}$$

where, the linear and quadratic damping ratios are

$$\zeta = \frac{C_1}{2\sqrt{MK}}, \beta = \frac{C_2}{M} . \tag{4.7}$$

Here, M, C_1, C_2 and K are the modal mass, damping and stiffness respectively. The damping coefficients for the analysis can be identified using the modal mass and stiffness for the first mode in Eq. (4.3).

Table 4-2 shows the dynamic characteristics for the first mode identified from the results of six experiments; the linear damping ratio is 5.5%, and the drag coefficient is 1.666 when the quadratic damping ratio is considered as the drag force. The coefficient of variation of the natural period is about 0.6%, while the damping coefficient varies by 30%.

Table 4-2 Identification of experimental dynamic characteristics of the first mode.

Properties	Values
Natural period, T_n	8.530 sec.
Added mass coefficient, C_a	1.0
Top rotational stiffness, k_rL/EI	18.17
Linear damping ratio, ζ	0.055
Quadratic damping ratio, β	17.66 [1/m]

4.4.2 **Comparison and discussion**

Fig. 4-9 (b) and (c) compares the theoretical models with the experimental results. The theoretical models agree very well with measured vibrations. The modeling error in the first few peaks would be the way the initial displacement is handled. In the experiment, the initial displacement was generated by contact with the exciter, whereas in both theoretical models, the initial displacement is made by a load that generates the same initial displacement.

In Fig. 4-10, the theoretical model and experiments with an intake flow velocity of 0.66 m/s are compared. In the theoretical models, the vibration converges to a steady limit cycle instead of zero point which is found in the experiment. This is a typical characteristic of flutter.

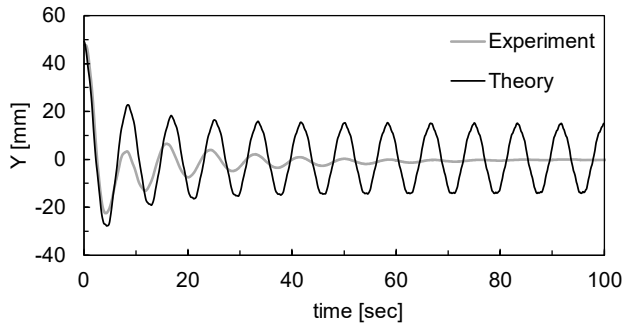

Fig. 4-10 Tip displacement comparison with intake flow velocity of 0.66 m/s; comparison between an experiment and the existing model.

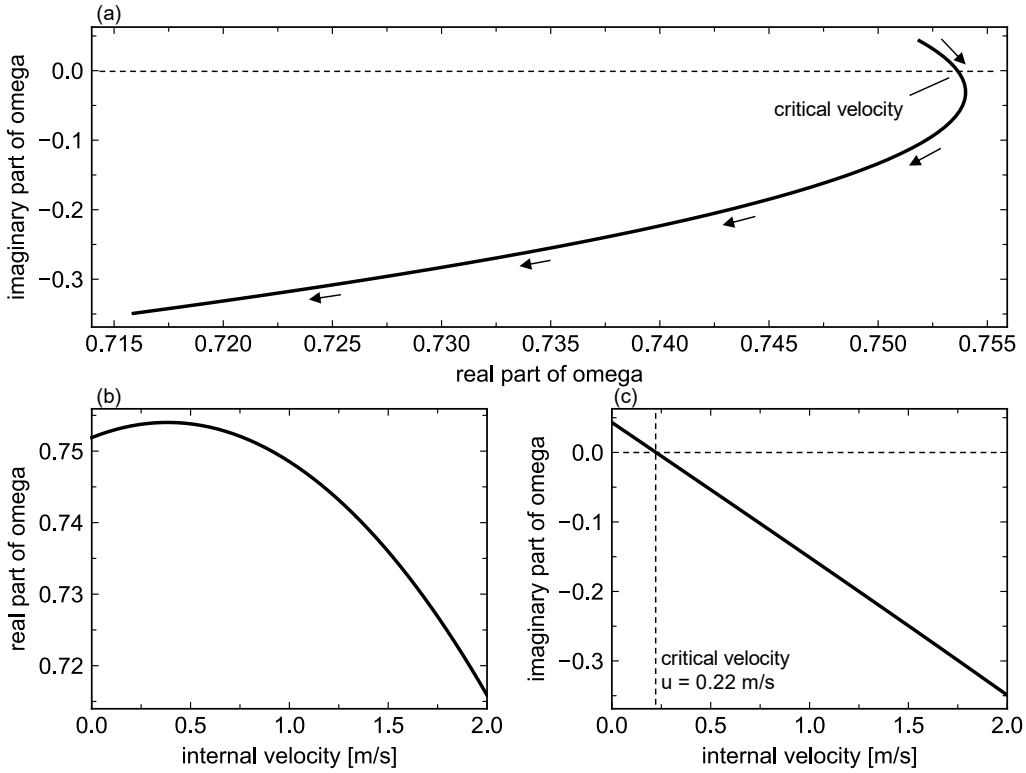

Fig. 4-11 Complex eigenvalues of the first mode with the existing model: (a) Argand diagram, (b) real part, and (c) imaginary part.

The Argand diagram from the eigenvalue analysis is shown in Fig. 4-11 by solving Eq. (4.4). The complex eigenvalue means a variable of exponential function, thus the real and imaginary part correspond to the angular frequency and damping of the system, respectively. In Fig. 4-11, the damping linearly decreases by the effect of Coriolis force. Then the imaginary part becomes negative at the critical velocity of 0.22 m/s. In the subsequent velocity, the vibration is excited by negative linear damping and converges to a constant amplitude due to the effect of quadratic damping as shown in Fig. 4-10.

This phenomenon is inconsistent with the experimental results in which flutter was not observed even at the experimental maximum velocity of 4.1 m/s. This is similar to results in several previous studies, and this study thus reaffirm this through this experimental configuration. It should be highlighted once again that an analysis referring to this default theory will evaluate extremely smaller allowable velocity than the actual critical velocity for OTEC and other ocean systems.

4. 5 Conclusion

As a critical phenomenon for the CWP, there are concerns about a self-induced vibration due to large momentum of internal flow. However, our knowledge of the dynamics of such pipes is based on limited experimental studies and the dynamics would seem not to be definitely established. As stated in section 4.1, the main objective of this chapter is to provide experimental data and insight by taking a new look at the dynamics of a submerged pipe aspirating water. This chapter has reported a tank experiment using a polycarbonate pipe with 4 m length. As the first configuration, the free vibration with internal flow is measured by a set-up in which possible disturbances is removed. As the second configuration, the behavior at a range of high intaking flow velocity generated by a centrifugal vacuum pump is measured. Subsequently, the observations are compared with existing equation of motion of a fluid-conveying pipe and its stability analysis.

In the experiment, a flutter was not observed at a maximum flowrate of 4.1 m/s. In addition, the observed free vibration with internal flow seems to be essentially nonlinear and three-dimensional. Unfortunately, we were unable to provide a deep insight with a 2D linear theory because the behavior is more complex than we initially anticipated. An investigation of the theory of nonlinear spatial motion might lead to establishing this phenomenon.

It should be highlighted once again that an analysis referring to the default theory will evaluate extremely smaller allowable velocity than the actual critical velocity for OTEC and other ocean systems. Importantly, the existing theory and simulation predicted that a self-induced vibration occur at this flow velocity. Therefore, the experiment reveals the necessary to improve the theory.

5 THEORETICAL INVESTIGATION OF A PIPE ASPIRATING FLUID: A NEW INLET FIELD MODEL

5. 1 Introduction

The inconsistency, which was reaffirmed in the previous chapter, has been experimentally and theoretically corroborated by three individual works. The works have proposed hypotheses that incorporate the effects of inlet flow at the free end of the pipe. In this chapter, we firstly review the outlines of these theories and consider their applicability in comparison with our experiment.

Païdoussis [78] found similarities in this problem with Feynman's reverse sprinkler. In this discussion, the negative pressurization at the entrance $p_i S_i = -\rho S_i u^2$ cancels the centrifugal forces in Eq. (4.1), hence the pipe does not flutter. Subsequently, Kuiper and Metrikine [89] suggested that the Coriolis force in Eq. (4.1) still causes flutter, and they proved that by practically solving the equation.

Cui and Tani [77] argued that there is a tip damping force $EIw_L''' = -\rho S_i u \dot{w}_L$ in addition to the negative pressurization at the entrance. Unfortunately, they did not offer any explanation for the derivation process and the physical sense. Pramila [76] also puts forward the tip force as: $EIw_L''' = -\rho S_i u\left(\dot{w}_L - uw_L'\right)$, in which the force seems to additionally consider the vectored thrust due to jet.

Païdoussis and co-authors [79,80] reappraised the inlet flow model based on the insight by Pramila. Two key assumptions have been introduced in this model: (i) there is a small mean flow

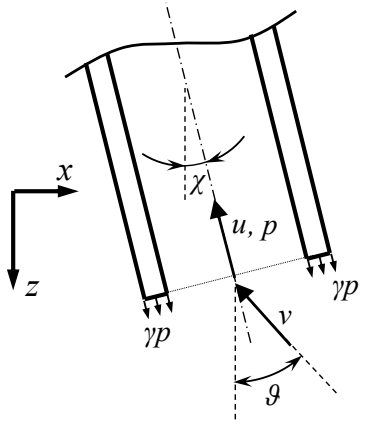

Fig. 5-1 Definition diagram for the inlet flow field based on [78,79].

velocity just facing the entrance of the pipe; (ii) there exists an additional mean tension, related to the flow over the inlet edge. Based on this assumption, the tip force is evaluated by several parameters which express the geometry of flow facing the entrance. Considering the model as shown in Fig. 5-1 the tip forces are described as Eqs. (5.1), (5.2) and (5.3),

$$F_x = \rho S_i u\left[\left(\dot{w}_L - u\sin\chi\right) - \left(-v\sin\vartheta\right)\right] + p_i S_i \sin\chi\,, \tag{5.1}$$

$$F_z = \rho S_i u\left[\left(-u\cos\chi\right) - \left(-v\cos\vartheta\right)\right] + p_i S_i \cos\chi\,, \tag{5.2}$$

$$T_w\left(L\right) = -\gamma p_i\left(S_o - S_i\right). \tag{5.3}$$

Here, χ is tangential angle of the entrance of the pipe, v and ϑ are velocity magnitude and angle of flow facing the entrance, respectively, γ is coefficient of the edge pressure, S_o is total cross-sectional area of the pipe and enclosed fluid, and the inlet pressure: $p_i S_i = -0.5\rho S_i u^2$.

The past decade has focused on the investigation into the influence and sensitivity of the parameters. A number of studies have found that these parameters sensitively govern the stability of the pipe [80,81,83,85]. Namely, a slight change in these parameters could significantly change the critical velocity. This raises the question of how to accurately identify parameters for comparison with the experiment or a practical design of the pipe. Moreover, there seems to be ambiguity with regard to the definition of the flow vector just facing the entrance. In fact, comparisons with experiments have been made by estimating the range of the parameters.

The literature cited above has shown that the inlet effect is undoubtedly important for the behavior of aspirating pipes; however, the flow model would seem to need to be improved. Therefore, in subsequent subsections, we attempt to refine the previous models by revisiting the phenomena at the entrance of aspirating pipe.

5. 2 **Numerical Investigation of Inlet Flow Field**

The inlet flow around the entrance of a pipe deeply inserted into a large water tank was experimentally investigated in early hydraulics. The engineering interest has tended to focus on a pressure loss coefficient rather than such a flow structure. Recently, Giacobbi et al. [80] conducted a Computational Fluid Dynamics (CFD) simulation, and they provided a detailed discussion on the velocity and pressure distribution on the pipe axis of $\pm 0.3D$ from the entrance. By contrast, in this study, we re-examine it focusing on the macroscopic flow structure and pressure distribution around the circumference by using a CFD simulation.

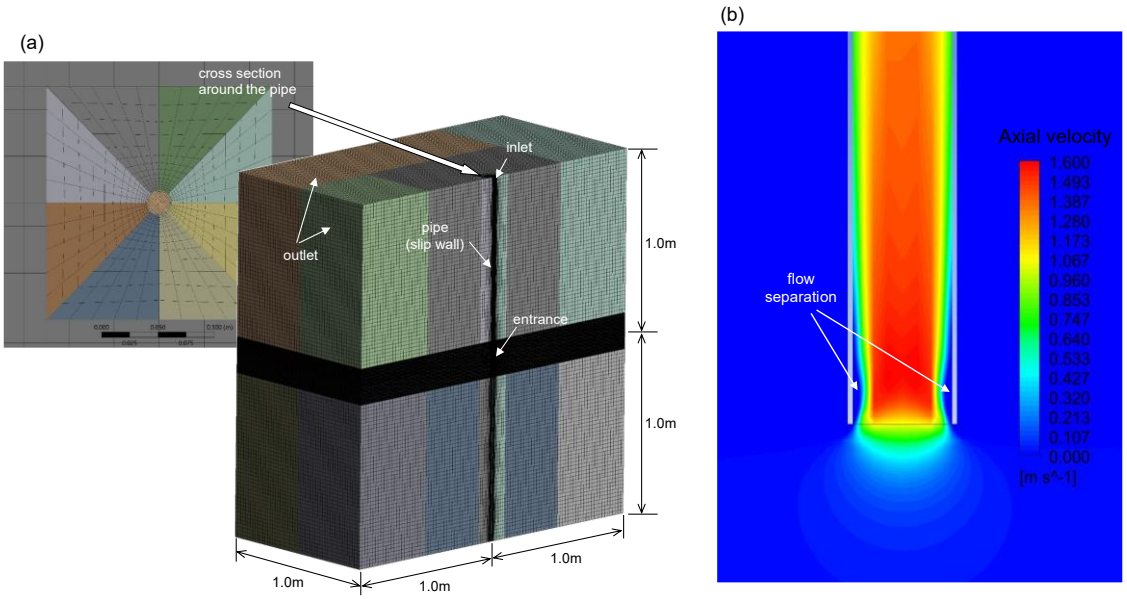

Fig. 5-2 (a) Meshed half fluid region and the cross-section around the pipe for ANSYS Fluent, (b) contour of axial flow velocity for 1.0 m/s inlet.

The flow around the pipe entrance simulated by ANSYS Fluent is represented in Fig. 5-2. The cross-sectional shape of the pipe is the same as the experimental model in chapter 4 (see Table 4-1), and a 1 m length pipe is aspirating water from a 2×2×2 m cubic fluid domain (with density $\rho = 1{,}000$ kg/m^3). The pipe wall is rigid and wall slip is assumed in order to eliminate the influence of frictional pressure loss. This assumption is also reasonable for the turbulent flow in which the Reynolds number $Re > 10^4$. Since the flow is very sensitive to the asymmetry of the mesh, we take care to generate a symmetric mesh by using hexahedral elements, as shown in Fig. 5-2 (a).

As shown in Fig. 5-2 (b) representing the velocity contour, external fluid is gradually accelerated as it approaches the pipe entrance. This also causes a change in momentum on the pipe surface. Since the pipe wall is a slip-wall and the flow is perfectly symmetrical, the tensile force can be acting only on the pipe edge among the solid parts here. We confirm that the force of 11 % of the flow momentum acts in the axial direction. After the fluid subsequently passes through the entrance, the contracted jet is formed by separating from the pipe wall (this phenomenon has been well known as the *vena contracta*). As the flow goes downstream, it mixes with the surrounding fluid, generates a vortex, and eventually reattaches on the pipe wall to form a uniform flow. In this flow development, the mixing and vortex cause pressure loss.

We next evaluate the flow forces for the same model as in Fig. 5-2. As a practical evaluation, the model considers an external cross flow instead of velocity of the pipe itself. Namely, it computes the forces acting on the solid surface of the pipe, in which the external cross-flow velocity v and the internal flow velocity u exist together. As a result, the velocity contours around

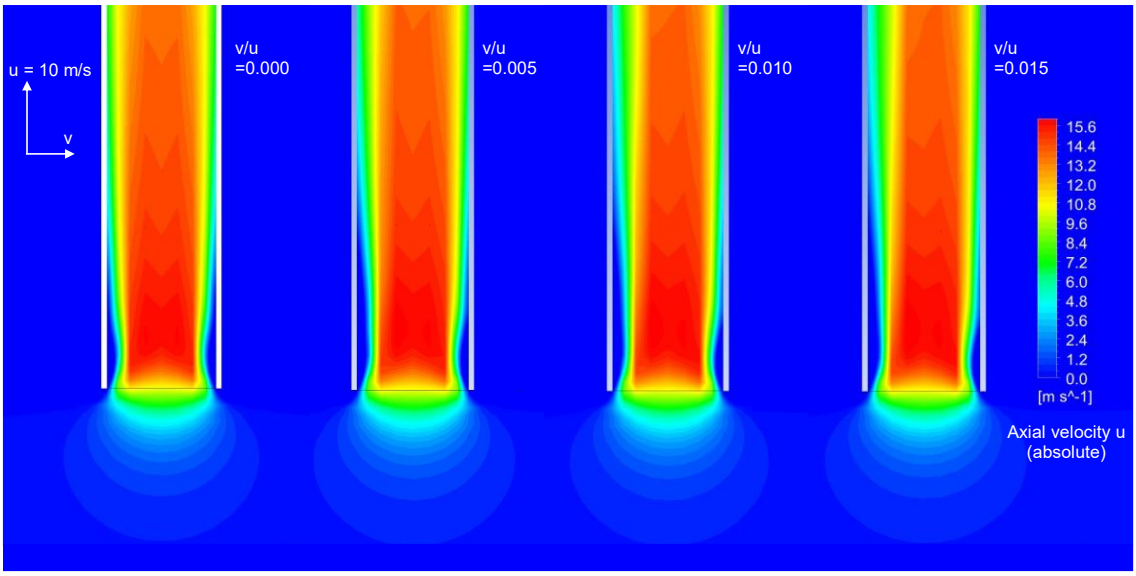

Fig. 5-3 Contour of axial flow velocity for varying ratios of the internal velocity u and the cross flow velocity v.

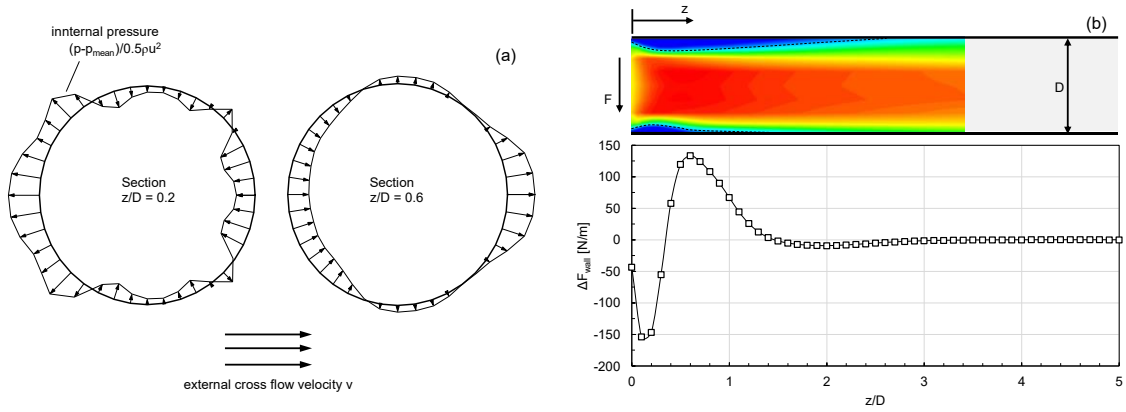

Fig. 5-4 (a) Pressure distribution of the cross section at z/D = 0.2, 0.6, and (b) line-integrated force distribution for v/u = 0.017.

the entrance are shown in Fig. 5-3. The pressure distribution around the circumference and its line-integrated force ΔF_{wall} distribution along the pipe axis are also shown in Fig. 5-4. Fig. 5-3 illustrates that the flow beyond the entrance is separated asymmetrically, and the jet formed downstream is inclined in the same direction as the external flow. Consequently, as visually demonstrated in Fig. 5-4 (a), a pressure resistance is caused by the unbalance in the pressure distribution on the pipe inner wall.

In conclusion, the fluid phenomena at the inlet end are the following: (a) the pressure loss due to the mixing and vortex during the contracted flow and its reattachment, (b) the end pressure on the edge of the inlet, and (c) the pressure resistance related to the pipe behavior. Although the pressure is strictly distributed on the inner wall of the pipe, it can be regarded as boundary

conditions, as in the previous models. The distribution of the pressure resistance is illustrated in Fig. 5-4 (b), in which we can confirm it converges at $z/D = 3$. When the D/L is sufficiently small, this force can be therefore regarded as a concentrated force acting at the tip.

Previous models assume flow vectors just inside and outside the entrance. However, the results would seem to indicate that this is not suitable for evaluating flow momentum because the flow field just around the entrance is complex and involves a large gradient. Instead of that, considering the macroscopic flow structure as a control region may be used to derive a new analytical model that does not include parameter assumptions.

5. 3 **New Inlet Flow Model**

We consider the simplified model of the inlet flow as shown in Fig. 5-5, which firstly assumes that the pipe is fixed, and the static pressure is neglected. To consider the forces and the pressure loss, we have three control surfaces in Fig. 5-5 (a): I. a virtual surface around the entrance, II. the cross-section of the jet at the highest velocity and III. the cross-section developed into uniform flow far downstream. Firstly, we consider the region between I and II. In this region, the flow can be regarded as a conservative flow. On surface I, the velocity u_1 and the pressure p_1 are zero because the area can be regarded as infinite. On surface II, the velocity is assumed as $u_2 = au$, where a represents the increase of the velocity due to the contraction, and S_e is the corresponding effective area. The pressure p_2 is evaluated by using Bernoulli's principle as

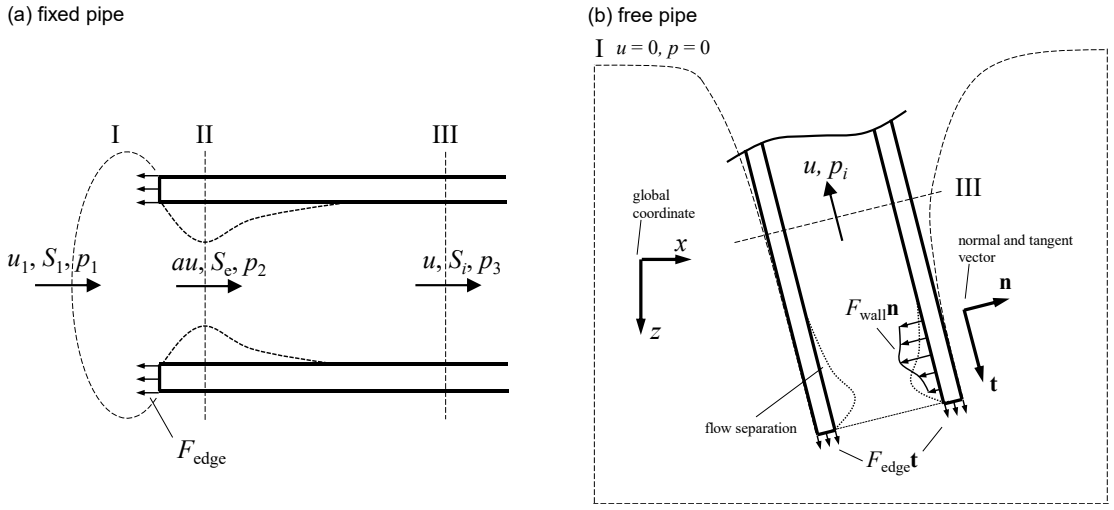

Fig. 5-5 New inlet field model: (a) control surfaces of an inlet flow field for a fixed pipe entrance, and (b) control surfaces and forces acting on the pipe for a free pipe entrance.

$$p_2 = -a^2 \frac{\rho u^2}{2}. \tag{5.4}$$

While the fluid passes through the entrance, the change in momentum does work on the normal to the solid surface. In this case, the surface is the edge of the pipe, and the reaction is defined as F_{edge},

$$F_{\text{edge}} = \left(\frac{a^2}{2} - a \right) \rho S_i u^2. \tag{5.5}$$

Secondly, we consider the region between II and III. In this region, the flow energy is dissipated by mixing and vortex formation during the flow separation and its reattachment. The pressure loss coefficient k is defined in advance, then the conservation of momentum and the difference in energy yield the relationship between k and a as

$$k = (a-1)^2, \tag{5.6}$$

$$p_3 = -(1+k)\frac{\rho u^2}{2}. \tag{5.7}$$

This relationship is also used for the evaluation of the pressure loss due to a pipe with sudden contractions by using an empirical contraction coefficient a^{-1}. However, in the case of this problem, we continue the discussion with k as a parameter, since it may be easily observable. Then, by applying the relationship in Eq. (5.6) to Eq. (5.5), we also have

$$F_{\text{edge}} = -\frac{1}{2}(1-k)\rho S_i u^2 \tag{5.8}$$

The coefficient k relates to the shape of the entrance, such as the wall thickness, beveled and rounded.

We next consider the free pipe which can behave in the 2D plane as shown in Fig. 5-5 (b). The flow structure is basically the same as in Fig. 5-5 (a) in which the jet occurs beyond the entrance

and develops into a uniform flow. This model may be reasonable when the velocity of the pipe overall is sufficiently small compared to the internal flow velocity u and the flow can be regarded as turbulent.

The control surface I in Fig. 5-5 (b) is the virtual surface around the entrance and the pressure and velocity are zero on it. The control surface III is the cross-section on which the flow develops to uniform. In this region between I and III, we consider the reaction force F_{inlet} due to the relative motion of the fluid and the pipe wall. This can be divided into the reaction acting on the edge as in Eq. (5.8) and the reaction with the inner wall of the pipe F_{wall}. Then, a conservation of momentum gives,

$$\rho S_i u\left[\left(\frac{\partial \mathbf{r}}{\partial t}-u\mathbf{t}\right)-0\right]=p_i S_i \mathbf{t}+F_{\text{edge}}\mathbf{t}-F_{\text{wall}}\mathbf{n}, \tag{5.9}$$

where, $\mathbf{r}$ is the position vector in a global coordinate system and p_i is internal pressure which is represented in Eq. (5.7). Thus, $\mathbf{F}_{\text{inlet}}$ can be expressed as

$$\mathbf{F}_{\text{inlet}}=F_{\text{edge}}\mathbf{t}-F_{\text{wall}}\mathbf{n}=\rho S_i u\frac{\partial \mathbf{r}}{\partial t}-\frac{1}{2}(1-k)\rho S_i u^2\mathbf{t}. \tag{5.10}$$

The advantage of Eq. (5.10) is that it describes the force and pressure loss with only one physically meaningful coefficient k. Furthermore, the relationship between entrance pressure loss and edge force by Eqs. (5.6)-(5.8) suggests the effects of the flow separation and jet formed inside of the pipe entrance on the motion of the aspirating pipe. Since Eq. (5.10) is the surface integral of the dynamic pressure on the solid part actually, the boundary condition of the inlet end of the pipe is described by using the shear force $Q(L)$ and axial force $T_w(L)$ as

$$Q\mathbf{n}+T_w\mathbf{t}=-\mathbf{F}_{\text{inlet}}. \tag{5.11}$$

5. 4 **Equation of Motion**

From the foregoing, we have supplemented the physical implications of the inlet flow and have refined the loading and boundary conditions at the inlet end. As stated in the literature review, the inlet flow highly governs stability of the aspirating pipe. Therefore, reflecting this in Eqs. (4.1)

and (4.2) may significantly change the nature of the equation of motion. At first, the differential equation of effective tension is expressed as

$$\frac{\partial T_e}{\partial z} = -\left(mg + \rho S_i g - \rho S_o g\right) \tag{5.12}$$

Integrating Eq. (5.12) along z, then the effective tension distribution is obtained.

$$T_e = -\left(mg + \rho S_i g - \rho S_o g\right) z + C\,, \tag{5.13}$$

where the boundary condition of T_e (L) is imposed to obtain the integral constant C. Considering the effect of the static ambient pressure $p_o S_o$ on Eqs. (5.7) and (5.8), we have

$$\begin{cases} T_w(L) = \dfrac{1}{2}(1-k)\rho S_i u^2 - p_o\left(S_o - S_i\right), \\ p_i S_i(L) = p_o S_i - \dfrac{1}{2}(1+k)\rho S_i u^2. \end{cases} \tag{5.14}$$

Here, the wall tension T_w (L) is based on the edge force of Eq. (5.7), and it means that the dynamic pressure on the edge of the pipe slightly reduces the buoyancy of the pipe. The inner pressure $p_i S_i$ represents a pressure drop from the outer pressure. By the definition of the effective tension, T_e (L) = $\rho S_i u^2$. Thus, the effective tension distribution is

$$T_e(z) = \left(mg + \rho S_i g - \rho S_o g\right)(L - z) + \rho S_i u^2. \tag{5.15}$$

Next, the boundary condition of Eq. (5.11) is also linearized as

$$EI\frac{\partial^3 w}{\partial z^3} + T_w\frac{\partial w}{\partial z} = -\rho S_i u\frac{\partial w}{\partial t} + \frac{1}{2}(1-k)\rho S_i u^2\frac{\partial w}{\partial z} - p_o\left(S_o - S_i\right)\frac{\partial w}{\partial z}. \tag{5.16}$$

Then, both terms of tension effect on the left and right sides have canceled out, thus the boundary

condition is described as only the end shear force and pressure resistance as

$$EI\frac{\partial^3 w}{\partial z^3} = -\rho S_i u\frac{\partial w}{\partial t}. \tag{5.17}$$

Finally, substituting Eq. (5.15) in Eq. (4.1), the equation of motion is

$$\begin{aligned}&\left(m + C_a\rho S_o + \rho S_i\right)\frac{\partial^2 w}{\partial t^2} + c_1\frac{\partial w}{\partial t} + c_2\frac{\partial w}{\partial t}\left|\frac{\partial w}{\partial t}\right| \\ &-\frac{\partial}{\partial z}\left[\left(mg + \rho S_i g - \rho S_o g\right)\left(L - z\right)\frac{\partial w}{\partial z}\right] + EI\frac{\partial^4 w}{\partial z^4} - 2\rho S_i u\frac{\partial^2 w}{\partial z\partial t} = 0.\end{aligned} \tag{5.18}$$

Also, we have the boundary conditions

$$\begin{cases} w = 0, & EI\dfrac{\partial^2 w}{\partial z^2} = k_r\dfrac{\partial w}{\partial z} \quad (z = 0), \\ EI\dfrac{\partial^3 w}{\partial z^3} = -\rho S_i u\dfrac{\partial w}{\partial t}, & EI\dfrac{\partial^2 w}{\partial z^2} = 0 \quad (z = L). \end{cases} \tag{5.19}$$

Eqs. (5.18) and (5.19) do not involve the entrance pressure loss coefficient *k*; therefore, the behavior is not affected by the pipe inlet shape (the wall thickness, beveled and rounded, etc.). This result is consistent with the experiments that investigated the effects of different pipe end-pieces [80,85]. Furthermore, this derivation concurs with the equation by Cui and Tani [77], in which the derivation process is unknown. Crucially, the centrifugal force due to the internal flow completely cancels with the final term on the right side of Eq. (5.15), as also highlighted by Cui and Tani [77] and Païdoussis [78].

5. 5 **Comparison of New Model with Experiment**

Eqs. (5.18) and (5.19) above describe the behavior of the aspirating pipe which we are most interested in. Besides, the physical interpretations that have been revealed in this section can provide new information for comparison with the experiment. In particular, the internal pressure and the axial strain may be measurable and comparable with

$$p_i(z) = p_o(z) - \left(1 + k + f\frac{L-z}{D_i}\right)\frac{1}{2}\rho u^2, \tag{5.20}$$

$$\varepsilon = \frac{T_e}{E(S_o - S_i)} + (1-2\nu)\frac{p_i S_i - p_o S_o}{E(S_o - S_i)}, \tag{5.21}$$

where, f is frictional loss coefficient, ε is the axial strain without bending strain and ν is the Poisson ratio.

In this experiment, the axial strain is measured at $z = 0$. Based on the hydraulic head between the surge tank and deep water tank measured in the first experiment, the pressure loss coefficient can be determined as $k + fL/D_i = 5.75$ and the static pressure $p_o = 21{,}560$ Pa. Thus, the increase in axial strain at $u = 1.66$ m/s from 0 m/s is predicted as 0.57 μ with Eq. (5.21). The measurement resolution of 1.0 μ is insufficient to accurately compare with this. However, at least, we have confirmed that the increase in axial strain measured is less than 1.0 μ at $u = 1.66$ m/s and it increases with flow velocity. For the second experiment, the pressure loss coefficient could be estimated as $k+fL/D_i = 2.0$ and the static pressure $p_o = 1{,}960$ Pa. With Eq. (5.21), the axial strain is 18 μ, which order is also good agreement with the experimental result in Fig. 4-6.

Next, Eqs. (5.18) and (5.19) are practically solved and compared with the experiment. The solution method and parameters are the same as for Eq. (4.3) described in chapter 4. Fig. 5-6 shows the comparison of the theoretical model and experiments with an intake flow velocity of 0.66 and 1.66 m/s. Although the experimental result can hardly be considered to be a two-dimensional free damped vibration and could not be compared quantitatively with theoretical models, the theoretical models seem to reproduce the natural period and amplitude, especially in

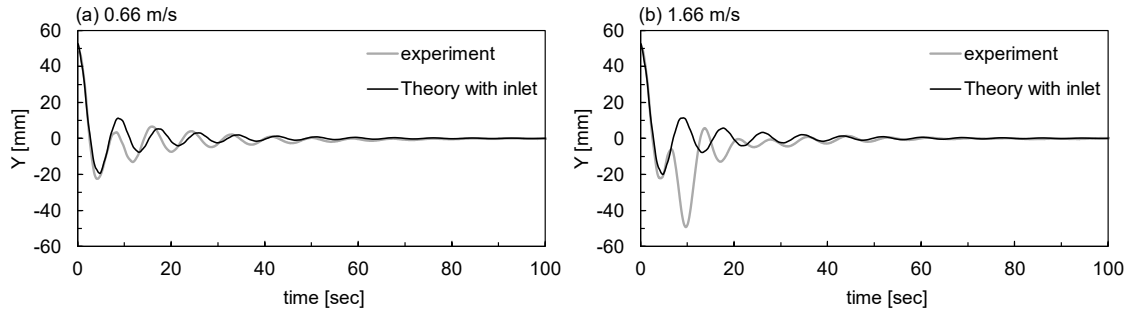

Fig. 5-6 Tip displacement comparison with intake flow velocity of 0.66 m/s and 1.66 m/s; comparison between an experiment and the theoretical analysis with the inlet flow model.

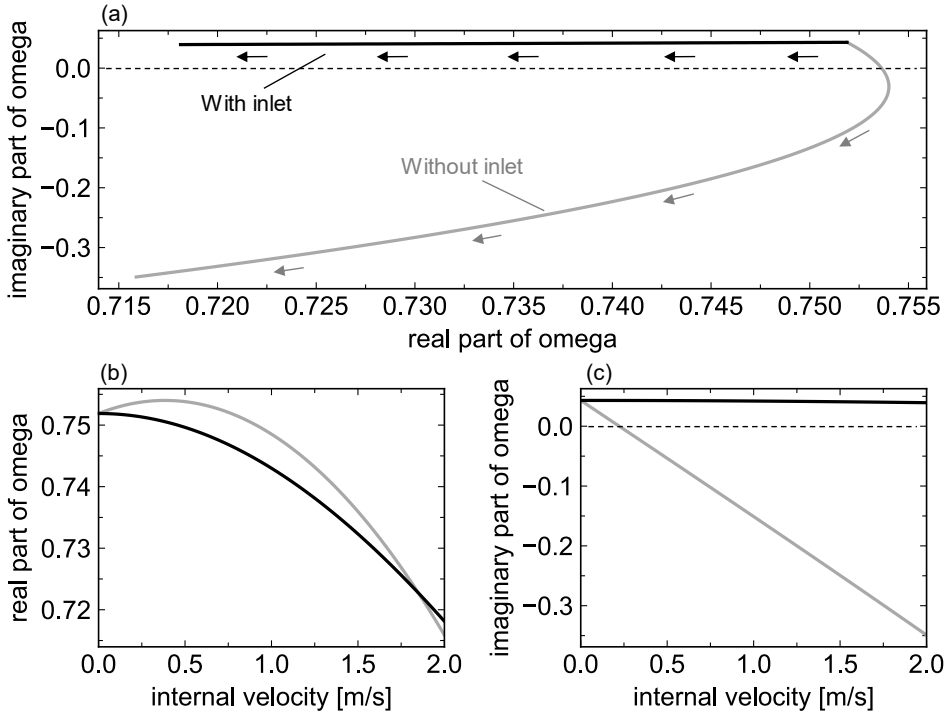

Fig. 5-7 Complex eigenvalues of the first mode with the new inlet flow model: (a) Argand diagram, (b) real part, and (c) imaginary part.

the latter part of the vibration.

In addition, Fig. 5-7 shows the Argand diagram of the first mode of Eqs. (5.18) and (5.19) that were obtained by solving by the same method as Eq. (4.4). Comparing Fig. 5-7 with Fig. 4-11, the change in the damping of the system is very gradual. This is because the pressure resistance in Eq. (5.17) makes obtuse the effect of the Coriolis force. On the other hand, the angular frequency of the system slightly decreases, as well as that with the free end in Eq. (4.1). Unfortunately, these changes in the frequency and the damping are small; thus, we did not result in significant changes with increasing velocity through the experiment.

The most remarkable point in Fig. 5-7 is that a critical velocity does not appear in this velocity range. There expects to be the critical velocity at least in this range based on the previous theory Eqs. (5.1), (5.2) and (5.3), however, this new theory leads to a different result. A more detailed analysis with the same model is shown in Fig. 5-8. It is apparent from Fig. 5-8 that the imaginary part of the eigenvalues asymptotically approaches the real axis as the flow velocity increases and does not become negative for any high velocities in the analysis. Besides, the same result can be seen for any damping coefficients $c_1 \geq 0$. Eqs. (5.18) and (5.19) numerically indicate that the system will be stable at any velocity, and therefore, the submerged pipe aspirating water does not flutter.

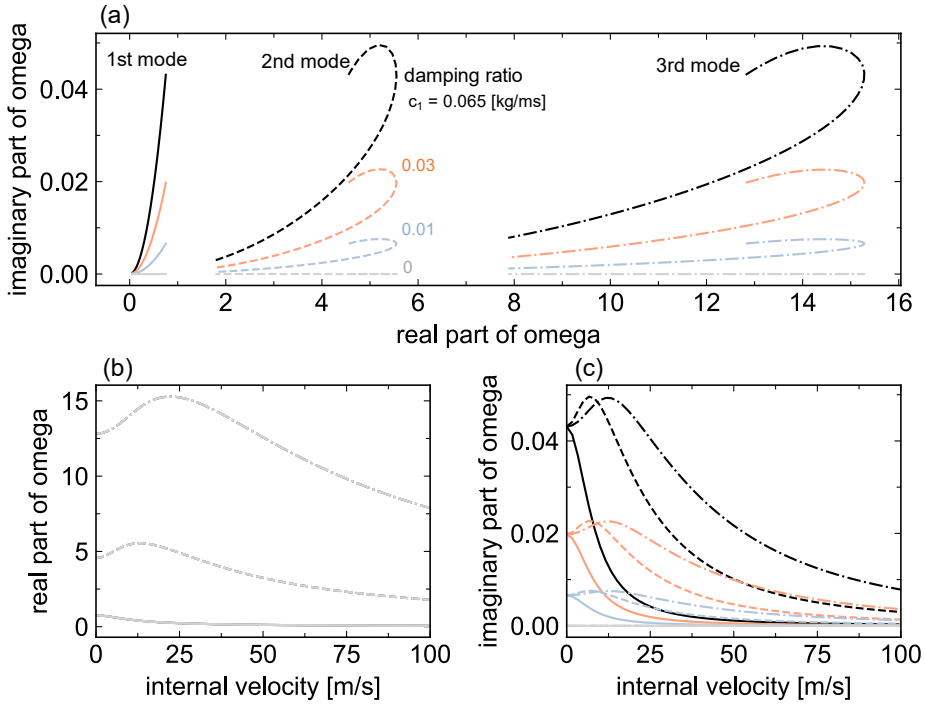

Fig. 5-8 Complex eigenvalues of the first to third mode on variable damping ratio with the new inlet flow model: (a) Argand diagram, (b) real part, and (c) imaginary part.

The centrifugal force due to the internal flow is completely lost from Eq. (4.1). Note that a critical velocity would appear if the term $A\rho S_i u^2(\partial^2 w/\partial z^2)$, where a coefficient $A > 0$, remains in Eq. (5.18). This has not been mathematically proven, and its influence would not be completely ruled out through these experiments. Whereas, according to Païdoussis' literature review [75], there is another experiment to demonstrate stability even at high velocities. For these reasons, further work should be carried out to resolve this problem.

5. 6 **Conclusion**

The inlet flow at the free end of the pipe has a critical role in the evaluation of stability. In this thesis, it has highlighted again that analysis without inlet flow will predict flutter which was not observed in the experiment. This chapter have proposed a model which considered the flow separation and jets that form at the inlet of the pipe based on the CFD simulation. This model seems to reproduce the natural period and amplitude of the free vibration up to 1.6 m/s of the internal flow. Regarding stability, this model is theoretically suggested that the pipe does not flutter. The finding has been well supported by the experimental observation that the flutter could not observed within 4.1 m/s.

So far this and the previous chapters have discussed the basic theory of a fluid aspirating pipe.

Finally, the correspondence between an actual OTEC CWP and the theory and experiment are considered here. With Eqs. (5.18) and (5.19), the nondimensional equation of motion is denoted as,

$$\frac{\partial^2 \tilde{w}}{\partial \tilde{t}^2} + \zeta_1 \frac{\partial \tilde{w}}{\partial \tilde{t}} + \zeta_2 \frac{\partial \tilde{w}}{\partial \tilde{t}} \left| \frac{\partial \tilde{w}}{\partial \tilde{t}} \right| - 2\mu^{1/2} \tilde{u} \frac{\partial^2 \tilde{w}}{\partial \tilde{z} \partial \tilde{t}} - \frac{\partial}{\partial \tilde{z}} \left[\gamma (1 - \tilde{z}) \frac{\partial \tilde{w}}{\partial \tilde{z}} \right] + \frac{\partial^4 \tilde{w}}{\partial \tilde{z}^4} = 0, \tag{5.22}$$

$\tilde{u}$

$$\frac{\partial^3 \tilde{w}}{\partial \tilde{z}^3} = -\mu^{1/2} \tilde{u} \frac{\partial \tilde{w}}{\partial \tilde{t}}, \frac{\partial^2 \tilde{w}}{\partial \tilde{z}^2} = 0, \quad \text{for } \tilde{z} = 1. \tag{5.23}$$

here, the nondimensional parameters are,

$$\begin{aligned}
&\tilde{w} = \frac{w}{L},\ \tilde{z} = \frac{z}{L},\ \tilde{t} = \sqrt{\frac{EI}{\left(m + C_a \rho S_o + \rho S_i\right) L^4}} t, \\
&\zeta_1 = \frac{c_1 L^2}{\sqrt{\left(m + C_a \rho S_o + \rho S_i\right) EI}},\ \zeta_2 = \frac{c_2 L}{m + C_a \rho S_o + \rho S_i}, \\
&\tilde{u} = \sqrt{\frac{\rho S_i}{EI}} uL,\ \mu = \frac{\rho S_i}{m + C_a \rho S_o + \rho S_i},\ \gamma = \frac{\left(mg + \rho S_i g - \rho S_o g\right) L^2}{EI}.
\end{aligned} \tag{5.24}$$

Where, the important nondimensional parameters are the flow velocity , the mass ratio μ and the Reynolds number *Re*. The maximum flow velocity of the experimental model pipe has $\tilde{u} = 3.0$, μ = 0.405 and *Re* = 8×10^4. Meanwhile, the actual OTEC CWP as shown in Table 2-1 has nondimensional values: $\tilde{u} = 0.45$, μ = 0.472 and *Re* = 2.5×10^7. Although a possible influence of other parameters cannot be ruled out, it may be generally considered that the velocities in this experiment sufficiently higher than the operating range of an OTEC.

The dynamics of aspirating pipe has been sparsely studied and our knowledge was limited. We have provided experimental observations and new physical insights; as a result, the present model has theoretically indicated that the aspirating pipe submerged in water may not flutter. Whereas, considering there are several experiments and numerical simulations that observed vibration due to internal flow, the final conclusion must be given with caution. Proof that aspirating pipe does not flutter is more difficult than proving its existence. We hope that our experiment and insights are helpful in solving the difficulty.

6 GENERAL CONCLUSIONS

As states in chapter 1, Introduction, the overall objective of this thesis is to clarify the design methodology of a floating OTEC plant and its mechanical characteristics through a preliminary design of a 100 MW plantship. Comparing to an offshore oil and gas riser, the main characteristics of CWP is that: (i) the diameter is significantly large, (ii) it contains a large mass flow rate, (iii) it is always hanged off even during operation, and thus (iv) the lower end is open in underwater. This study has mainly focused on two dynamic characteristics and phenomena caused by these factors below,

(1) The dynamic interaction between a ship-shaped platform, mooring and CWP,

(2) Self-induced vibration due to internal flow.

As the study case, this study has selected the concept of a 100 MW-NET OTEC plantship, which reflects design philosophy of a FPSO proposed by Adiputra et al. This study has specified the hull geometry, mooring system, CWP and environmental conditions to confirm the technical feasibility and to examine these interactions. A spread mooring system has been considered preferable as a position keeping system. Preliminary designs by several combinations of a flexible joint, a clump weight for the CWP, taut mooring system and catenary mooring system has been compared on their dynamic behavior by using OrcaFlex.

This study has confirmed the validity of both specific catenary mooring system and the taut mooring system for the ship-shaped platform. The environmental conditions and assumptions were not definitely high resolution, nevertheless this result would suggest that the OTEC plantship with a spread mooring system could be technically feasible at calm and directional environment.

The case study has highlighted that the interaction is generally significant, and a direct coupling analysis would be more reasonable for the design. Moreover, this also has yielded the following findings for this concept.

1. Since the FRP-CWP is a lightweight and has a large projected area, the rigid body rotation due to current is predominant. The static deflection could be controlled by installing the flexible joint at the top and the clump weight at the bottom.
2. The dynamic response of the CWP due to the ship motion has been predominant for the design loads. The design loads would increase 2-10 times of the static tension, shear and

bending moment.

3. A one-way coupling analysis might estimate the conservative design loads. Whereas the current force acting on the CWP would need to be considered to design the mooring system.

These findings might be helpful to a further feasibility study including more detailed design of a plantship and mooring system, development of a CWP, and estimation of these costs.

A requirement for the coupled analysis has led to systematically understand the coupled response characteristics, such as the natural frequency and frequency response of the platform and CWP. This study has constructed a simplified analysis model/method which facilitates the preliminary design of an OTEC floating plant and explanation of the results of numerical simulations and model experiments. It has been observed that this model has predicted the coupled response with practically sufficient accuracy for the early design stage. Meanwhile, in the later design stages, the hydrodynamic forces and nonlinearity of the mooring system, nonlinearity of the CWP and 3D motions need to be addressed.

The present model/method has the advantage of providing the coupled response at the early stage of design, and it can deal with more design cases and sensitivity of design parameters at this time. As a preliminary design method applying present model, the influence of the variation of design parameters to the coupled response characteristic has been discussed through the parametric analysis of bending rigidity, linear density, top rotational stiffness and mass of clump weight. It could facilitate an early stage of design and could contribute to an effective planning of the complex floating plant.

Stability of the CWP due to internal flow can be described by a fundamental theory of fluid-aspirating pipe. However, our knowledge of the dynamics of such pipes has been based on limited experimental studies and the dynamics would seem not to be definitely established. To apply a design methodology for CWP, this study has pursued the dynamics experimentally and theoretically. The principal achievement and findings of this study are as follows:

1. This study has established two experimental set-ups and method with a polycarbonate pipe with 4 m long for a wave tank with the depth of 7 m.
2. With the first experiment, the observed free vibration with internal flow has seemed to be essentially nonlinear and three-dimensional.
3. In the second experiment, flutter was not observed at a maximum flowrate of 4.1 m/s. This observation has highlighted that a theory which does not consider an inlet effect will evaluate

extremely smaller allowable velocity than the actual critical velocity for OTEC and other ocean systems.

4. This study has provided a new model of the inlet flow field, which plays an important role on stability, considering the flow separation and jet formed inside of the pipe entrance. The model seems to reproduce the experimental natural period and amplitude of the free vibration with internal flow.

5. The new model also suggests that a CWP does not flutter. This has been supported by the experimentally attained flow velocity of 4.1 m/s, which is sufficiently higher than the operating range of an OTEC system.

APPENDIX A

A. 1 Mode Functions

The analytical solution shown in this appendix can be used for the mode function in Eq. (3.9). The governing equations of a lateral and axial deflection of an infinitesimal Bernoulli-Euler beam are:

$$m_l \frac{\partial^2 w}{\partial t^2} + EI \frac{\partial^4 w}{\partial x^4} = 0\,, \tag{A.1}$$

$$m_a \frac{\partial^2 u}{\partial t^2} - EA \frac{\partial^2 u}{\partial x^2} = 0\,, \tag{A.2}$$

where, w is lateral deflection, u is axial displacement, m_l and m_a are linear density for lateral and axial directions including added mass, E is Young's modulus, A and I are area and moment of inertia of area. The boundary conditions are with rotational spring support at the origin, and a clump weight at the other end as below.

$x = 0$,

$$\begin{cases} w(0) = 0,\ EIw''(0) + kw'(0) = 0, \\ u(0) = 0. \end{cases} \tag{A.3}$$

$x = L$,

$$\begin{cases} EIw''(L) = 0,\ EIw'''(L) - m_c \ddot{w}(L) = 0, \\ EAu'(L) + m_c \ddot{u}(L) = 0. \end{cases} \tag{A.4}$$

The general solution of Eq. (A.1) is denoted as:

$$\begin{cases} w_i = \psi_i e^{j\omega t}, \\ \psi_i = C_{1,i} \sin \lambda_i \dfrac{z}{L} + C_{2,i} \sinh \lambda_i \dfrac{z}{L} + C_{3,i} \cos \lambda_i \dfrac{z}{L} + C_{4,i} \cosh \lambda_i \dfrac{z}{L}. \end{cases} \tag{A.5}$$

Substituting Eq. (A.5) for Eq. (A.3), the frequency equation with two parameters is obtained.

$$\begin{aligned} &(\alpha\beta+1)\lambda\cos\lambda\cosh\lambda - (\alpha\beta+1)\lambda\sin\lambda\sinh\lambda \\ &+\alpha(1+\cos\lambda\cosh\lambda) - 2\beta\lambda^2\sin\lambda\sinh\lambda = 0, \end{aligned} \tag{A.6}$$

here, we have non-dimensional values of frequency f_i and boundary conditions α, β:

$$f_i = \frac{\lambda_i^2}{2\pi L^2}\sqrt{\frac{EI}{m_l}}, \alpha = \frac{kL}{EI}, \beta = \frac{m_c}{m_l L} \tag{A.7}$$

Then, $\lambda_i, C_{j,i}\left(j = 1,2,3,4\right)$ are obtained by solving Eq. (A.6).

Furthermore, the general solution of Eq. (A.1) is denoted as:

$$\begin{cases} u_i = \tau_i e^{j\omega t}, \\ \tau_i = D_i \sin \omega_i \dfrac{z}{L}. \end{cases} \tag{A.8}$$

Substituting Eq. (A.8) for Eq. (A.4), the frequency equation is obtained as,

$$\cos\omega - \mu\omega\sin\omega = 0. \tag{A.9}$$

Here, we have non-dimensional values of frequency f_i and boundary conditions μ:

$$f_i = \frac{\omega_i}{2\pi L}\sqrt{\frac{EA}{m_a}}, \mu = \frac{m_c}{m_a L}, \tag{A.10}$$

Then, ω_i and D_i are obtained by solving Eq. (A.10).

The example of calculation of λ_i and ω_i are shown in Fig. A-1. In the lateral modes, a heavy clump weight reduces the natural frequency, and a stiffened rotational spring increases it in contrast.

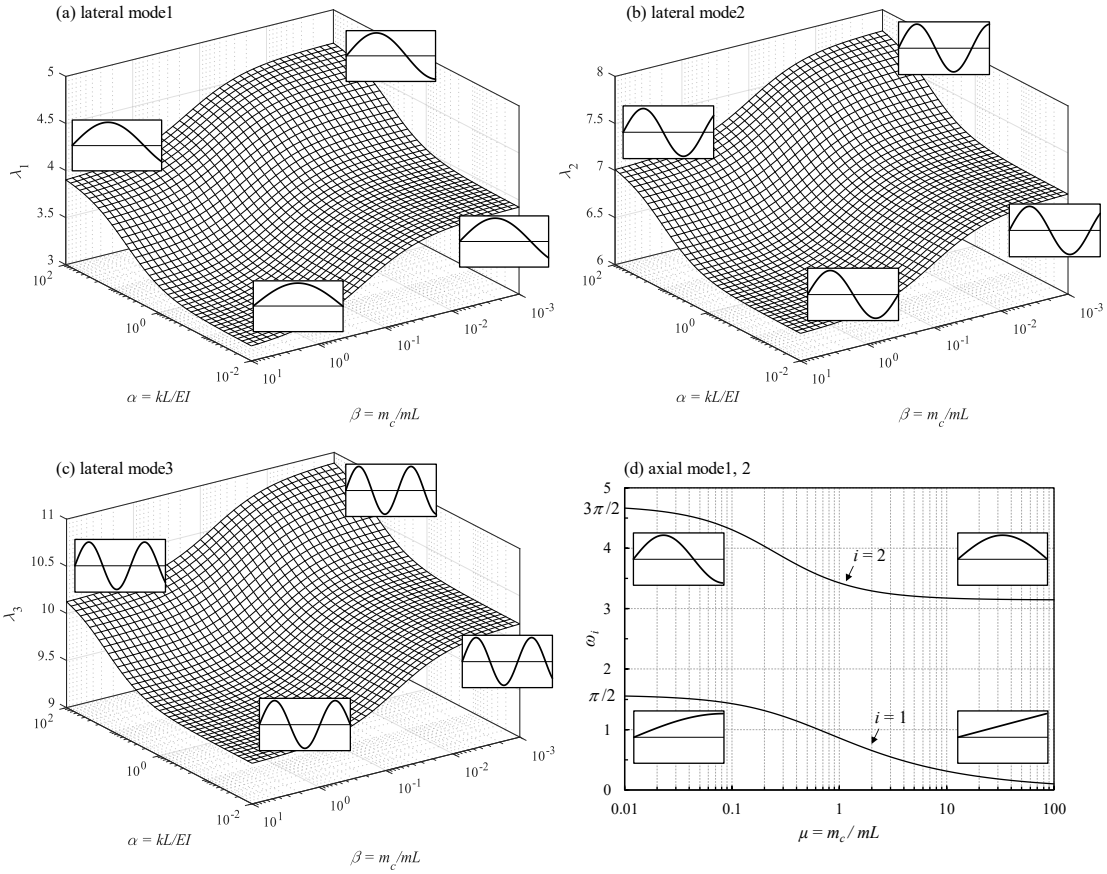

Fig. A-1 Exact solutions of eigen values for rotational spring – mass beam and fixed – mass column.

A.2 Global Matrixes

- Inertia Matrix

$$\mathbf{h}_m(z)=\left[\begin{array}{ccc:ccc} 1 & 0 & -z_0 & cz & -c\boldsymbol{\psi}^{\mathrm{T}} & s\boldsymbol{\tau}^{\mathrm{T}} \\ 0 & 1 & y_0 & sz & -s\boldsymbol{\psi}^{\mathrm{T}} & -c\boldsymbol{\tau}^{\mathrm{T}} \\ -z_0 & y_0 & {y_0}^2+{z_0}^2 & (sy_0-cz_0)z & -(sy_0-cz_0)\boldsymbol{\psi}^{\mathrm{T}} & -(cy_0+sz_0)\boldsymbol{\tau}^{\mathrm{T}} \\ \hdashline cz & sz & (sy_0-cz_0)z & z^2 & -z\boldsymbol{\psi}^{\mathrm{T}} & \mathbf{0}^{\mathrm{T}} \\ -c\boldsymbol{\psi} & -s\boldsymbol{\psi} & -(sy_0-cz_0)\boldsymbol{\psi} & -z\boldsymbol{\psi} & \boldsymbol{\psi}\boldsymbol{\psi}^{\mathrm{T}} & \mathbf{O}^{\mathrm{T}} \\ s\boldsymbol{\tau} & -c\boldsymbol{\tau} & -(cy_0+sz_0)\boldsymbol{\tau} & \mathbf{0} & \mathbf{O} & \boldsymbol{\tau}\boldsymbol{\tau}^{\mathrm{T}} \end{array}\right] \tag{A.11}$$

- Hydrodynamic factor vector

$$\mathbf{h}(z)=\left[\begin{array}{cccccc} c & s & sy_0-cz_0 & z & -\boldsymbol{\psi}^{\mathrm{T}} & \mathbf{0}^{\mathrm{T}} \end{array}\right]^{\mathrm{T}} \tag{A.12}$$

- Constraint matrix

$$\mathbf{h}_r(z)=\left[\begin{array}{ccc:ccc} 0 & 0 & 0 & 0 & \mathbf{0}^{\mathrm{T}} & \mathbf{0}^{\mathrm{T}} \\ 0 & 0 & 0 & 0 & \mathbf{0}^{\mathrm{T}} & \mathbf{0}^{\mathrm{T}} \\ 0 & 0 & 1 & -1 & \boldsymbol{\psi}'^{\mathrm{T}} & \mathbf{0}^{\mathrm{T}} \\ \hdashline 0 & 0 & -1 & 1 & -z\boldsymbol{\psi}'^{\mathrm{T}} & \mathbf{0}^{\mathrm{T}} \\ \mathbf{0} & \mathbf{0} & \boldsymbol{\psi}' & -z\boldsymbol{\psi}' & \boldsymbol{\psi}'\boldsymbol{\psi}'^{\mathrm{T}} & \mathbf{O}^{\mathrm{T}} \\ \mathbf{0} & \mathbf{0} & \mathbf{0} & \mathbf{0} & \mathbf{O} & \mathbf{O} \end{array}\right] \tag{A.13}$$

- Gravitation matrix

$$\mathbf{h}_g(z)=\left[\begin{array}{ccc:ccc} 0 & 0 & 0 & 0 & \mathbf{0}^{\mathrm{T}} & \mathbf{0}^{\mathrm{T}} \\ 0 & 0 & 0 & 0 & \mathbf{0}^{\mathrm{T}} & \mathbf{0}^{\mathrm{T}} \\ 0 & 0 & -z_0 & 0 & \mathbf{0}^{\mathrm{T}} & \mathbf{0}^{\mathrm{T}} \\ \hdashline 0 & 0 & 0 & cz & -c\boldsymbol{\psi}^{\mathrm{T}} & s\boldsymbol{\tau}^{\mathrm{T}} \\ \mathbf{0} & \mathbf{0} & \mathbf{0} & -c\boldsymbol{\psi} & \mathbf{O} & \mathbf{O}^{\mathrm{T}} \\ \mathbf{0} & \mathbf{0} & \mathbf{0} & s\boldsymbol{\tau} & \mathbf{O} & \mathbf{O} \end{array}\right] \tag{A.14}$$

- Elastic forces

$$\mathbf{h}_{k1}(z)=\begin{bmatrix} \ddots & & \\ & \ddots & \\ & EI\boldsymbol{\psi}^{(4)}\boldsymbol{\psi}^{\mathrm{T}}-T_{st}\boldsymbol{\psi}''\boldsymbol{\psi}^{\mathrm{T}}-T_{st}'\boldsymbol{\psi}'\boldsymbol{\psi}^{\mathrm{T}} & \mathbf{O}^{\mathrm{T}} \\ & \mathbf{O} & -EA\boldsymbol{\tau}''\boldsymbol{\tau}^{\mathrm{T}} \end{bmatrix} \tag{A.15}$$

$$\mathbf{h}_{k2}(z)=\begin{bmatrix} \ddots & & \\ & \ddots & \\ & EI\boldsymbol{\psi}''\boldsymbol{\psi}'^{\mathrm{T}}-EI\boldsymbol{\psi}^{(3)}\boldsymbol{\psi}^{\mathrm{T}}+T_{\mathrm{st}}\boldsymbol{\psi}'\boldsymbol{\psi}^{\mathrm{T}} & \mathbf{O}^{\mathrm{T}} \\ & \mathbf{O} & EA\boldsymbol{\tau}'\boldsymbol{\tau}^{\mathrm{T}} \end{bmatrix} \tag{A.16}$$

APPENDIX B

This appendix shows the derivation procedure of Eq. (4.1). The free body diagram of a small arc length δs element is shown in Fig. B-1. The pipe is assumed as a 1D body and is divided into a solid (a pipe wall), an outer "displaced" fluid column and an inner "contained" fluid column with internal forces acting between them. Firstly, defining the position vector **r**, tangent vector **t** and the normal vector **n** along the center line of the pipe (shown in Fig. B-1 (a)), then we apply Newton's second law to the solid element in Fig. B-1 (b).

$$m\frac{\partial^2 \mathbf{r}}{\partial t^2} = \frac{\partial T_w \mathbf{t}}{\partial s} + \frac{\partial Q\mathbf{n}}{\partial s} + \mathbf{F}_o + \mathbf{F}_i + mg\mathbf{j},\ Q = -\frac{\partial M}{\partial s}, \tag{B.1}$$

where m is linear density of solid element, T_w is wall tension, Q is shear force, M is bending moment, g is gravity acceleration, $\mathbf{F}_o$ is reaction from outer fluid, $\mathbf{F}_i$ is reaction from inner fluid, **j** is unit vector for z-direction and s is curvilinear coordinate. Fluid reactions, $\mathbf{F}_i$ and $\mathbf{F}_o$, are formulated based on a concept of "effective tension" widely used in the analysis of submerged pipes and risers and its interpretation given by Sparks [87].

Static pressure and dynamic pressure due to motion act on the outer surface of the solid element. In order to apply Archimedes' law, we additionally consider the static pressure and its reaction acting on both virtual end cross-sections of the outer fluid column as shown in Fig. B-1 (c). The integral of the static pressure distribution around the fluid column can be regarded as the buoyancy acting at the center of the element. Moreover, the dynamic pressure can be expressed by the Morison's equation as,

$$F_n = -C_a \rho S_o \dot{v}_n - \frac{1}{2} C_d \rho D_o v_n |v_n|, \tag{B.2}$$

where, F_n is normal force acting on the center of element, v_n is magnitude of normal velocity of pipe motion as $(\partial \mathbf{r}^{\mathrm{T}}/\partial t)\mathbf{n}$, $C_a \rho S_o$ is added mass, ρ is fluid density and D_o is outer diameter of the pipe.

Thus, the buoyancy, hydrodynamic force by Eq. (B.2) and the reaction pressure at both ends

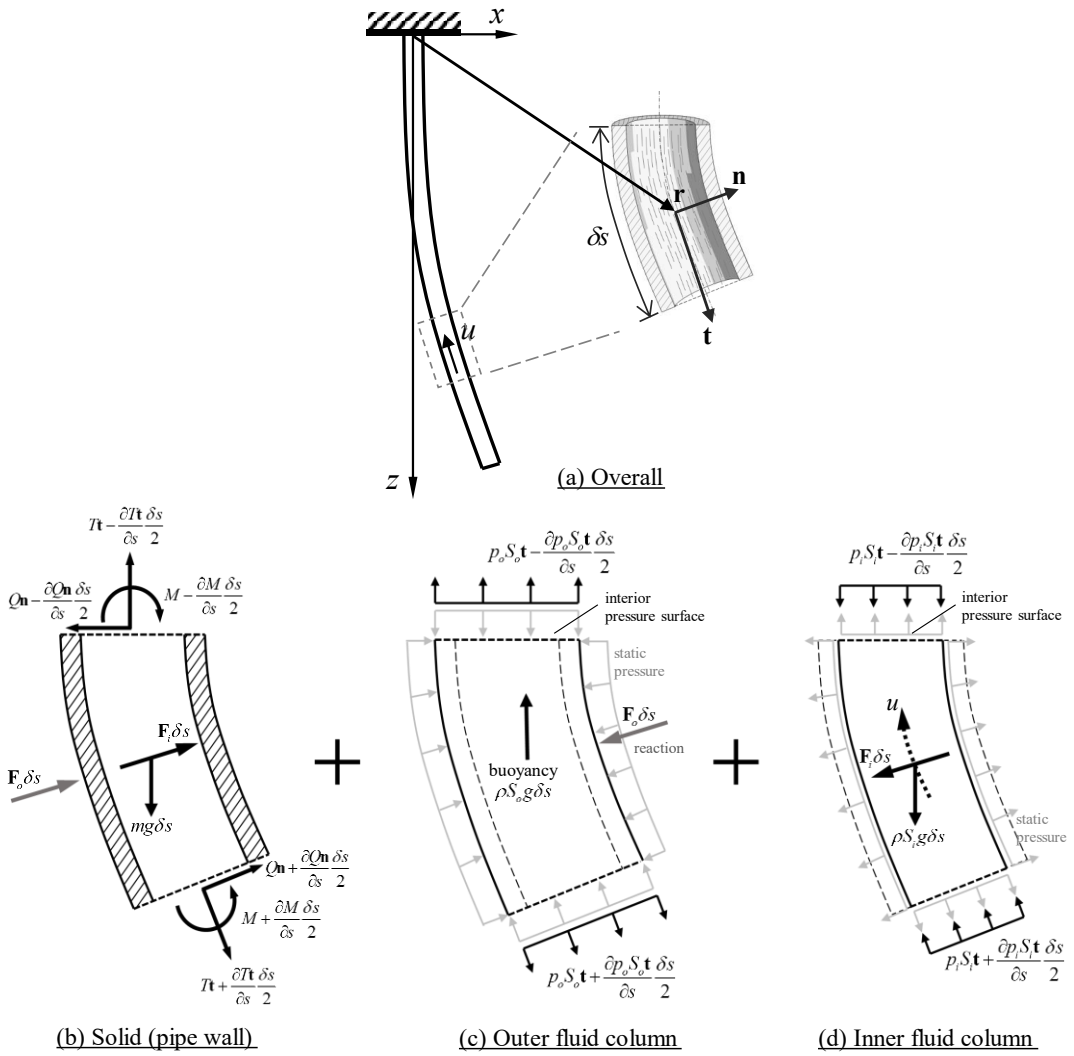

Fig. B-1 Definitions of the system: (a) coordinate system and vectors, (b) forces acting on the pipe wall, (c) forces acting on displaced fluid, and (d) forces acting on contained fluid.

can be summarized as,

$$\mathbf{F}_o = F_n\mathbf{n} - \rho S_o g\mathbf{j} + \frac{\partial p_o S_o \mathbf{t}}{\partial s}. \tag{B.3}$$

The pressure acting on the inner surface of the solid element is evaluated by the same procedure. The inner fluid is basically represented as perfect fluid; however, the shear forces with the inner pipe wall due to the viscosity, are additionally evaluated by Darcy-Weisbach equation as,

$$\tau = \frac{f}{8}\rho u^2 \Leftrightarrow \delta p_i = \frac{\pi D_i \delta s}{S_i}\tau = f\frac{\delta s}{D_i}\frac{1}{2}\rho u^2, \tag{B.4}$$

here, τ is shear force, f is friction loss factor which can be evaluated by Reynolds number and roughness of the pipe surface, δp_i is dynamic pressure loss due to friction and D_i is inner diameter of the pipe. The static pressure is separated into the weight acting at the center of the element and the reaction pressure at both ends as seen in Fig. B-1 (d).

Summarizing these forces, the equation of motion is obtained considering the Euler equation as below. The reaction from inner fluid is expressed by rearranging it.

$$\rho S_i \frac{D\mathbf{U}}{Dt} = -\frac{\partial p_i S_i \mathbf{t}}{\partial s} - \mathbf{F}_i + \rho S_i g \mathbf{j}, \tag{B.5}$$

here, D/Dt is the material derivative and $\mathbf{U}$ is velocity vector of the inner fluid column by the Eulerian description as,

$$\mathbf{U} = -u\mathbf{t} + \frac{\partial \mathbf{r}}{\partial t}. \tag{B.6}$$

The flow is approximated as a plug flow which has a constant average velocity u in the cross section of the pipe. It is considered reasonable for a fully developed turbulent flow profile.

By using Eqs. (B.1), (B.3) and (B.5), the equation of total motion, including inner and outer fluid, can be denoted by using effective tension T_e as,

$$m\frac{\partial^2 \mathbf{r}}{\partial t^2} + \rho S_i \frac{D\mathbf{U}}{Dt} = \frac{\partial T_e \mathbf{t}}{\partial s} - \frac{\partial^2 M}{\partial s^2}\mathbf{n} - \frac{\partial M}{\partial s}\frac{\partial \mathbf{n}}{\partial s} - F_n \mathbf{n} + \left(mg + \rho S_i g - \rho S_o g\right)\mathbf{j}, \tag{B.7}$$

$$\text{here, } T_e = T_w + p_o S_o - p_i S_i. \tag{B.8}$$

The effective tension is defined as the total force in the solid part and contained fluid, less the force in the displaced fluid column. This concept treats the pipe as a composite system, not only

solid (pipe wall) component, but also inner/outer fluids. This should take care to clearly distinguish between the stresses in the structure and the pressure of the fluid. The effect of fluid and wall friction in Eq. (B.4) does not affect the motion, since the reduction of the wall tension due to shear force and the internal pressure loss cancel each other out, as shown from the definition of the effective tension. However, it should be noted that the internal pressure decreases with the frictional pressure loss.

Finally, the linear equation of motion Eq. (4.1) can be derived by linearizing Eq. (B.7).

REFERENCES

[1] Avery, W.H., Wu, C. Renewable Energy from the Ocean: A Guide to OTEC, Oxford University Press, 1994.

[2] Rajagopalan, K., Nihous, G.C. Estimates of global Ocean Thermal Energy Conversion (OTEC) resources using an ocean general circulation model. *Renewable Energy*. 50, 532–540, 2013.

[3] Rajagopalan, K., Nihous, G.C. An Assessment of Global Ocean Thermal Energy Conversion Resources With a High-Resolution Ocean General Circulation Model. *Journal of Energy Resources Technology*. 135, 2013.

[4] Nihous, G. A Preliminary Investigation of the Effect of Ocean Thermal Energy Conversion (OTEC) Effluent Discharge Options on Global OTEC Resources. *Journal of Marine Science and Engineering*. 6, 25, 2018.

[5] Claude, G. Power from the tropical seas. *Mechanical Engineering*. 52, 1039–1044, 1930.

[6] Miller, A., Ascari, M. OTEC Advanced Composite Cold Water Pipe: Final Technical Report, United States, 2011.

[7] Kamogawa, H. OTEC research in Japan. *Energy*. 5, 481–492, 1980.

[8] Nagasaki, S. Mooring design of offshore floating structure, Sankaido Publishing Co., Ltd., 1981.

[9] Cohen, R., Lennard, D.E., Turner, J.H., Wadhams, P. Energy from the Ocean. *Philosophical Transactions of the Royal Society of London. Series A, Mathematical and Physical Sciences*. 307, 405–437, 1982.

[10] George, J.F., Richards, D. Baseline designs of moored and grazing 40-MW OTEC pilot plants. Volume A. Detailed report, United States, 1980.

[11] TRW Systems Group. Ocean thermal energy conversion: research on an engineering evaluation and test program, TRW Systems Group, Redondo Beach, CA, 1975.

[12] Waid, R.L. OTEC Platform Configuration And Integration Studies, in: *Proceedings of the Annual Offshore Technology Conference*, pp. 2471–2474, 1978.

[13] Paulling, J.R. Frequency-domain analysis of OTEC CW pipe and platform dynamics, in: *Proceedings of the Annual Offshore Technology Conference*, pp. 1641–1652, 1979.

[14] Jawish III, W.K., Scotti, R. Study of three OTEC cold water pipe design analysis computer models, in: *Proceedngs of the Ocean Energy Conference*, pp. 25–30, 1981.

[15] Griffin, O.M. Otec cold water pipe design for problems caused by vortex-excited oscillations. *Ocean Engineering*. 8, 129–209, 1981.

[16] TRW Systems Group. Ocean thermal energy conversion cold water pipe preliminary design project. Final report, United States, 1979.

[17] McGuinness, T., Griffin, A., Hove, D. Preliminary designs of cold-water pipes for barge- and spar-type otec plants., in: *Proceedings of the 6th Ocean Thermal Energy Conversion Conference*, Washington, DC, pp. 6.1.1-6.1.12, 1979.

[18] McGuinness, T., Scotti, R.S. OTEC Cold Water Pipe Program Status, in: *Proceedings of the Annual Offshore Technology Conference*, pp. 65–78, 1980.

[19] Sherwood, W.G., Dunning, F.S. OTEC Program - U. S. Department Of Energy Test And Evaluation Program, in: *Proceedings of the Annual Offshore Technology Conference*, pp. 1623–1640, 1979.

[20] Owen, W.L., Trimble, L.C. Mini-OTEC operational results, in: *Proceedings of the 7th Ocean Energy Conference*, Washington, D.C., pp. 14.1.1-14.1.9, 1981.

[21] Svensen, N.A. An overview of the OTEC-1 design, in: *Proceedings of the 6th Ocean Thermal Energy Conversion Conference*, Dept. of Energy, Washington, D.C., pp. 5.3.1-5.3.15, 1979.

[22] Archbold, P. Development of a test program for OTEC-1, in: *Proceedings of the 6th Ocean Thermal Energy Conversion Conference*, Washington, D.C., pp. 5.4.1-5.4.13, 1979.

[23] Hoshide, R.K., Klein, A., Polino, D.L., Poucher, F.W. OTEC-1 test operations experience. Final report, United States, 1983.

[24] Ramsden, H.D. Conversion of the USNS Chepachet to the OTEC-1 platform. *Marine Technology*. 20, 64–70, 1983.

[25] Ramsden, H.D., Watts, W.A. OTEC-1 mooring. *Marine Technology*. 19, 256–267, 1982.

[26] Harms, V.W. Current measurements off Keahole Point, Hawaii: application to OTEC-1 ocean test platform, United States, 1981.

[27] McGuinness, T. OTEC platform and cold weater pipe test program, in: *Proceedings of the 7th Ocean Energy Conference*, Washington, D.C., pp. 14.3.1-14.3.6, 1981.

[28] Barr, R., Giannotti, J., Deuchler, W., Scotti, R., Stadter, J., Walsh, J.P., Weiss, R. Report of ad hoc OTEC cold water pipe committee, United States, 1980.

[29] The Johns Hopkins University Applied Physics Laboratory. Verification test for cold water pipe analysis. Part A. Test description, results, and model comparisons, United States, 1980.

[30] Vega, L.A., Nihous, G.C. At-sea test of the structural response of a large-diameter pipe attached to a surface vessel, in: *Proceedings of the Annual Offshore Technology Conference*, Offshore Technology Conference, pp. 473–480, 1988.

[31] Ravindran M, Abraham, R. The Indian 1 MW demonstration OTEC plant and the development activities. *Oceans Conference Record (IEEE)*. 3, 1622–1628, 2002.

[32] Nihous, G.C., Vega, L.A. Design of a 100 MW OTEC-hydrogen plantship. *Marine Structures*. 6, 207–221, 1993.

[33] Maeda, H., Miyajima, S., Shin, H., Yamakoshi, Y., Aketa, S. Study of Behaviors of a Moored Floating Structure with a CWP. *Journal of the Society of Naval Architects of Japan*. 345–358, 1991.

[34] Ouchi, K., Otsuka, K., Omura, H. Recent advances of ocean nutrient enhancer "TAKUMI" project, in: *Proceedings of the ISOPE Ocean Mining Symposium*, China, pp. 7–12, 2005.

[35] Langer, J., Quist, J., Blok, K. Recent progress in the economics of ocean thermal energy conversion: Critical review and research agenda. *Renewable and Sustainable Energy Reviews*. 130, 109960, 2020.

[36] Kim, H.J., Lee, H.S., Seo, J.B., Lim, S.T., Moon, J.H., Kim, Y.S. Demonstration of 1MW OTEC plant in Korean waters in 2019, in: *Proceedings of the 7th OTEC Symposium*, Busan, Korea, 2019.

[37] Cable, B. OTEC Technology Development Report, California, 2010.

[38] Cable, B. OTEC System Design Report, California, 2010.

[39] Zaiger, K. 2.5 MW OTEC Mini-Spar Pilot Plant, California, 2011.

[40] Shi, S., Halkyard, J., Kurup, N., Jiang, L. Coupled analysis approach in OTEC system design, in: *Proceedings of the International Conference on Offshore Mechanics and Arctic Engineering - OMAE*, pp. 795–802, 2012.

[41] Varley, R., Halkyard, J., Johnson, P., Shi, S., Marinho, T. OTEC Cold Water Pipe-Platform Subsystem Dynamic Interaction Validation, United States, 2014.

[42] Halkyard, J., Sheikh, R., Marinho, T., Shi, S., Ascari, M. Current developments in the validation of numerical methods for predicting the responses of an ocean thermal energy conversion (OTEC) system cold water pipe, in: *Proceedings of the International Conference on Offshore Mechanics and Arctic Engineering - OMAE*, OMAE2014-24636, 2014.

[43] Kibbee, S. Ocean thermal energy conversion at SBM, in: *18th Offshore Symposium*, Society of Naval Architects and Marine Engineers, pp. 3–18, 2013.

[44] Xiang, S., Cao, P., Erwin, R., Kibbee, S. Otec cold water pipe global dynamic design for ship-Shaped vessels, in: *Proceedings of the International Conference on Offshore Mechanics and Arctic Engineering - OMAE*, OMAE2013-10927, 2013.

[45] Cao, P., Xiang, S., He, J., Kibbee, S., Bian, S. Advancing Cold Water Intake Riser Design through Model Test, in: *Proceedings of the Annual Offshore Technology Conference*, pp. 3019–3033, 2015.

[46] Wang, J., Xiang, S., Fu, S., Cao, P., Yang, J., He, J. Experimental investigation on the dynamic responses of a free-hanging water intake riser under vessel motion. *Marine Structures*. 50, 1–19, 2016.

[47] Zhang, W., Li, Y., Wu, X., Guo, S. Review of the applied mechanical problems in ocean thermal energy conversion. *Renewable and Sustainable Energy Reviews*. 93, 231–244, 2018.

[48] Bureau Veritas. Classification and Certification of Ocean Thermal Energy Converter (OTEC) - Tentative Rules -, 2018.

[49] IEC. Marine energy - Wave, tidal, and other water current converters - Part 20: Design and analysis of an Ocean Thermal Energy Conversion (OTEC) plant - General guidance, IEC TS 62600-20, 2019.

[50] Hirao, S.C., Umeda, J., Kokubun, K., Fujiwara, T. Tank Test and Numerical Simulation of Spar Type Floating OTEC, in: *Proceedings of the International Conference on Offshore Mechanics and Arctic Engineering - OMAE*, OMAE2021-62107, 2021.

[51] Kwon, Y.J., Kim, H.J., Jung, D.H. A Study for Forced Oscillation Experiment for OTEC Riser under Current, in: *Proceedings of the International Ocean and Polar Engineering Conference*, pp. 212–219, 2015.

[52] Adiputra, R., Utsunomiya, T. Stability based approach to design cold-water pipe (CWP) for ocean thermal energy conversion (OTEC). *Applied Ocean Research*. 92, 2019.

[53] Adiputra, R., Utsunomiya, T. Linear vs non-linear analysis on self-induced vibration of OTEC cold water pipe due to internal flow. *Applied Ocean Research*. 110, 102610, 2021.

[54] Ocean Energy Systems. International Levelized Cost of Energy for Ocean Energy Technologies, 2015.

[55] Adiputra, R., Utsunomiya, T., Koto, J., Yasunaga, T., Ikegami, Y. Preliminary design of a 100 MW-net ocean thermal energy conversion (OTEC) power plant study case:

Mentawai island, Indonesia. *Journal of Marine Science and Technology*. 25, 48–68, 2020.

[56] Hino, T. Proceedings of CFD Workshop TOKYO 2005, Tokyo, 2005.

[57] Shimamura, Y. FPSO/FSO: State of the art. *Journal of Marine Science and Technology*. 7, 59–70, 2002.

[58] DNVGL. OFFSHORE STANDARDS Position mooring. DNVGL-OS-E301, 2018.

[59] ISO. Fibre ropes for offshore stationkeeping -Polyester. ISO 18692, 2007.

[60] Utsunomiya, T. Irregular frequency removal and convergence in higher-order bem for wave diffraction/radiation analysis, in: *Proceedings of the International Conference on Offshore Mechanics and Arctic Engineering - OMAE*, American Society of Mechanical Engineers (ASME), 2019.

[61] Newman, J.N. The Drift Force and Moment on Ships in Waves. *Journal of Ship Research*. 11, 51–60, 1967.

[62] Newman, J.N. Second-order, slowly-varying forces on vessels in irregular waves, University College London, 1974.

[63] Himeno, Y. Prediction of Ship Roll Damping - A State of the Art, 1981.

[64] Yukawa, K., Hoshino, K., Hara, S., Yamakawa, K. An Estimation of Hydrodynamic Forces Acting on a Trimmed Ship Hull. *Journal of the Society of Naval Architects of Japan*. 2002, 29–36, 2002.

[65] Fujiwara, T., Ueno, M., Nimura, T. Estimation of Wind Forces and Moments acting on Ships. *Journal of the Society of Naval Architects of Japan*. 1998, 77–90, 1998.

[66] DNVGL. RECOMMENDED PRACTICE Environmental conditions and environmental loads. DNVGL-RP-C205, 2017.

[67] ISO. Petroleum and natural gas industries — Specific requirements for offshore structures — Part 7: Stationkeeping systems for floating offshore structures and mobile offshore units. ISO 19901-7, 2013.

[68] Ormberg, H., Larsen, K. Coupled analysis of floater motion and mooring dynamics for a turret-moored ship. *Applied Ocean Research*. 20, 55–67, 1998.

[69] Low, Y.M., Grime, A.J. Extreme response analysis of floating structures using coupled frequency domain analysis. *Journal of Offshore Mechanics and Arctic Engineering*. 133, 2011.

[70] Cruces Girón, A.R., Corrêa, F.N., Vázquez Hernández, A.O., Jacob, B.P. An integrated methodology for the design of mooring systems and risers. *Marine Structures*. 39, 395–423, 2014.

[71] Chakrabarti, S.K., Frampton, R.E. Review of riser analysis techniques. *Applied Ocean Research*. 4, 73–90, 1982.

[72] Paidoussis, M.P., Luu, T.P. Dynamics of a Pipe Aspirating Fluid Such as Might be Used in Ocean Mining. *Journal of Energy Resources Technology*. 107, 250–255, 1985.

[73] Païdoussis, M.P., Issid, N.T. Dynamic stability of pipes conveying fluid. *Journal of Sound and Vibration*. 33, 267–294, 1974.

[74] PaÏdoussis, M.P., Li, G.X. Pipes conveying fluid: A model dynamical problem. *Journal of Fluids and Structures*. 7, 137–204, 1993.

[75] Païdoussis, M.P. Fluid-Structure Interactions Volume 1: Slender Structures and Axial Flow Second Edition, Academic Press, Oxford, 2014.

[76] Pramila, A. Undamped cantilever aspirating fluid may be stable. *Rakenteiden Mekaniikka*. 25, 3–14, 1992.

[77] Cui, H., Tani, J. Effect of boundary conditions on the stability of a cantilever pipe discharging and aspirating fluid. *JSME International Journal. Ser. C, Dynamics, Control, Robotics, Design and Manufacturing*. 39, 20–24, 1996.

[78] Païdoussis, M.P. ASPIRATING PIPES DO NOT FLUTTER AT INFINITESIMALLY SMALL FLOW. *Journal of Fluids and Structures*. 13, 419–425, 1999.

[79] Païdoussis, M.P., Semler, C., Wadham-Gagnon, M. A reappraisal of why aspirating pipes do not flutter at infinitesimal flow. *Journal of Fluids and Structures*. 20, 147–156, 2005.

[80] Giacobbi, D.B., Rinaldi, S., Semler, C., Païdoussis, M.P. The dynamics of a cantilevered pipe aspirating fluid studied by experimental, numerical and analytical methods. *Journal of Fluids and Structures*. 30, 73–96, 2012.

[81] Axisa, F. Flow Conditions at the Inlet of Aspirating Pipes: Part 1—Theory. *American Society of Mechanical Engineers, Fluids Engineering Division (Publication) FEDSM*. 3, 849–860, 2011.

[82] Butt, M.F.J., Paidoussis, M.P., Nahon, M. An Investigation Into the Dynamics of a Pipe Aspirating Fluid, in: *Proceedings of the International Design Engineering Technical Conferences and Computers and Information in Engineering Conference International Design Engineering Technical Conferences and Computers and Information in Engineering Conference*, 2018.

[83] Ma, Y., You, Y., Feng, A. Stability Analysis of Cold-water Pipe Under Different Inlet Flow Field Models, in: *Proceedings of International Ocean and Polar Engineering Conference*, OnePetro, 2021.

[84] Kuiper, G.L., Metrikine, A. V. Experimental investigation of dynamic stability of a cantilever pipe aspirating fluid. *Journal of Fluids and Structures*. 24, 541–558, 2008.

[85] Debut, V., Antunes, J., Axisa, F. Flow Conditions at the Inlet of Aspirating Pipes: Part 2—Experiments. *American Society of Mechanical Engineers, Fluids Engineering Division (Publication) FEDSM*. 3, 861–873, 2011.

[86] Zhang, Z. A flexible new technique for camera calibration. *IEEE Transactions on Pattern Analysis and Machine Intelligence*. 22, 1330–1334, 2000.

[87] Sparks, C.P. The influence of tension, pressure and weight on pipe and riser deformations and stresses. *Journal of Energy Resources Technology, Transactions of the ASME*. 106, 46–54, 1984.

[88] Adiputra, R., Utsunomiya, T. Finite Element Modelling of Ocean Thermal Energy Conversion (OTEC) Cold Water Pipe (CWP), in: *Proceedings of the International Conference on Offshore Mechanics and Arctic Engineering - OMAE*, OMAE2022-78135, Hamburg, Germany, 2022.

[89] Kuiper, G.L., Metrikine, A. V. Dynamic stability of a submerged, free-hanging riser conveying fluid. *Journal of Sound and Vibration*. 280, 1051–1065, 2005.